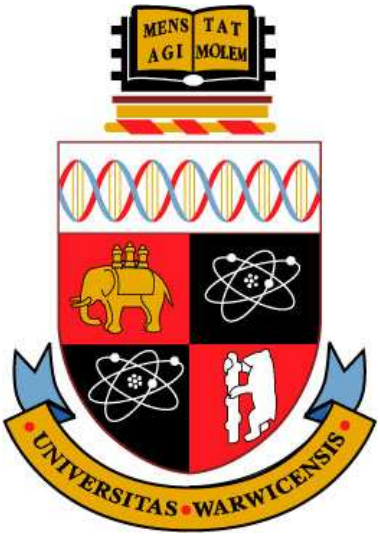

A study of the static and dynamic magnetic behaviour of $Cu_2Te_2O_5(Br_xCl_{1-x})_2$

by

S. J. Crowe

Thesis

Submitted to the University of Warwick

for the degree of

Doctor of Philosophy

Department of Physics

October 2005

THE UNIVERSITY OF WARWICK

Contents

List of Figures

Acknowledgments

I would first and foremost like to thank my supervisor, Don Paul, for countless scientific discussions and support. I would also like to thank the other members of the Superconductivity and Magnetism Group (Geetha, Martin L, Oleg, Martin D, Tom, Jenny and Nic) for all their help, and for being a great bunch of people to work with. In particular I would like to thank Subham Majumdar for his guidance and friendship. I would also like to thank Jon Duffy for getting me to Warwick in the first place.

On my trips to the neutron facilities at ISIS and the ILL I have always encountered friendly and enthusiastic support from all involved. In particular I would like to acknowledge the help of Garry McIntyre, Clemens Ritter and John Stride at the ILL and Jon Taylor, Rob Bewley, Adroja, Pas and Dickon at ISIS. I would also like to thank Simon Levett for his help and good company. I am very grateful to Oksana Zaharko for numerous discussions about magnetic structure refinements, and to Aziz Daoud-Aladine for sharing his amazing knowledge of FullProf.

Last but not least, I would like to thank my parents for their unbelievable support over the last three years.

Declarations

The work presented in this thesis was carried out by me except where explicitly stated. All of the experiments described in this thesis took place during the period October 2002 to October 2005 and were carried out at the Department of Physics at the University of Warwick, the Institut Laue-Langevin or ISIS at the Rutherford Appleton Laboratory. For these experiments I was either the sole experimentalist or a leading member of the experimental team. The neutron diffraction study of single crystal $Cu_2Te_2O_5Br_2$ (described in section 4.3) was performed in collaboration with Dr O. Zaharko and Dr A. Daoud-Aladine. No part of this thesis has been submitted for examination at any other institute. Parts of the work described in this thesis have been published in the following articles;

S.J. Crowe, S. Majumdar, M.R. Lees, D.McK. Paul, R.I. Bewley, S.J. Levett and C. Ritter, *Neutron inelastic scattering investigation of the magnetic excitations in $Cu_2Te_2O_5X_2$ (X=Br,Cl).* Phys. Rev. B **71**, 224430 (2005).

S.J. Crowe, S. Majumdar, M.R. Lees, D.McK. Paul, D.T. Adroja and S.J. Levett, *Inelastic neutron scattering study of the spin-gap behaviour in $Cu_2Te_2O_5Br_2$.* Physica B **359-361**, 1219 (2005).

O. Zaharko, H. Ronnow, J. Mesot, S.J. Crowe, D.McK. Paul, P.J. Brown, A. Daoud-Aladine, A. Meents, A. Wagner, M. Prester and H. Berger, *Incommensurate magnetic ordering in $Cu_2Te_2O_5X_2$ (X=Cl,Br) studied by single crystal neutron diffraction.* cond-mat/0512617.

S.J. Crowe, M.R. Lees, D.McK. Paul, R.I. Bewley, J.W. Taylor, G. McIntyre,

O. Zaharko, H. Berger, *The effect of externally applied pressure on the magnetic behaviour of* $Cu_2Te_2O_5(Br_xCl_{1-x})_2$. cond-mat/0601023.

Abstract

The spin tetrahedral compounds $Cu_2Te_2O_5X_2$ (X=Br,Cl) have recently attracted attention due to the interesting contrast in their magnetic properties. In this thesis the structural and dynamic magnetic behaviour of these compounds, as well as intermediate doped compositions, are studied by a combination of neutron elastic and inelastic scattering.

Polycrystalline neutron diffraction measurements of $Cu_2Te_2O_5(Br_xCl_{1-x})_2$ with compositions x = 0, 0.25, 0.52, 0.73 and 1 have been performed. The magnetic structures of all compositions are found to be incommensurate, with propagation vectors decreasing linearly with x, from $\boldsymbol{\kappa_{Br}}$ = [0.170, 0.350, 1/2] for the bromide to $\boldsymbol{\kappa_{Cl}}$ = [0.150, 0.420, 1/2] for the chloride. Single crystal neutron diffraction measurements of $Cu_2Te_2O_5Br_2$ reveal the magnetic structure to comprise of a complicated helical spin arrangement.

Neutron inelastic scattering investigations have been performed on polycrystalline samples of $Cu_2Te_2O_5(Br_xCl_{1-x})_2$ with compositions x = 0, 0.25, 0.52, 0.63, 0.73 and 1. Magnetic excitations with a dispersive component are observed in all compositions, which are associated with the 3D incommensurate magnetic order that develops below their respective transition temperatures. Both the apparently flat and dispersive components of the excitations in the compositions x = 0, 0.25, 0.52, 0.63 and 0.73 soften as the temperature approaches T_N, leaving diffuse quasi-elastic scattering above the transition temperature. However, in the bromide the excitations remain well-defined well above T_N^{Br}, which may perhaps be attributed to the presence of a degree of low dimensional correlations above T_N^{Br} in this compound.

Finally, the effect of externally applied pressure on the magnetic behaviour of $Cu_2Te_2O_5(Br_xCl_{1-x})_2$ with compositions x = 0, 0.73 and 1 was investigated. Magnetic susceptibility measurements reveal an increase in the overall coupling strength under pressure in all three samples, whilst the transition temperatures behave in a contrasting manner, increasing under pressure in the chloride and x = 0.73 sample, whilst decreasing in the bromide.

Chapter 1

Introduction

1.1 Introduction to magnetism

The study of magnetism dates back almost 3000 years. As legend has it, a Greek shepherd named Magnes was tending his herd when his iron-tipped boots became stuck fast to a clump of naturally magnetised lodestone (iron ore). The Greeks were fascinated by the phenomenon, and their writings dominated thinking on the matter for centuries to come. Yet it is the Chinese who are credited with the first technological utilization of loadstone with the invention of the compass, which found widespread use in western Europe by the 12th century. The underlying physics of magnetism was little understood until the 'electromagnetic revolution' of the 19th century, which established the connection between magnetism and electricity. However, it was not until the 20th century and the advancement of quantum mechanics that a theory of magnetism capable of satisfactorily explaining the magnetic properties of real materials took shape. More recently the focus of attention in this field has been dominated by so-called **quantum magnetism**, the study of spin systems with sufficiently low spin or dimensionality that quantum fluctuations dominate the behaviour. This chapter offers a brief introduction to the physics of magnetism (section 1.1), quantum magnetism (section 1.2) and

the quantum magnetic system studied in this work, $Cu_2Te_2O_5(Br_xCl_{1-x})_2$ (section 1.3).

1.1.1 Magnetic spin

The concept of magnetic spin is deeply rooted in quantum mechanics and is discussed in many quantum textbooks (see for example references [24] and [62]). In quantum mechanics, the orbital angular momentum (**L**) of an electron is given by $\hbar\sqrt{l(l+1)}$, and its component along the z-axis is given by $\hbar m_l$ (where the quantum numbers $l = 0, 1, 2...$ and $m_l = -l, -l+1, ..., l-1, l$ define the state of the electron). An electron also possesses an intrinsic angular momentum, or 'spin' (**S**), whose magnitude is $\hbar\sqrt{s(s+1)}$, and its component along the z-axis is $\hbar m_s$. For an electron the spin quantum number (s) is $1/2$, and $m_s = \pm 1/2$. It follows that the magnitude of the spin angular momentum of an electron is $\sqrt{3}\hbar/2$, and the component of the spin along the z-axis is $+\hbar/2$ (spin up) or $-\hbar/2$ (spin down). The total angular momentum of the system, $\mathbf{J}$, is the sum of the orbital and spin components, that is $\mathbf{J} = \mathbf{L} + \mathbf{S}$.

Due to its charge, each component of the angular momentum of an electron has a magnetic moment associated with it. The magnetic moment associated with the orbital angular momentum has a magnitude $\mu_B\sqrt{l(l+1)}$, and a component along the z-axis of $-\mu_B m_l$, where μ_B is the Bohr magneton ($\mu_B = e\hbar/2m_e$). The corresponding magnitude of the spin magnetic moment is $\sim \sqrt{3}\mu_B$, and the component along the z-axis is $\sim \pm\mu_B$.

1.1.2 Diamagnetism and paramagnetism

In solid state systems containing huge numbers of electrons, it is useful to define a bulk property known as the magnetisation, $\mathbf{M}$, which is the magnetic moment per unit volume (see for example [28]). When a material is placed in a magnetic

field ($\mathbf{H}$) its magnetisation determines the field, $\mathbf{B}$, induced inside the material by the relation $\mathbf{B} = \mu_0(\mathbf{H} + \mathbf{M})$, where μ_0 is the permeability of free space. For many materials the magnetisation is proportional to the applied field, $\mathbf{M} \propto \mathbf{H}$, and the constant of proportionality, χ, is the magnetic susceptibility. Materials can be categorised on the basis of their susceptibility. For example, if $\chi < 0$, that is, the induced field acts to oppose the applied field, the material is classed *diamagnetic*. A well-known example of diamagnetic materials are superconductors, which, in their superconducting state, are perfect diamagnets. If $\chi > 0$ then the material is either *paramagnetic* or may belong to a third category of systems, which will be discussed in section 1.1.3. All materials possess a diamagnetic component to their susceptibility. In a classical picture this is explained by Lenz's law; an applied magnetic field induces a current in the electrons of the atom such that the resultant field is opposite to the applied field. However, atoms with unpaired electrons (and therefore a magnetic moment) will also have a paramagnetic (positive) component to their susceptibility, which is often the larger effect. In the absence of an applied field, the magnetic moments of isolated paramagnetic atoms will be oriented randomly and so cancel to give a net magnetic moment of zero. However, in the presence of an applied field, the moments will tend to align with the field giving a positive magnetisation. The lower the temperature, the less thermal fluctuations will oppose the alignment of the moments. Hence the temperature dependence of the susceptibility of a paramagnet is described empirically by Curie's law,

$$\chi = \frac{C_{Curie}}{T}, \tag{1.1}$$

where C_{Curie} is the Curie constant and depends upon the material. From a quantum mechanical derivation (see, for example, reference [6]), the temperature dependence of the susceptibility in low magnetic fields is found to be

$$\chi \approx \frac{n\mu_0\mu_{eff}^2}{3k_BT}, \tag{1.2}$$

where n is the number of magnetic moments per unit volume and the effective moment, μ_{eff}, is given by $\mu_{eff} = g_J \mu_B \sqrt{J(J+1)}$ (where g_J is the Landé g-factor). Even for systems in which J=0 in the ground state, a mixing of the ground state with excited states in a small field leads to a small, temperature independent, positive component to the susceptibility, which is known as Van Vleck paramagnetism.

1.1.3 Exchange

While diamagnets and paramagnets can be explained in terms of isolated moments, a third category of magnetic materials are driven by the interactions between the atomic moments. The dominant interaction between the moments on atoms is not the dipolar interaction (which is relatively very weak), but the *exchange* interaction (see for example reference [2]). Exchange arises from a combination of the Pauli exclusion principle and electrostatic Coulomb repulsion. Electrons with parallel spins are forbidden from being at the same place at the same time by the Pauli exclusion principle. In this sense, one can think of each electron as being surrounded by an 'exchange-correlation hole', a region in which the probability of finding a parallel spin is strongly reduced. The fact that electrons with parallel spins are kept apart like this reduces their Coulomb repulsion energy. The kinetic energy of the electrons increases however, and it is the balance of these competing effects that determines whether or not it is energetically favourable to magnetically order. The idea of exchange manifests itself in the Heisenberg Hamiltonian ($\mathcal{H}$), an important tool often used in modelling spin-systems (see for example [20]),

$$\mathcal{H} = -\sum_{i,j} J_{ij} \mathbf{S_i} \cdot \mathbf{S_j}, \tag{1.3}$$

where J_{ij} is the exchange constant (or exchange integral) between the i^{th} and j^{th} spin. J_{ij} is taken to be positive for ferromagnets (favouring parallel spin alignment), and negative for antiferromagnets (favouring antiparallel alignment).

1.1.4 Exchange paths

In order for exchange to occur, the orbitals of electrons must overlap. However, the exchange interaction decreases rapidly as the distance between the electrons increases, and hence the moments on atoms often interact indirectly through super-exchange [6]. Often a diamagnetic ion (eg. oxygen) lies between the two magnetic ions, for example in magnetic transition metal oxides. In this case, the overlap of the oxygen p-orbitals with the d-orbitals of the metal ions allows for indirect superexchange. However, in a magnetic solid there may be a number of different exchange paths along which the magnetic ions may interact and it is important to determine which are dominant. The qualitative Goodenough [25] rules allow one to predict the relative strength of superexchange paths by considering the angle of the ion-oxygen-ion bonds, the symmetry properties of the ion d-orbitals and the number of unpaired spins of the metal ion. In some magnetic materials super-superexchange interactions, in which the magnetic ions interact via two intermediary atoms, may also be significant (see figure 1.1) [78]. Therefore, when using the Heisenberg Hamiltonian to describe a magnetic solid it is important to consider which exchange constants (J_{ij}) should be included; one may need to consider next nearest neighbour as well as nearest neighbour interactions, and these may arise from direct exchange, superexchange or even super-superexchange. Experimentally, neutron inelastic scattering, Raman scattering and magnetic susceptibility measurements are often used to try to determine the exchange constants.

There is a further type of exchange that is of importance in this work, called the Dzyaloshinsky-Moriya interaction [19, 55]. This is also known as the anisotropic superexchange interaction and arises when one considers spin-orbit coupling in the framework of exchange. Spin-orbit coupling is a relativistic effect and is an interaction between the orbital and spin components of the electron's wave function, which results in a splitting of the states with well defined $\mathbf{L}$ and $\mathbf{S}$. The Dzyaloshinsky-Moriya interaction is the exchange interaction between one

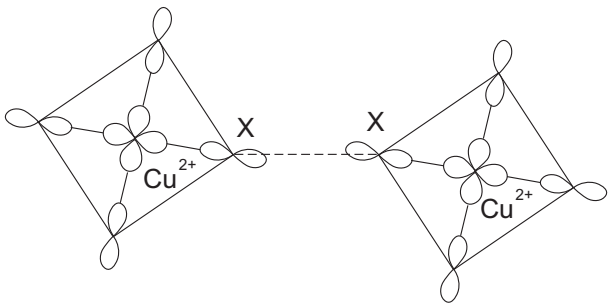

Figure 1.1: An example of a super-superexchange interaction in which the $x^2 - y^2$ orbitals of two Cu^{2+} ions interact via the p-orbitals of two X ions (X=Br,Cl).

ground state magnetic ion and one excited (spin-orbit split) magnetic ion.

1.1.5 Magnetic order

Exchange is the mechanism by which materials are able to magnetically order. The correlations between magnetic atoms may result in a number of different types of order, the most common of which are ferromagnetic and antiferromagnetic order. In a ferromagnet, the moments spontaneously order below the transition temperature T_C in a parallel configuration, giving an overall net moment. Below T_C, the relationship between M and H becomes non-unique due to hysteresis, which arises due to the formation of domains that behave in a complicated manner under an applied magnetic field. Above T_C, however, the susceptibility is given by the Curie-Weiss law,

$$\chi = \frac{C_{Curie}}{T - T_C} \qquad (T > T_C). \tag{1.4}$$

In contrast, in an antiferromagnet the moments order in an anti-parallel arrangement below the (Néel) transition temperature, T_N, with an overall net magnetic moment of zero. One can think of the magnetic crystal in this case as consisting of two inter-penetrating sublattices that magnetise in the opposite direction to each other. One can express the temperature dependence of the susceptibility by

$$\chi = \frac{C_{Curie}}{T + T_N} \qquad (T > T_N). \tag{1.5}$$

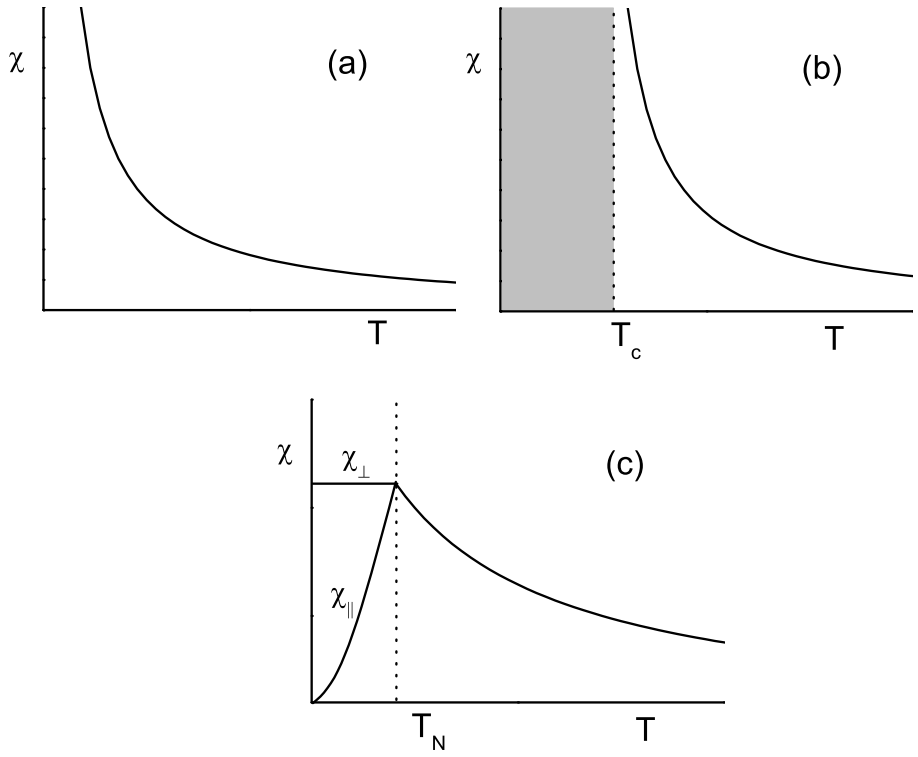

Figure 1.2: Magnetic susceptibility as a function of temperature for a typical (a) paramagnet, (b) ferromagnet and (c) antiferromagnet.

Figure 1.2 shows the temperature dependence of the susceptibility of a typical (a) paramagnet, (b) ferromagnet and (c) antiferromagnet. Whereas in the case of a ferromagnet the susceptibility becomes infinite at T_C, in an antiferromagnet the susceptibility reaches a well-defined maximum at T_N. Below T_N, the behaviour of the susceptibility depends upon the orientation of the applied field with respect to the direction of the moments because of crystalline anisotropy. If the field is applied perpendicular to the direction of the spins, the susceptibility is temperature independent. If, however, the field is applied parallel to the spins, then the susceptibility falls continuously to zero with decreasing temperature.

In general, a magnet with spin s has $2s+1$ quantised orientations, which are degenerate. The entropy associated with these magnetic states is $k_B \ln(2s+1)$, where k_B is the Boltzmann constant (see for example [26]). Therefore, the total

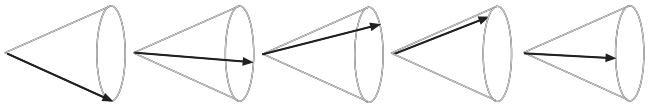

Figure 1.3: Helical magnetic structure in which the spins trace out the shape of a helix.

magnetic entropy (S_M) per mole of a spin s system is given by

$$S_M = R \ln(2s + 1), \tag{1.6}$$

where R is the ideal gas constant ($R = 8.32$ J mol^{-1} K^{-1}).

There are a number of other possible ordered arrangements besides ferromagnetic and antiferromagnetic. For example, ferrimagnets have inter-penetrating sublattices like in the antiferromagnetic case discussed above, but the moments on the sublattices are unequal, resulting in an overall net moment. Another example, which is important in this thesis, is a helical magnetic arrangement. In this case the direction of the spins rotates from cell to cell within parallel planes, tracing out the shape of a helix (see figure 1.3). The moments are modulated by a propagation vector, $\boldsymbol{\kappa}$, which defines by how much the spins rotate from cell to cell; this can be either commensurate or incommensurate with the underlying crystal lattice.

1.1.6 Phonons and magnons

In a dynamic lattice the thermal vibrations of the atoms may be described as lattice excitations, the energies of which are quantised. The quanta of lattice excitations are called phonons. The energy of phonon modes vary characteristically across the Brillouin Zone (BZ) and this can be described by the dispersion relation that relates their energy $\hbar\omega$ to their (crystal) momentum $\hbar q$. Typically there are two branches of the dispersion relation, acoustic and optical. Whilst a monatomic system only has acoustic vibrations, a diatomic or polyatomic system will also have optical vibrations. Acoustic phonons are so named because at low q their

dispersion relation has the form $\omega \propto q$, which is characteristic of sound waves. In particular, at $q = 0$ their energy is zero, that is, vanishingly small energy is required to excite the phonons at the zone centre, and hence the acoustic phonons are the Goldstone modes of the system (see, for example, reference [6]). Optical phonons, on the other hand, have non-zero energy at q=0 and tend to be flatter modes.

The contribution of phonons to the specific heat of a material can be rather complicated. However, there are a number of simplified models that often give a very reasonable approximation to the observed specific heat. Firstly, Einstein's model of lattice vibrations is based on the simplifying assumptions that each of the atoms oscillates as an independent harmonic oscillator, and that all of the atoms oscillate with the same frequency, ω_E. Combining the quantum mechanical solutions of the harmonic oscillator with Maxwell-Boltzmann statistics, Einstein derived an expression for heat capacity based on these assumptions (see for example, reference [26]). In the high temperature limit, Einstein's model agrees with the empirical Dulong-Petit law, which states that the heat capacity, C, of a molecule containing r atoms is $3rR$, where R is the gas constant. At low temperatures, Einstein's model qualitatively agrees with the observed drop in heat capacity, which is purely a quantum phenomena. However, quantitatively the Einstein model is regarded as only a simple approximation to the heat capacity of real materials, and, in particular, approximates the optical phonons far better than the acoustic phonons.

The Debye model provides a better approximation to the heat capacity of many systems, and in particular to the contribution of acoustic phonons. In this model the atoms are considered as oscillators that, instead of all having the same frequency, have a distribution of frequencies that result from considering the propagation of an acoustic wave through an isotropic solid. The derivation of this frequency distribution and the heat capacity based on the Debye assumption

can be found, for example, in reference [26]. As with the Einstein model, in the high temperature limit, the Debye model predicts the Dulong-Petit law. At low temperatures, however, the Debye model shows a T^3 behaviour with the relation

$$C_v = \frac{12}{5} r R \pi^4 \left(\frac{T}{\theta_D} \right)^3 , \tag{1.7}$$

where θ_D is the characteristic Debye temperature defined by the cut-off frequency (ω_D), $k_B \theta_D = \hbar \omega_D$. This is a measure of the temperature above which all modes begin to be excited, and below which the modes start to be 'frozen out'.

In a magnetic material, fluctuations of the spins will propagate through the crystal due to exchange correlations in the ordered state, and this propagation is known as a spin wave. Whilst the elementary quantised excitations of a lattice are called phonons, the quantised excitations (spin waves) of a magnetic system are called magnons. As with phonons, magnons have characteristic dispersion relations, which in a ferromagnetic material have the form $\omega \propto q^2$ at low q (see, for example, reference [76]). In contrast, the dispersion relation for antiferromagnet spin waves at low q is $\omega \propto q$, where the constant of proportionality is the spin wave speed. The corresponding contribution to the heat capacity of spin waves at low temperatures is $\propto T^{3/2}$ and $\propto T^3$ for ferromagnetic and antiferromagnetic materials respectively [26]. The dispersion relation of a spin wave on a linear antiferromagnetic chain is found to be $\omega \propto |\sin(qa)|$, where a is the inter-spin separation (see [53] and references therein). Figure 1.4 shows $\omega(q)$ in the first (magnetic) BZ. The salient features are the linear low q behaviour discussed above, and the flattening off of the mode toward the zone boundary. It is worth noting that at q=0 the energy is zero, and hence the spin wave is a Goldstone mode. However, this is true only for an isotropic magnet, and an energy gap may appear at q=0 due to anisotropy.

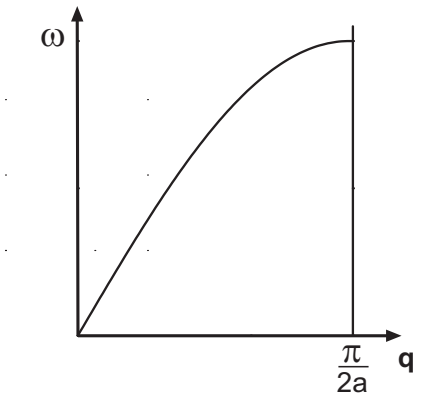

Figure 1.4: The dispersive behaviour (ω v. q) of a spin wave on a linear antiferromagnetic chain, with inter-spin separation a.

1.2 Quantum phase transitions and quantum magnetism

In magnetic phase transitions there is a characteristic finite transition temperature below which the system becomes magnetically ordered, and above this transition temperature thermal fluctuations are too large for the ordered state to be maintained. However, there are physical parameters other than temperature that may sometimes induce a magnetic transition. One of the most prominent examples of this is pressure, both applied or chemically induced (by doping). In this scenario, the induced phase transition can, in principle, occur in the limit $T \rightarrow 0$ K. This is classed as quantum critical behaviour, and the point which separates the two distinct zero temperature phases is called a quantum critical point. In contrast to normal phase transitions, quantum phase transitions are not driven by thermal fluctuations but by quantum fluctuations (see, for example, references [67, 68, 70]).

A quantum magnet is defined as a magnetic system in which the behaviour is dominated by quantum fluctuations. The fluctuations may arise from a combination of low dimensionality, low spin (s=1/2 or 1) and/or geometrically frustrated moments. Many different classes of quantum magnets have been theoretically and

experimentally investigated, some of which are mentioned in sections 1.2.1, 1.2.2 and 1.2.3. While a rich variety of systems are still at the forefront of condensed matter research, particular attention has focused on low dimensional Cu-O systems, motivated, in part, by the presence of two dimensional Cu-O layers in the high temperature superconducting cuprates [39, 50]. However, quantum spin systems are intriguing in their own right, with unique ground states and excitation spectra arising from both thermal and quantum fluctuations.

1.2.1 Low dimensionality

Low dimensional magnets are compounds which can be approximated by groups of magnetic ions that interact strongly along one axis (1 dimensional), or two axes (2 dimensional), but only weakly in the other directions. They demonstrate a wide range of complex quantum behaviour, but are conveniently described by relatively simple models. In this way they provide a limiting case for theoretical models, which can be directly compared with experimental results [82].

The Heisenberg Hamiltonian given in section 1.1.3 (see equation 1.3) has several useful limiting cases that depend upon the dimensionality of the spin vector. If the spins are confined to one dimension only (i.e. up or down along the z-axis), then we are in the limit of the *Ising Model*. If the spins are able to lie in the x-y plane, then we obtain the *X-Y model*. Finally, the case in which the spin vector has three dimensions, and the system is rotationally invariant, is known as the *Heisenberg model*. Heisenberg spins coupling along a single dimension form a Heisenberg spin chain [1]. Haldane first suggested that there is a qualitative difference between the excitation spectra of integer and half-integer Heisenberg chains [29]. In particular, he predicted the existence of a gap in s=1 Heisenberg chains between a singlet ground state and the first excited state, which is now known as the Haldane gap. In contrast, if the spin is half-integer then the system has a continuum of states [20, 56].

Spin ladders occupy a crossover region between 1D and 2D magnetism [12]. A two-leg spin ladder consists of two spin chains with the inter-chain exchange interaction comparable in magnitude to the intra-chain exchange interaction. One of the interesting effects observed in spin-$1/2$ two-leg ladders is a spin-gap in their energy spectrum [13]. This arises from the fact that two spins on the same 'rung' of the ladder (opposite from each other but on different chains, therefore interacting via the inter-chain exchange coupling), pair up to form a singlet state. This can be seen to extend to the case of all even-leg spin-$1/2$ ladders. This is not the case for odd-leg spin ladders, however, where there is a leftover electron on each rung preventing the ground state from becoming a non-magnetic singlet.

1.2.2 Frustration

Antiferromagnets usually align such that all neighbouring spins have opposite orientation. However, sometimes there are geometrical restrictions that do not allow this to happen. For example, for three spins situated at the corners of a triangle in an Ising-like system, there is no state that allows all of them to have the opposite spin orientation to their nearest neighbours. Another common example is that of tetrahedral spin-clusters, in which again there is no state that allows all of the neighbouring spin-spin interactions to minimise their energy by choosing a particular orientation of the spins (see figure 1.5). If this is the case, then the system is said to be **frustrated**. A compromise solution is required, and typically there is not a unique solution, but a large number of different states that result in the same classical ground state energy. Low energy quantum fluctuations, structural distortions or disorder can lift the classical degeneracy, resulting in a variety of interesting magnetic phenomena [18]. Experimentally, frustrated magnetic networks are realised in Kagomé and pyrochlore systems, which are lattices of corner sharing triangles and tetrahedra respectively. Many of these systems undergo a spin-glass transition [21] and some have also shown low-lying singlet, spin liquid and spin ice

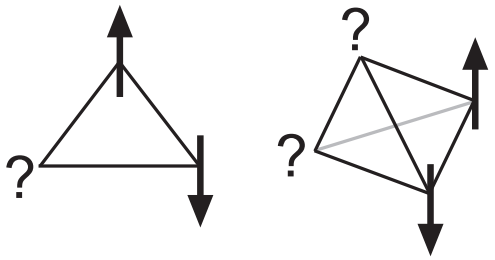

Figure 1.5: Frustrated antiferromagnetic coupling on (a) a triangle and (b) a tetrahedron.

ground states (see for example [63, 7, 11] and references therein).

1.2.3 Spin gaps and the spin-Peierls transition

An interesting characteristic of some quantum magnets is a finite gap in the magnetic excitation spectrum, known as a spin-gap. A famous example of the opening up of a spin-gap is via the spin-Peierls transition, which occurs in some Heisenberg s=1/2 antiferromagnets [20]. A well known example, and the first inorganic material in which the transition was observed, is $CuGeO_3$ [32]. In such systems, the linear magnetic chain can be described by a single exchange coefficient, J, above the spin-Peierls transition temperature, T_{SP}. However, below T_{SP} the chain distorts to form a dimerised antiferromagnetic chain with alternating exchange coefficients $J^{'}$ and $J^{''}$. This chain distortion corresponds to a physical distortion of the 3D lattice, with the spin-Peierls transition linked to magneto-elastic coupling. The transition causes an energy gap to open up between the singlet, non-magnetic ground state and the first excited triplet state of the system. The reduction in magnetic energy competes with the energy required to distort the lattice.

Spin gaps can exist for many reasons other than dimerisation. As described above, even-leg spin ladders have a spin gap in their energy spectrum, whilst spin-1 Heisenberg chains possess a Haldane gap [10, 48]. Further examples can be found in some frustrated materials and magnetic cluster systems [44, 38, 73, 40].

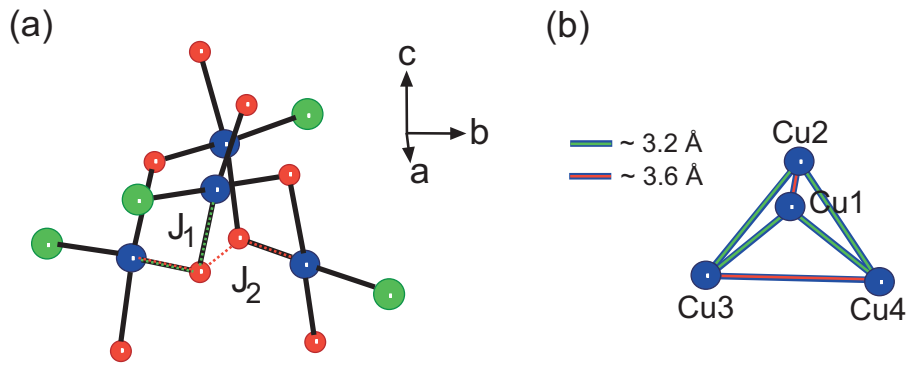

Figure 1.6: (a) In $Cu_2Te_2O_5X_2$, the Cu^{2+} ions are located at the vertices of $Cu_4O_8X_4$ tetrahedra. The Cu atoms are in blue, O in red and X (=Br or Cl) in green. J_1 is the superexchange interaction Cu-O-Cu (dotted green line), and J_2 is the super-superexchange interaction Cu-O··O-Cu (dotted red line). (b) The tetrahedra are slightly distorted with the Cu1-Cu2 and Cu3-Cu4 edges ($\sim$ 3.6 Å) slightly longer than the others ($\sim$ 3.2 Å).

1.3 Introduction to $Cu_2Te_2O_5(Br_xCl_{1-x})_2$

The low-lying excitations in spin triangular or tetrahedral lattice systems often lead to exotic magnetic behavior (see section 1.2.2). Recently, the copper oxyhalides $Cu_2Te_2O_5Br_2$ and $Cu_2Te_2O_5Cl_2$ have attracted particular attention as new examples of spin-tetrahedral systems. Sections 1.3.1 to 1.3.4 outline the important crystallographic and magnetic features of $Cu_2Te_2O_5X_2$, drawing widely from background literature on the subject.

1.3.1 Crystallographic structure of $Cu_2Te_2O_5(Br_xCl_{1-x})_2$

$Cu_2Te_2O_5X_2$ crystallises in the tetragonal $P\overline{4}$ space group [37]. The $Cu_2Te_2O_5X_2$ structure may be described in terms of $Cu_4O_8X_4$ tetrahedral clusters, with four spin-$1/2$ Cu^{2+} ions situated at the positions Cu1 (x, y, z), Cu2 ($1-x$, $1-y$, z), Cu3 (y, $1-x$, $-z$), Cu4 ($1-y$, x, $-z$), where $x \approx 0.73$, $y \approx 0.45$, $z \approx 0.16$. This is an irregular tetrahedron, with the Cu1-Cu2 and Cu3-Cu4 edges slightly longer than the others (see figure 1.6). The tetrahedra form a chain-like arrangement

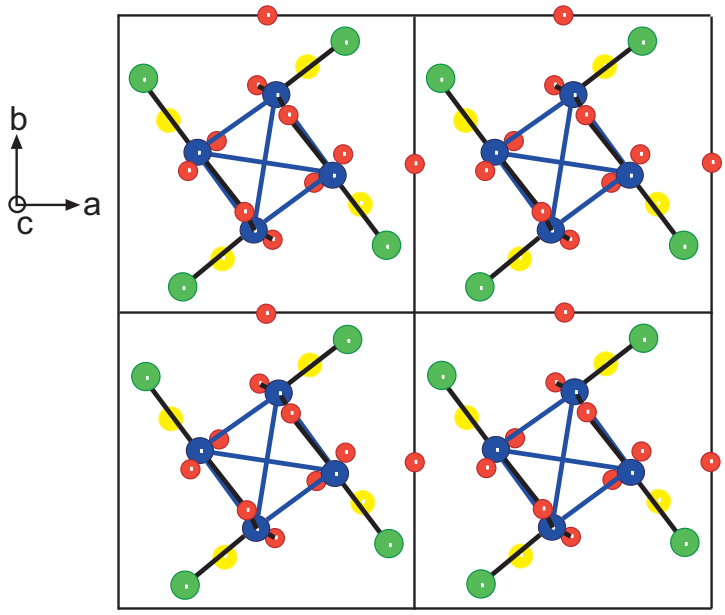

Figure 1.7: Crystallographic structure of $Cu_2Te_2O_5X_2$, projected onto the ab-plane. Cu atoms are in blue, O in red, X (=Br or Cl) in green and Te in yellow.

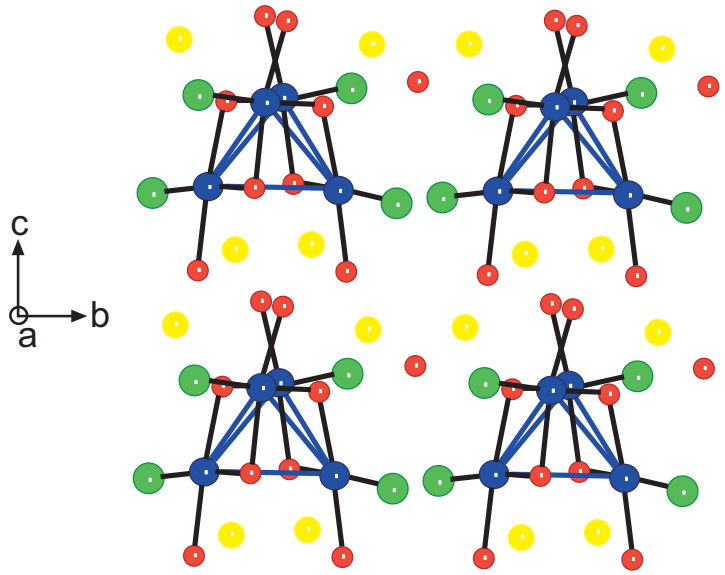

Figure 1.8: The Cu tetrahedra form chains along the c-axis, separated from each other by Te and O atoms (Cu atoms in blue, O in red, X (=Br or Cl) in green and Te in yellow).

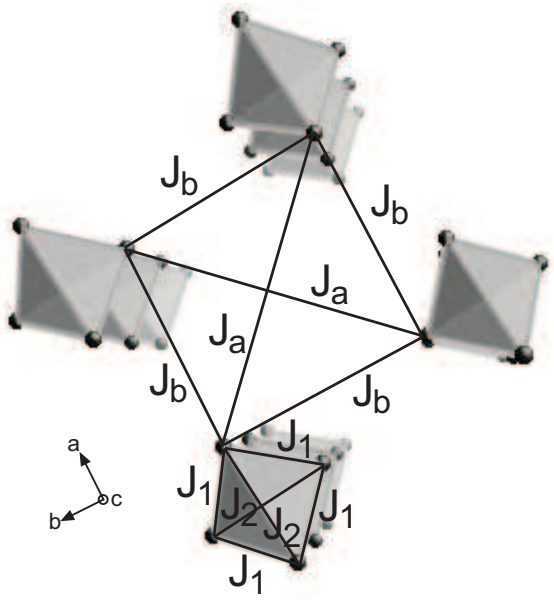

Figure 1.9: $Cu_2Te_2O_5X_2$ with four exchange interaction paths indicated; J_1 and J_2 are *intra*-tetrahedral whilst J_a and J_b are *inter*-tetrahedral.

along the c-axis, separated from each other by Te and O atoms (see figure 1.8). The a and c lattice parameters are, respectively, 3 % and 1 % bigger for X = Br than X = Cl, corresponding to a difference in unit cell volume of approximately 7 %. The unit cell volume of $Cu_2Te_2O_5(Br_xCl_{1-x})_2$ decreases linearly with substitution of Cl for Br, i.e. with decreasing x [45].

1.3.2 Magnetic exchange interactions in $Cu_2Te_2O_5(Br_xCl_{1-x})_2$

The magnetic species of interest in these compounds is the Cu^{2+} ion, in which an unpaired 3d electron carries a spin-1/2 moment. There are a number of possible exchange paths between the Cu^{2+} ions, which can be described with the help of figures 1.6 and 1.9 [78]. Firstly, there are two *intra*-tetrahedral exchange paths, J_1 and J_2 (see figure 1.6). J_1 is a super-exchange (SE) interaction via an oxygen atom, Cu-O-Cu, which operates between Cu atoms separated along the z-axis within the tetrahedra. J_2, on the other hand, links Cu ions with the same z-

coordinate and is a super-superexchange (SSE) interaction via two oxygen atoms; Cu-O··O-Cu. Secondly, there are several possible *inter*-tetrahedral exchange paths. Within the ab plane, there are two distinct SSE inter-tetrahedral paths via the halide atoms (Cu-X··X-Cu); J_a lies along the (110) direction and J_b lies either along the (100) or (010) direction. Between adjacent tetrahedra along the c-axis is the SSE path J_c, which is mediated by oxygen atoms (Cu-O··O-Cu). Figure 1.9 illustrates the intra-tetrahedral J_1 and J_2 interactions, and the J_a and J_b inter-tetrahedral exchange paths. In order to determine the relative strength of the exchange parameters one needs to examine the experimental data with respect to the exchange models. This is discussed further in section 1.3.4.

1.3.3 Macroscopic magnetic behaviour of $Cu_2Te_2O_5(Br_xCl_{1-x})_2$

Magnetic transition in $Cu_2Te_2O_5(Br_xCl_{1-x})_2$

Both $Cu_2Te_2O_5Br_2$ and $Cu_2Te_2O_5Cl_2$ show intriguing ground state properties, which, despite the compounds being isostructural, are surprisingly dissimilar. Anomalies have been observed in the temperature dependence of magnetisation [37, 46], heat capacity [46, 27] and thermal conductivity measurements [61, 69] at T_N^{Cl} =18.2 K and T_N^{Br}= 11.4 K for the Cl and Br compounds respectively. In the case of X=Cl, the field dependence of the transition at T_N^{Cl} is antiferromagnetic-like, with both the magnitude of the peak in heat capacity and the transition temperature decreasing slightly in an applied magnetic field. In contrast, in $Cu_2Te_2O_5Br_2$ the transition at T_N^{Br} shows a rather different field dependence, with both the magnitude and temperature of the transition *increasing* with increasing applied magnetic field. Moreover, thermal conductivity measurements reveal the behaviour of the X=Br compound to be highly anisotropic, with an increase in the transition temperature occurring when a magnetic field is applied parallel to the a-axis, but not occurring when the field is parallel to the c-axis. Behaviour such as

this has been observed in a few antiferromagnetic systems (see [69] and references therein), with the suggestion in some cases that it may be associated with the lowering of spin-dimensionality with applied field. If a similar argument is applied to $Cu_2Te_2O_5Br_2$ then one would expect the magnetic order below T_N^{Br} to have an easy axis along the c-axis.

Despite these differences, recent neutron diffraction studies [80] have revealed that the low temperature phases in both compounds correspond to an incommensurate magnetic order with similar propagation vectors, $\mathbf{k_{Cl}} \approx$[0.150,0.422,0.5] (X=Cl) and $\mathbf{k_{Br}} \approx$[0.158,0.345,0.5] (X=Br). The ground state magnetic order below T_N is rather complicated, and cannot be determined solely from measurements on polycrystalline materials. Single crystal measurements of the X=Cl sample reported by Zaharko et al. [80] show the magnetic structure to involve multiple helices, and the crystals to possess more than one domain. The magnetic structure proposed for the chloride consists of two canted pairs (Cu1-Cu2 and Cu3-Cu4) on each tetrahedron at cant angles of $\gamma_{12} = 38^o$ and $\gamma_{34} = 111^o$ respectively, and a Cu^{2+} moment value of $0.67\mu_B$/ion. The proposed magnetic structure is shown in figure 1.10, which is taken from reference [80].

Spin gap behaviour in $Cu_2Te_2O_5(Br_xCl_{1-x})_2$

Interestingly, the magnetisation of polycrystalline samples of both compounds reaches a maxima at $T \sim 25$ K before dropping sharply at low temperatures, most strikingly in the bromide. The sharp drop has been attributed to the presence of a singlet-triplet spin-gap [37, 46]. Single crystal ac susceptibility measurements reveal that this behaviour is anisotropic [61]. In $Cu_2Te_2O_5Br_2$, the susceptibility saturation level at low temperature is close to the value of the orbital susceptibility (Van Vleck paramagnetism + core electron diamagnetism) when the applied field is oriented parallel to the c-axis, which is consistent with a spin-singlet ground state. However, when the applied field is perpendicular to the c-axis, the saturation level

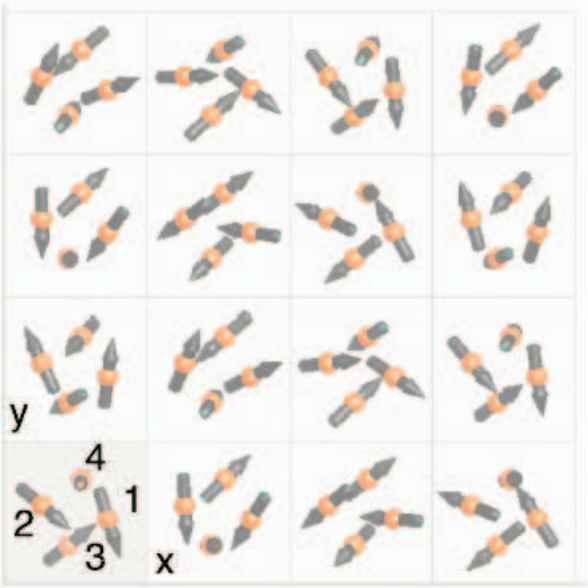

Figure 1.10: The proposed magnetic structure of $Cu_2Te_2O_5Cl_2$ projected on the xy-plane, based on a refinement of single crystal neutron diffraction data. The helical magnetic structure consists of two canting pairs of Cu^{2+} moments, Cu1-Cu2 and Cu3-Cu4. This has been taken from reference [80].

exhibits a pronounced sample dependence, typically saturating at a higher susceptibility than in the parallel geometry, which is inconsistent with a spin-gap state. In comparison, the susceptibility of $Cu_2Te_2O_5Cl_2$, whilst more isotropic, saturates at a relatively high level in both geometries with respect to the orbital susceptibility. The authors suggest that nonmagnetic impurities may play an important role in determining the ground state at low temperatures.

Further features and differences in the compounds have been probed by Raman scattering [46, 27, 35]. Whilst the Raman spectra of $Cu_2Te_2O_5Cl_2$ has no strong features at low energies, the bromide shows evidence of what is suggested to be a singlet-triplet excitation corresponding to a gap of $\sim$ 3.7 meV. Below T_N^{Br} a lower energy peak appears at $\sim$ 2.2 meV, which is associated with an excitation between a ground state singlet and a low lying excited singlet. Further Raman measurements in an applied magnetic field lead to the assertion by Gros et al. [27]

that the low energy peak at ~ 2.2 meV is a longitudinal magnon, and an additional peak observed at ~ 2.9 meV is associated with the excitation to a low lying singlet. The longitudinal magnetic mode is believed to hybridise with the singlet excitation due to a Dzyaloshinskii-Moriya anisotropy interaction [35].

The ground state instability of $Cu_2Te_2O_5(Br_xCl_{1-x})_2$

The above reported behaviour suggests the possible coexistence of long range order with a singlet ground state. Coexistence such as this has previously been observed in $Cu_{1-x}Zn_xGeO_3$ [49], where there is scope for disorder induced antiferromagnetic order in the gapped phase even for very small doping ($x \leq 0.005$). Fukuyama et al. [22] have also theoretically demonstrated the possibility of disorder induced antiferromagnetic order in doped $CuGeO_3$ spin-Peierls systems. A similar coexistence of magnetic order and a spin-gap may occur in this copper telluride system due to some small disorder. It is clear that there is a complicated interplay between the localised intra-tetrahedral interactions, which support spin-gapped behavior, and the inter-tetrahedral coupling that allows magnetic order to develop. The true nature of the ground state in these systems remains a question for further elaboration. In fact, the differences between the magnetic behaviour of $Cu_2Te_2O_5Br_2$ and $Cu_2Te_2O_5Cl_2$ have led some to argue that they lie either side of a quantum critical point [46, 27]. This has motivated the study of intermediate compounds $Cu_2Te_2O_5(Br_xCl_{1-x})_2$, with systematic doping of Cl for Br ($0 < x < 1$). The unit cell volume, transition temperature and phonon frequencies are found to vary smoothly with concentration x [27, 35, 45]. However, the Raman spectra shows a more abrupt change when substituting Cl for Br [45]. The low energy mode splits into several modes that shift to higher energy, and by $x \sim 0.7$ the low energy spectra looks like that of the Cl compound. Calculations of the susceptibility and bulk magnetisation in a mean field approximation by Jensen et al. [35] also indicate the possibility of an abrupt change in the magnetic order parameter around the

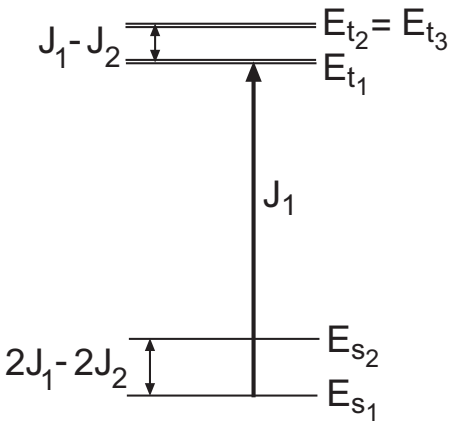

Figure 1.11: Energy level scheme of an independent tetrahedron with nearest neighbour interaction J_1, and next nearest neighbour interaction J_2.

composition $x \sim 0.75$.

1.3.4 Modelling the magnetic behaviour of $Cu_2Te_2O_5(Br_xCl_{1-x})_2$

One can model the magnetic structure of $Cu_2Te_2O_5X_2$ as isolated tetrahedra by neglecting the inter-tetrahedral coupling and considering only nearest neighbour (J_1) and next nearest neighbour (J_2) interactions. The ground state of this model is a spin singlet, which consists either of dimers or a quadrumer involving all four Cu atoms, depending on the relative strength of J_1 and J_2. Figure 1.11 shows the energy levels of an isolated tetrahedron with respect to J_1 and J_2, where E_{s1} and E_{s2} are the energy levels of the two singlet states, and E_{t1}, E_{t2} and E_{t3} are the triplet states. A good fit to magnetisation data [37] gives J_1=J_2, in which case the system has a nonmagnetic singlet ground state, an excited triplet state and a singlet-triplet spin-gap of magnitude J_1=J_2=$J \sim$ 43 K and 38.5 K for X = Br and Cl respectively.

With mean-field inter-tetrahedral coupling (J_{MF}) the two singlets of the independent tetrahedral model become a mixed ground state with a low lying excited state, which is identified with a longitudinal magnon [27]. Within the mean-

field approach a quantum critical point is predicted at the coupling magnitude $J_{MF} = J_{MF}^{qc} = 3J_1/4$, and a field-induced increase in the transition temperature T_N^{Br} is predicted for $Cu_2Te_2O_5Br_2$, in agreement with observed behaviour (see section 1.3.3). For calculations based on the theoretical case of tetrahedra coupled along a chain, two possible magnetic phases are identified [8, 74]; a singlet product phase in which each of the Cu1-Cu3 and Cu2-Cu4 pairs form a spin singlet, and a dimer phase in which each of the Cu1-Cu3 and Cu2-Cu4 pairs form a spin-triplet, but the overall plaquette is a spin singlet. In both phases, low lying singlet excitations are predicted to reside in the 'gap' region between the ground state singlet and excited triplet states. Whilst in the former phase these low lying excitations are expected to be dispersionless, in the dimer phase there may also be dispersive low lying modes. However, the phase adopted by $Cu_2Te_2O_5X_2$ is determined by the relative strength of its exchange couplings, which is comprehensively addressed in references [75] and [78]. Both argue that the intercluster super-superexchange paths Cu-X··X-Cu along the (110) direction and the (100) and (010) directions (denoted J_a and J_b respectively in figure 1.9) are significant. In particular, the halogen atoms play a key role in the exchange due to the large extension of the Cl 3p and Br 4p wave functions, which become involved in a covalent Cu-O-Cl(Br) network. Whangbo et al. estimate the relative strength of the exchange parameters in both compounds by spin dimer analysis, predicting (see figure 1.9);

$J_a > J_1 \geq J_b > J_2$ for X=Cl.

$J_a > J_b \gg J_1 > J_2$ for X=Br.

Finally, further work [35, 42] suggests the importance of antisymmetric Dzyaloshinsky-Moriya (DM) spin-spin interactions, which in a tetrahedral system can induce weak antiferromagnetic order from a singlet background. However, without further experimental evidence it remains difficult to ascertain which model, or exchange coupling configuration most closely describes $Cu_2Te_2O_5Br_2$ and $Cu_2Te_2O_5Cl_2$.

Chapter 2

Experimental Techniques

2.1 Sample characterisation

2.1.1 Magnetisation measurements

The magnetisation measurements reported in this work have been carried out using a Quantum Design MPMS-5S SQUID magnetometer, shown schematically in figure 2.1. The temperature control system allows measurements between 1.8 and 400 K, whilst the magnet can provide a field of up to 50 kOe. The SQUID itself consists of a superconducting ring with two Josephson junctions, and acts effectively as an extremely high sensitivity flux-to-voltage converter. It is shielded from external fields (in particular that of the superconducting solenoid), and coupled inductively to the detection coils. As the sample is moved through the pick-up coils, the SQUID voltage is measured at a number of sample positions along the scan. This SQUID response is fitted to the theoretical signal from a point-source magnetic dipole using an iterative regression algorithm, and the moment of the sample is then extracted. SQUID magnetometers are capable of measuring very small magnetic moments; the instrument used in this work has a resolution of 5×10^{-8} emu.

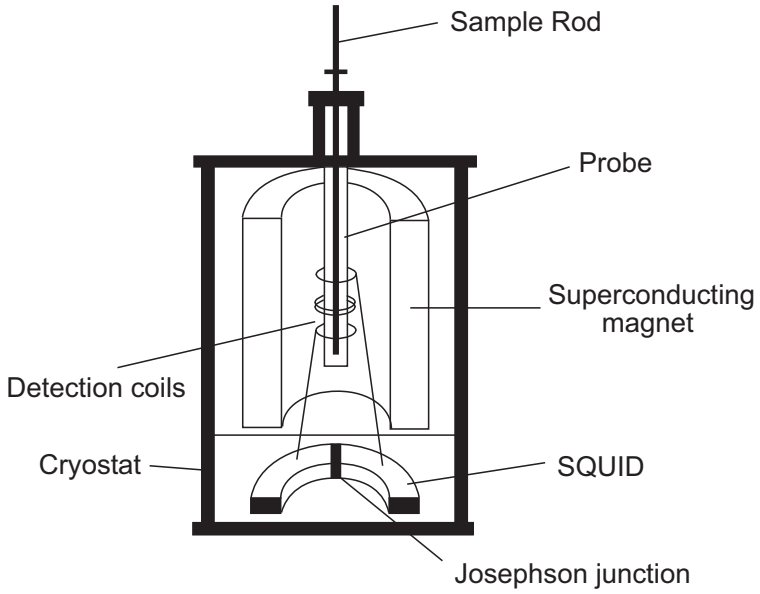

Figure 2.1: Schematic diagram of the Quantum Design SQUID magnetometer. The sample is moved vertically through pick-up coils, inducing a response in the SQUID that can be fitted to give the magnetisation of the sample. Extremely small magnetic moments can be resolved by this highly sensitive device.

2.1.2 Heat capacity measurements

A Quantum Design physical property measurement system (PPMS) has been used to carry out heat capacity measurements. The PPMS utilises the heat pulse relaxation technique, and is capable of measuring at temperatures from 0.4 to 350 K, and in fields of up to 90 kOe. The sample is mounted on a platform containing a heater and thermometer, which is in well defined thermal contact with a heat capacity puck (also containing a thermometer). The temperature of both sample platform and puck are stabilised to an initial temperature, T_0. Power is then supplied to the platform heater for a given amount of time in order to raise the temperature of the platform to T_1. Once the heater is switched off, the temperature of the sample platform relaxes back to the puck temperature, T_0. The decay of the platform temperature is exponential, with a time constant that depends upon the thermal conductance of the wires through which the heat flow

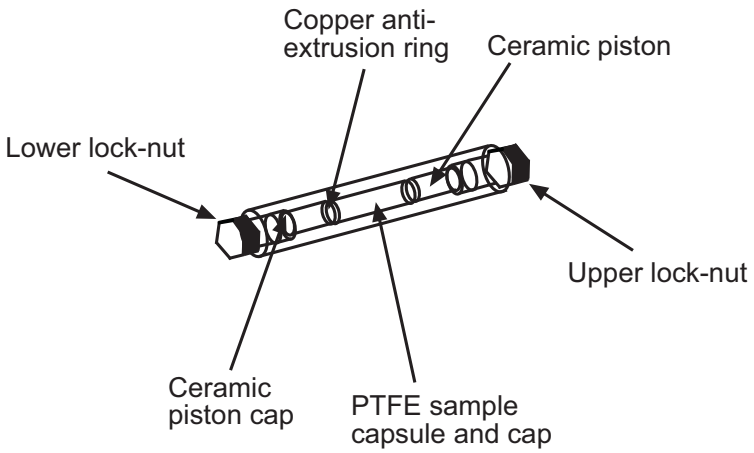

Figure 2.2: Schematic diagram of the easyLab Mcell 10 pressure cell.

is transmitted (which is known), and the heat capacity of the sample. In this way, fitting of the temperature relaxation curve can be used to determine the heat capacity of the sample.

2.2 Pressure measurements

Magnetisation measurements under an applied external pressure have been performed using an easyLab Technologies Mcell 10 pressure cell, which can be used in a Quantum Design SQUID magnetometer to measure the bulk magnetisation of samples under pressures of up to 10 kbar. The cell is made of an alloy with low magnetic background and, using the automatic background subtraction feature available on the Quantum Design MPMS SQUID magnetometer, measurements of samples with magnetic moments as low as 5×10^{-6} emu are possible. Figure 2.2 is a schematic diagram of the Mcell 10 pressure cell. The sample is placed in a PTFE capsule and the cell is filled with Daphne oil, which acts as the pressure medium. The sample space is approximately 1.9 mm in diameter and 10mm long. A small piece of Sn is also placed in the capsule. The superconducting transition temperature of Sn is well known as a function of pressure, and therefore the *in*

situ pressure can be measured using the Sn manometer. The sample capsule is placed between two ceramic pistons and fastened by end lock-nuts. Hydrostatic pressure is then applied to the sample using a hydraulic press and the pressure is maintained by tightening the upper lock nut.

For both the inelastic and elastic neutron scattering measurements performed under pressure, a similar clamp cell was used. The cell was made from a hardened beryllium-copper alloy, with a 6mm diameter x 40mm long sample volume. The pressure medium was Fluorinert (C8F18). Again, pressure was generated using a 50 tonne hydraulic press and subsequently locked in by an external lock-nut. In these measurements a NaCl crystal was used as the manometer, utilising the fact that the lattice parameter of NaCl as a function of pressure is well known.

2.3 Neutron scattering

Neutron scattering is well established as an experimental technique for studying the structural and dynamic properties of materials. The theoretical foundations of neutron scattering will only briefly be discussed in this chapter, with a far more comprehensive coverage of the subject available in a host of texts, including references [71, 3, 47, 51, 4, 57]. More emphasis will be placed on the specific techniques, instrumentation and analysis methods utilised in this work (sections 2.3.3 to 2.3.6).

2.3.1 Theoretical foundations

Neutron scattering cross sections

Consider a beam of neutrons with incident energy E_i and incident wave vector $\mathbf{k_i}$, some of which scatters from a sample into a new state with energy E_f and wave vector $\mathbf{k_f}$. Figure 2.3 shows the scattering geometry of an event such as this. The

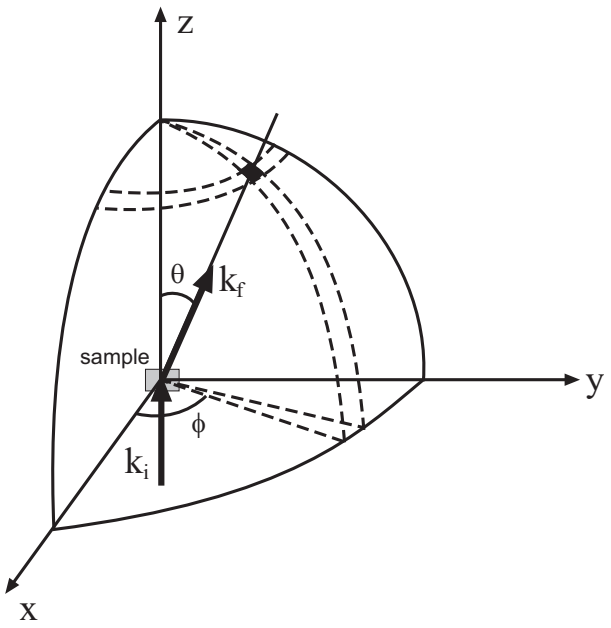

Figure 2.3: Scattering geometry for neutrons scattered from a sample in the direction θ, ϕ

number of neutrons scattered per second into a small solid angle ($d\Omega$) in the direction θ, ϕ, with final energy between E_f and dE_f, is given by the partial differential cross section, $\frac{d^2\sigma}{d\Omega dE_f}$. This is the measurable quantity in scattering experiments, from which details of the underlying structure and dynamics of the sample can be extracted by using a suitable theoretical expression for the cross section. In general, the nuclear partial differential cross section of neutron scattering from an assembly of nuclei at positions $\mathbf{r_j}$ can be expressed by

$$\frac{d^2\sigma}{d\Omega dE_f} = \frac{1}{2\pi\hbar}\frac{k_f}{k_i}\sum_{jj'} b_j b_{j'} \int \left\langle e^{-i\mathbf{Q}\cdot\mathbf{r_{j'}}(0)} e^{i\mathbf{Q}\cdot\mathbf{r_j}(t)} \right\rangle e^{-i\omega t} dt, \tag{2.1}$$

where $\mathbf{Q} = \mathbf{k_i} - \mathbf{k_f}$ is the scattering vector, k_i and k_f are the magnitudes of the initial and final wavevectors of the neutrons respectively, b_j is the scattering length of the j^{th} nuclei (see below), and the brackets $\langle ... \rangle$ denote an average over all possible thermodynamic states of the sample. A derivation of equation 2.1 can be found in many texts on the subject (see, for example, reference [71]).

Coherence and incoherence

When an incident plane wave scatters from a single nucleus, the scattered wave is spherically symmetric and its amplitude is given by the *scattering length*, b. The value of b varies from element to element, and also depends on the isotope and the spin state of the nucleus. This means that if the nuclei of a sample have non-zero spin, or if different isotopes are present, then there will be a spread of scattering lengths in the sample even if only one element is present. If this is the case, then scattered neutrons from different nuclei will have different phases, which gives rise to two scattering terms, namely *coherent* and *incoherent*. The coherent scattering term can be thought of as that which would arise from the system if all of the scattering lengths were equal to the average scattering length, $\overline{b}$. The incoherent term arises from the random variation of the scattering lengths about this mean value. Expressions for the total coherent and incoherent cross sections are given below.

$$\sigma_{coh} = 4\pi(\overline{b})^2 \tag{2.2}$$

$$\sigma_{inc} = 4\pi(\overline{b^2} - (\overline{b})^2) \tag{2.3}$$

Pair correlation functions

Often an instructive way of expressing cross sections such as equation 2.1, is by use of *correlation functions*. Equation 2.1 can be rewritten as [34]

$$\frac{d^2\sigma}{d\Omega dE_f} = \sum_{jj'} b_j b_{j'} \frac{k_f}{k_i} S(\mathbf{Q}, \hbar\omega), \tag{2.4}$$

by introducing the scattering function,

$$S(\mathbf{Q}, \hbar\omega) = \frac{1}{2\pi\hbar} \int G(\mathbf{r}, t) e^{i(\mathbf{Q}\cdot\mathbf{r} - \omega t)} d\mathbf{r} dt, \tag{2.5}$$

and the time-dependent pair correlation function,

$$G(\mathbf{r}, t) = \left(\frac{1}{2\pi}\right)^3 \int \sum_{jj'} e^{-i\mathbf{Q}\cdot\mathbf{r}} \left\langle e^{-i\mathbf{Q}\cdot\mathbf{r}_{\mathbf{j}'}(0)} e^{i\mathbf{Q}\cdot\mathbf{r}_{\mathbf{j}}(t)} \right\rangle d\mathbf{Q}. \tag{2.6}$$

The pair correlation function, $G(\mathbf{r}, t)$, gives the probability of finding an atom at position $\mathbf{r}$ at time t, given that there is an atom at the origin at time t=0. The scattering function, $S(\mathbf{Q}, \hbar\omega)$, is the Fourier transform of the time dependent pair correlation function and provides the link between the scattering data and the physical system being studied.

Magnetic neutron scattering

Neutrons are spin-1/2 particles with a magnetic moment. Therefore as well as scattering from the nuclei (as described above), neutrons also interact with magnetic ions in the sample via the dipole interaction. The magnetic ion does not act as a point-like scattering source, hence magnetic neutron scattering is attenuated by the square of a magnetic form factor, $f_m(\mathbf{Q})$, which depends upon the scattering vector, $\mathbf{Q}$. A form factor is essentially the Fourier transform of the real space magnetisation density, and they are tabulated for a large number of free magnetic ions in the International tables of Crystallography [9]. The magnetic scattering amplitude, $\mathbf{b_M}$, is more complicated than its nuclear counterpart, b, because of the nature of the dipole interaction between the neutrons and magnetic ions. The scattering amplitude vector is given by

$$\mathbf{b_M}(\mathbf{Q}) = p f_m(\mathbf{Q}) \mathbf{m}_\perp, \tag{2.7}$$

where $\mathbf{m}_\perp$ is the perpendicular component of the moment, $\mathbf{m}$, of the magnetic ions in the sample, and in general p is given by

$$p = \gamma r_0 S, \tag{2.8}$$

where γ is the gyromagnetic ratio, r_0 is the classical radius of the electron and S is the spin of the magnetic ion. Equation 2.7 highlights an important fact in magnetic neutron scattering; only the spin component perpendicular to the scattering vector contributes to the magnetic scattering cross section.

In an analogous fashion to the nuclear case (see section 2.3.1), one can derive an expression for the partial differential magnetic cross section with respect to a scattering function, which is the Fourier transform of the magnetic pair correlation function. In the magnetic case, the spin polarisation of the neutrons must be considered, as must the magnetic degrees of freedom of the unpaired electrons, rendering the problem rather more complicated than for nuclear scattering. Many textbooks comprehensively cover the subject [51, 47, 71]. Here, a rather specific example of an inelastic magnetic cross section will be shown, which bears significance to the results presented in this thesis (see chapter 5). Consider a material containing isolated regular clusters of magnetic ions with an intra-cluster ion separation of R. Let there be a well-defined transition between two exchange-split ground state levels, E_1 and E_2, of the cluster system. For this scenario, the magnetic scattering cross section for a transition between states E_1 and E_2 in a polycrystalline sample can be expressed as (see reference [23])

$$\left(\frac{d^2\sigma}{d\Omega dE_f}\right)_{E_1\rightarrow E_2} \sim e^{-\frac{E_2-E_1}{k_bT}}\ e^{-2W(|\mathbf{Q}|)} f_m^2(|\mathbf{Q}|)\mathcal{M}\left(1-\frac{\sin(|\mathbf{Q}|R)}{|\mathbf{Q}|R}\right). \quad (2.9)$$

where k_B is the Boltzmann constant, $W(|\mathbf{Q}|)$ is the Debye-Waller factor (see section 2.3.3) and $\mathcal{M}$ denotes an expression containing the matrix elements of the transition, which are $|\mathbf{Q}|$-independent and not discussed here (see reference [23] for details). Of interest in this thesis is the last term, which is a $|\mathbf{Q}|$-dependent interference term characterised by the ion separation R. This oscillatory term in $|\mathbf{Q}|$ is convoluted with the form factor to give an overall $|\mathbf{Q}|$-dependence in which the oscillations dampen at larger $|\mathbf{Q}|$.

As a final comment it is worth noting that, whilst the mechanisms behind nuclear and magnetic scattering are entirely different, their cross sections are fortuitously of the same magnitude, allowing simultaneous measurement of the magnetic and chemical behaviour of materials.

2.3.2 Neutron sources

There are two widely used methods of producing neutrons for scattering experiments. Firstly, a nuclear reactor can produce neutrons by the fission of ^{235}U. To sustain the fission process a moderator is required in order to slow down the neutrons, and the neutron energy with peak flux is determined by the moderator temperature. For example, a moderator temperature of 290 K corresponds to a peak neutron energy of $\sim$ 25 meV, and wavelength 1.8 Å. This, fortuitously, coincides with the typical length scale of interatomic separations, and hence the moderation process both maintains fission and provides neutrons of appropriate energies for scattering experiments. The neutron flux produced by a reactor is constant in time and covers a range of wavelengths. The neutron beam can be monochromated to give a very narrow range of wavelengths for use in a scattering experiment. The reactor source used for experiments reported in this thesis was the Institut Laue Langevin (ILL) high flux reactor in Grenoble, France.

The second method for producing neutrons is by spallation. In this technique a beam of protons is accelerated to high energies using a synchrotron, and fired at a heavy metal target. The protons collide with the nuclei of the target and through the nuclear process known as spallation, high energy nucleons are emitted. These particles may in turn collide with the nuclei of the target leading to a cascade effect and in all 20 - 30 neutrons may be emitted for each proton incident on the target. The neutrons are moderated in order to bring them to suitable scattering energies. Often spallation sources operate in a pulsed mode, typically with a pulse rate of about 50 Hz, which allows for the use of a technique known as *time-of-flight*. In the time-of-flight method a white beam (containing neutrons with a continuous distribution of wavelengths) is used, and the time (t) taken for a neutron to travel the flight path (L) from the moderator to the sample and on to the detectors is measured. The final wave vectors of scattered neutrons can then be determined by their time of flight, given in the case of elastic scattering

by

$$|\mathbf{k_f}| = \frac{m_n L}{\hbar t}, \tag{2.10}$$

where m_n is the mass of the neutron. The spallation source utilised in the work of this thesis was ISIS at the Rutherford Appleton Laboratory, UK.

2.3.3 Neutron diffraction

In neutron diffraction, structural information about the sample can be extracted from the coherent elastic differential cross section. In the case of nuclear diffraction, equation 2.1 can be reduced to (see for example [51]),

$$\left(\frac{d\sigma}{d\Omega}\right)_{nucl} \propto \sum_{\boldsymbol{\tau}} \delta(\mathbf{Q} - \boldsymbol{\tau}) |F_N(\mathbf{Q})|^2, \tag{2.11}$$

where $\boldsymbol{\tau}$ is the reciprocal lattice vector and $F_N(\mathbf{Q})$ is the nuclear structure factor, given by

$$F_N(\mathbf{Q}) = \sum_j b_j \; e^{i\mathbf{Q}\cdot\mathbf{d_j}} \; e^{-2W_j(|\mathbf{Q}|)}. \tag{2.12}$$

Here, $\mathbf{d_j}$ is the position of the j^{th} atom in the unit cell, and $W_j(|\mathbf{Q}|)$ is the Debye-Waller factor. The Debye-Waller factor incorporates the damping of Bragg scattering due to dynamic and static displacements of the scattering objects about their average positions. The δ-function in equation 2.11 corresponds to the well-known Bragg's law, which states that the nuclear scattering peaks occur when the scattering vector is equal to the reciprocal lattice vector.

In a similar manner, it can be shown that the magnetic structure factor is given by

$$\mathbf{F}_{\perp\mathbf{M}}(\mathbf{Q}) = \sum_j \mathbf{b_{Mj}}(\mathbf{Q}) \; e^{i\mathbf{Q}\cdot\mathbf{d_j}} \; e^{-2W_j(|\mathbf{Q}|)}. \tag{2.13}$$

In the particular case of an incommensurate helical magnetic structure, which is relevant to the work in this thesis, the cross section of elastic magnetic scattering [71] is given by the expression

$$\left(\frac{d\sigma}{d\Omega}\right)_{helical} \propto \sum_{\boldsymbol{\tau}} \delta(\mathbf{Q} + \boldsymbol{\kappa} - \boldsymbol{\tau}) \delta(\mathbf{Q} - \boldsymbol{\kappa} - \boldsymbol{\tau}) |\mathbf{F}_{\perp\mathbf{M}}(\mathbf{Q})|^2, \tag{2.14}$$

where $\boldsymbol{\kappa}$ is the modulation wave vector that defines the periodicity of the helical spin arrangement. In this case the δ-function indicates that magnetic Bragg scattering occurs when the scattering vector is equal to $\boldsymbol{\tau} \pm \boldsymbol{\kappa}$. This corresponds to a diffraction pattern that contains satellite peaks at a vector $\boldsymbol{\kappa}$ either side of each nuclear Bragg peak.

Neutron diffractometers

In reality, the intensity arising from Bragg scattering does not occur at a point in reciprocal space, but as a small three dimensional ellipsoid that extends over a finite range in 3D $\mathbf{Q}$-space. This is due to a combination of mosaic spread of the sample and finite instrumental resolution. In one-dimensional measurements, the Bragg scattering therefore appears as a peak with finite width. By counting the scattered neutrons from the extended range of the peak, the integrated intensity of the Bragg reflection (I_{hkl}) can be calculated. Two different methods of diffraction have been utilised in this thesis; single crystal and polycrystalline diffraction using constant wavelength neutrons.

The single crystal diffraction work presented in this thesis was carried out on the D10 four-circle diffractometer at the ILL reactor, Grenoble. Figure 2.4 is a schematic diagram of the instrument. Firstly the neutron beam is monochromated to produce a predominantly single wavelength beam, which is incident on a sample mounted on a Eulerian cradle. There are three axes of rotation for the crystal (ω, ϕ, χ), and one for the detector (2θ). The reciprocal lattice of the crystal is oriented with respect to the instrument and the beam via an orientation matrix. The detector is placed at the correct 2θ value to satisfy the Bragg condition for a given reflection (hkl), and the crystal is then rotated through this condition so that the detector sees the full width of the finite Bragg reflection, and the integrated intensity of the peak, I_{hkl}, is measured. Further reflections can subsequently be measured by orienting the sample and detector such that the Bragg condition

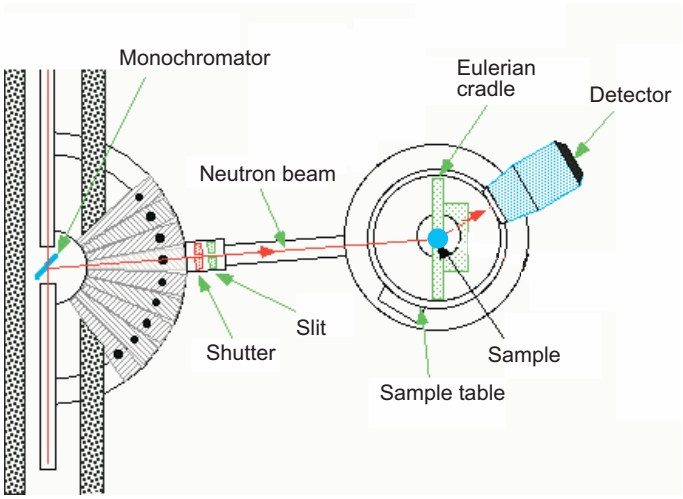

Figure 2.4: Schematic of D10, a four circle diffractometer at the ILL, Grenoble. This figure has been adapted from that provided on the D10 instrument website, http://www.ill.fr

for the new reflection is satisfied. The detector on D10 is a two dimensional area detector, which effectively measures two-dimensional slices through the three dimensional Bragg ellipsoid.

The second diffraction technique utilised in this work is the scattering of a monochromatic beam of neutrons from a polycrystalline sample. A polycrystalline (powder) sample essentially consists of a very large number of small single crystals randomly oriented with respect to each other. This means that the cross section for scattering is averaged over all orientations of $\mathbf{Q}$. It can be shown (see for example reference [47]) that all neutrons with a final wave vector that lies on a cone in reciprocal space, known as the Debye-Scherrer cone, contribute to Bragg scattering at $|\mathbf{Q}|$. Figure 2.5 shows the geometry of the Debye-Scherrer cone for Bragg scattering, which has its axis along $\mathbf{k_i}$ and a semi-angle, θ, that satisfies $\cos\theta = 1 - |\mathbf{Q}|^2/2|\mathbf{k_i}|^2$. The polycrystalline measurements reported in this thesis were performed on the D20 high flux powder diffractometer at the ILL, France. A photo of D20 is shown in figure 2.6. The instrument is equipped with a large position sensitive detector (PSD) that covers an area of about 4 m long by 150

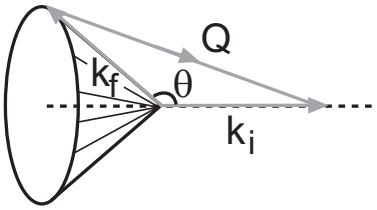

Figure 2.5: Bragg scattering from a polycrystalline sample occurs when the wave vectors of the scattered neutrons lie on a Debye-scherrer cone

mm high, corresponding to over 150^o coverage of the scattering angle. The PSD consists of microstrip plates in a very precise detector geometry, which provides a homogeneous and stable detector response. The high flux of the instrument aids the observation of weak magnetic peaks, which was important in this work.

2.3.4 Magnetic structure refinements

When a set of integrated intensities for a number of magnetic Bragg reflections have been collected in a single crystal diffraction experiment, or an intensity profile as a function of 2θ has been collected in a powder diffraction experiment, the magnetic structure may be *refined*. That is, a model of the magnetic structure can be proposed and refined such that it gives the best fit to the experimental data, using a least squares or simulated annealing algorithm. The Commission on Powder Diffraction of the International Union of Crystallography has published guidelines for refinements [54]. In this thesis the refinement program FULLPROF, created by J. Rodriguez-Carvajal, has been used [65, 66].

The magnetic structure can be related to the measured positions and integrated intensities of Bragg reflections using the following formulae. Firstly, the integrated intensity of a Bragg reflection is proportional to the square of its structure factor [30],

$$I(\mathbf{Q}) \propto |\mathbf{F}_{\perp\mathbf{M}}(\mathbf{Q})|^2 = |\mathbf{F}_{\mathbf{M}}(\mathbf{Q})|^2 - \left|\frac{\mathbf{Q}\cdot\mathbf{F}_{\mathbf{M}}(\mathbf{Q})}{|\mathbf{Q}|}\right|^2. \qquad (2.15)$$

Here, $\mathbf{F}_{\mathbf{M}}$ is the full structure factor, which is expressed in terms of the mag-

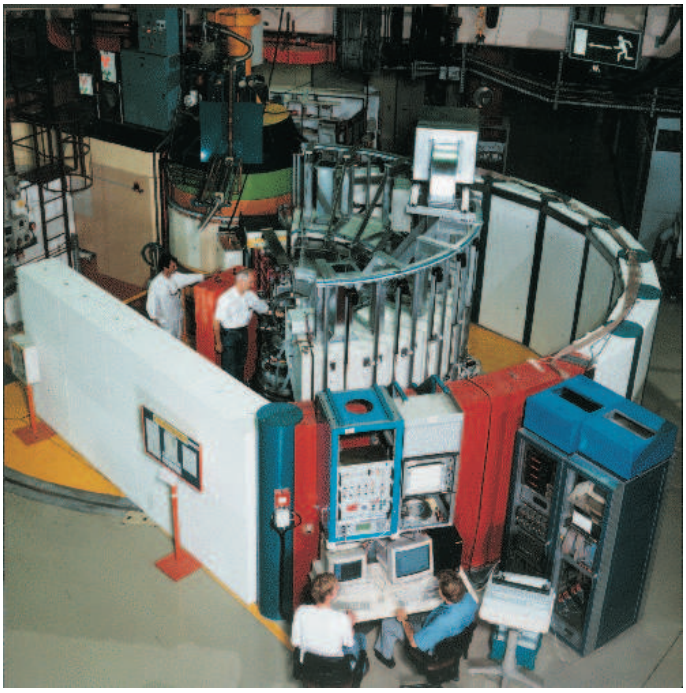

Figure 2.6: Photo of D20, a high flux powder diffractometer at the ILL, Grenoble. This has been taken from the D20 instrument website, http://www.ill.fr

netic moments of the sample rather than their perpendicular components (see equations 2.7 and 2.13),

$$\mathbf{F_M}(\mathbf{Q}) = pf_m(\mathbf{Q}) \sum_j \mathbf{m}_j e^{-2W_j}(\mathbf{Q}) e^{i\mathbf{Q}\cdot\mathbf{d_j}}, \tag{2.16}$$

where p is defined in equation 2.8. In general, the distribution of magnetic moments in a given periodic magnetic structure can be expanded as a Fourier series;

$$\mathbf{m}_{nj} = \sum_{\boldsymbol{\kappa}} \mathbf{S}_{\boldsymbol{\kappa}j} e^{-2\pi i \boldsymbol{\kappa}\cdot\mathbf{R}_n}, \tag{2.17}$$

where $\mathbf{m}_{nj}$ is the moment vector of the jth atom in the nth unit cell, and $\boldsymbol{\kappa}$ is the magnetic propagation vector. The Fourier components $\mathbf{S}_{\boldsymbol{\kappa}j}$ are complex vectors, which, in order to ensure real moments, obey the condition $\mathbf{S}_{-\boldsymbol{\kappa}j} = \mathbf{S}^*_{\boldsymbol{\kappa}j}$. Finally, substituting equation 2.17 (using $\mathbf{m_{0j}}$) into equation 2.16 gives

$$\mathbf{F_M}(\boldsymbol{\tau} + \boldsymbol{\kappa}) = pf_m(\mathbf{Q}) \sum_j \mathbf{S}_{\boldsymbol{\kappa}j} e^{-2W_j}(\mathbf{Q}) e^{2\pi i(\boldsymbol{\tau}+\boldsymbol{\kappa})\cdot\mathbf{d_j}}. \tag{2.18}$$

From equations 2.15 and 2.18 it is clear that the Fourier components of the magnetic structure, $\mathbf{S}_{\boldsymbol{\kappa}j}$, are accessible from the scattering intensities of neutron diffraction. Taking the example of an incommensurate magnetic structure (relevant to the work in this thesis), the Fourier components can be expressed as

$$\mathbf{S}_{\boldsymbol{\kappa}j} = \frac{1}{2}[\mathbf{A}_j + i\mathbf{B}_j]e^{-2\pi i\psi_{\boldsymbol{\kappa}j}}, \tag{2.19}$$

which, when expanded in equation 2.17, leads to the following expression for the magnetic moments

$$\begin{aligned} \mathbf{m}_{nj} &= \mathbf{S}_{\boldsymbol{\kappa}j}e^{-2\pi i\boldsymbol{\kappa}\cdot\mathbf{R}_n} + \mathbf{S}_{-\boldsymbol{\kappa}j}e^{2\pi i\boldsymbol{\kappa}\cdot\mathbf{R}_n} & (2.20)\\ &= \mathbf{A}_j\cos 2\pi(\boldsymbol{\kappa}\cdot\mathbf{R}_n + \psi_{\boldsymbol{\kappa}j}) + \mathbf{B}_j\sin 2\pi(\boldsymbol{\kappa}\cdot\mathbf{R}_n + \psi_{\boldsymbol{\kappa}j}). & (2.21)\end{aligned}$$

Here, $\mathbf{A}_j$ and $\mathbf{B}_j$ are orthogonal vectors that define the axes of the modulation on the jth atom, and $\psi_{\boldsymbol{\kappa}j}$ its phase (see for example reference [33]).

In the refinement process of polycrystalline magnetic scattering, the measured intensity profile is recorded in discrete steps of scattering angle, T_i, and can be expressed in the form $\{T_i, y_i, \sigma_i\}_{i=1,\ldots,n}$, where σ_i is the standard deviation of the intensity y_i at the scattering angle T_i. This is compared with the calculated intensity at T_i, $y_{c,i}$, which is given by

$$y_{c,i} = S\sum_{\boldsymbol{\tau}+\boldsymbol{\kappa}} I_{\boldsymbol{\tau}+\boldsymbol{\kappa}}\Omega(T_i - T_{\boldsymbol{\tau}+\boldsymbol{\kappa}}) + b_i, \tag{2.22}$$

where S is a scale factor, Ω is the profile (peak shape) function (for example, Gaussian, Voigt or pseudo-Voigt) that incorporates both instrumental and sample effects, b_i is the background intensity and

$$I_{\boldsymbol{\tau}+\boldsymbol{\kappa}} = (L|\mathbf{F}_{\perp\mathbf{M}}|^2)_{\boldsymbol{\tau}+\boldsymbol{\kappa}}. \tag{2.23}$$

L corrects for the Lorentz geometric correction factor, defined by

$$L = \frac{1}{2\sin\theta\sin 2\theta}\ . \tag{2.24}$$

In the Rietveld least squares method of refinement [64], the model structure is refined by minimising the following chi-square function with respect to a list of parameters, $\boldsymbol{\alpha}$ (that define the Fourier components $\mathbf{S}_{\boldsymbol{\kappa}j}$)

$$\chi^2 = \sum_i \frac{1}{\sigma_i^2} \left\{ y_i - y_{c,i}(\boldsymbol{\alpha}) \right\}^2 . \tag{2.25}$$

For single crystal (integrated intensity) refinements, the function to be optimised in the refinement is

$$\sum_n \frac{1}{\sigma_n^2} (G_{obs,n}^2 - \sum_k G_{calc,k}^2)^2, \tag{2.26}$$

where G^2 is the square of the magnetic structure factor corrected for the Lorentz factor, which in the case of Eulerian cradle geometry is given by $L = \frac{1}{\sin 2\theta}$, n is the index of the observation and k indexes the different reflections contributing to the observation. There are a number of ways of defining the quality of the refinement in terms of reliability or agreement factors. These generally fit in one of two categories; (i) those which give a measure of the quality of the structural model independently from the profile, which are known as crystallographic factors and (ii) those which intend to quantify the quality of the overall profile fitting, which are known as profile factors. It is useful to monitor both types of factors in the refinement procedure in order to know not just how well the calculated profile fits the observed profile, but also how good the structural model is. Therefore two agreement factors are quoted for the refinement results in this thesis; χ^2, which is a profile factor and is defined in equation 2.25, and the magnetic RF-factor, which is a crystallographic factor defined by

$$R_F = 100 \frac{\sum_n \left[\left| G_{obs,n} - \sqrt{\sum_k G_{calc,k}^2} \right| \right]}{\sum_n G_{obs,n}}. \tag{2.27}$$

In the least squares minimisation technique (see for example [5]), χ^2 is minimised by solving the set of equations $\delta(\chi^2)/\delta\alpha_j = 0$ for the list of parameters, $\boldsymbol{\alpha}$ (see equation 2.25). It is a local search technique, and it is important to have good initial parameter values in order to avoid becoming stuck in false minima.

An alternative algorithm for the refinement, also available using FULLPROF, is simulated annealing (SA) [41, 58]. In SA, a 'cost function' ($E(\mathbf{\Omega})$) is optimised with respect to a list of parameters ($\mathbf{\Omega}$) in the following manner. Firstly, an initial cost function is constructed with the input list of parameters, $\mathbf{\Omega}_{old}$. With each iteration of the simulation these parameters are altered by a small amount and renamed $\mathbf{\Omega}_{new}$. The condition for accepting the new cost function is that either (a) $\mathbf{\Delta} = E(\mathbf{\Omega}_{new}) - E(\mathbf{\Omega}_{old}) < 0$ or, if $\mathbf{\Delta} > 0$, that (b) $e^{-\mathbf{\Delta}/T}$ is larger than a random number between 0 and 1. Here T is the temperature factor, which is reduced by a specified step in each iteration of the simulation. In this manner, the probability of selecting a configuration which is worse than the previous configuration reduces as the simulation progresses and the temperature 'cools'. The cost function used in FULLPROF for SA is

$$E(\mathbf{\Omega}) = \left(\sum_n \left| I_{obs,n} - S \sum_k I_{calc,k}(\mathbf{\Omega}) \right| \right) / \sum_n I_{obs,n}, \tag{2.28}$$

where $\mathbf{\Omega}$ is a list of parameters that define the Fourier components $\mathbf{S}_{\boldsymbol{\kappa} j}$ (see equation 2.17). In contrast to the least squares algorithm, the SA algorithm is a global search technique that does not easily become stuck in false minima, and is therefore a very useful technique for generating possible models of the magnetic structure.

2.3.5 Neutron inelastic scattering

The energies of thermal neutrons are close to the energies of atomic and electronic processes, allowing one to probe lattice and magnetic excitations using neutron inelastic scattering (NIS). The kinematics of NIS are based upon energy and momentum conservation. As discussed earlier, the scattering vector ($\mathbf{Q}$) is defined in terms of the incident and final wave vector of the neutrons ($\mathbf{k}_i$ and $\mathbf{k}_f$) by $\mathbf{Q} = \mathbf{k}_i - \mathbf{k}_f$ (see figure 2.7a). In the scattering process, momentum ($\hbar\mathbf{Q}$) is transferred to the system, and if the scattering process is inelastic then the neu-

tron also transfers energy ($E_i - E_f = \hbar\omega$) to the system. Applying the cosine rule to the scattering configuration of figure 2.7a gives

$$\mathbf{Q}^2 = \mathbf{k}_i^2 + \mathbf{k}_f^2 - 2|\mathbf{k}_i||\mathbf{k}_f| \cos\theta. \tag{2.29}$$

In units of energy this becomes

$$\frac{\hbar^2\mathbf{Q}^2}{2m} = E_i + E_f - 2\sqrt{E_i E_f} \cos\theta. \tag{2.30}$$

In NIS, the scattering function $S(\mathbf{Q}, \hbar\omega)$ (see equations 2.4 - 2.6) is mapped out in $(\mathbf{Q}, \omega)$-space.

Neutron spectrometers

One common experimental technique for NIS is triple axis spectrometry, in which a monochromator crystal defines the incident energy of the neutrons and an analyser crystal selects the final neutron energy [17]. However, in this work the HET and MARI direct geometry chopper spectrometers at the ISIS pulsed spallation source were used. In this technique the incident neutron energy is selected using a chopper (velocity selector), and the final energies of the neutrons are calculated from their time of flight. This is in contrast to the indirect geometry technique in which the incident beam is not monochromated but the final neutron energy is selected.

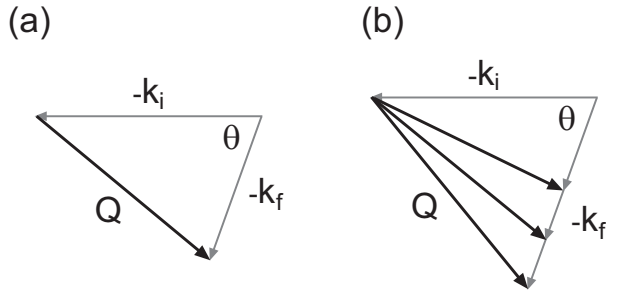

Figure 2.7: (a) Scattering triangle for neutrons with incident wave vector $\mathbf{k_i}$ and final wave vector $\mathbf{k_f}$. (b) Scattering triangle for direct geometry chopper spectrometers, for which the incident wave vector is selected and the final wave vectors are used to determine the energy and momentum transfered to the system.

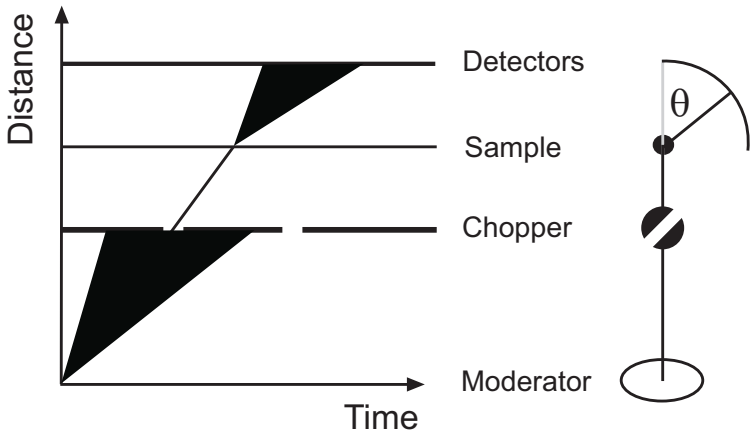

Figure 2.8: Schematic distance-time diagram for a direct geometry spectrometer. The chopper is used to select the incident energy of the neutrons and the energy and momentum transfered to the sample is determined from their time of flight to the detector.

Figure 2.7b shows the scattering triangle for direct geometry and figure 2.8 shows a schematic distance-time diagram for a direct geometry spectrometer. The neutrons leave the moderator in a short pulse at time t=0 with a wide spread of velocities (energies). A chopper, placed at a fixed distance from the moderator, only allows neutrons within a band of specified velocities (energies) to pass through to the sample. The neutrons scatter from the sample, changing direction and energy, and arrive at different times at the detector. Their final energy (and hence the energy transfer) can be calculated from their time of flight. The neutrons also transfer momentum to the sample. In direct geometry, conservation of energy ($\hbar\omega = \frac{\hbar^2}{2m}\left(|\mathbf{k}_i|^2 - |\mathbf{k}_f|^2\right)$) can be used in equation 2.30 to eliminate E_f and obtain the expression

$$\frac{\hbar^2\mathbf{Q}^2}{2m} = 2E_i - \hbar\omega - 2\cos\theta\sqrt{E_i(E_i - \hbar\omega)}. \tag{2.31}$$

This maps out the path in $(\mathbf{Q},\omega)$-space traced by a detector placed at an angle θ. Spectrometers typically have detector banks covering a wide solid angle in order to access as much of $(\mathbf{Q},\omega)$-space as possible. The energy resolution of the spectrometer depends predominantly on the width of the pulse from the moderator

(Δt_m), the opening time of the chopper (Δt_c) and the time of flight at the chopper (t_c). The uncertainty in the energy transfer ($\Delta\hbar\omega$) is given approximately by equation 2.32, where $\Delta(\hbar\omega)_m$ and $\Delta(\hbar\omega)_c$ are the moderator and chopper terms defined in equations 2.33 and 2.34 respectively [17].

$$\frac{\Delta\hbar\omega}{E_i} = \left[\left(\frac{\Delta(\hbar\omega)_m}{E_i}\right)^2 + \left(\frac{\Delta(\hbar\omega)_c}{E_i}\right)^2\right]^{1/2} \tag{2.32}$$

$$\frac{\Delta(\hbar\omega)_m}{E_i} = 2\left(\frac{\Delta t_m}{t_c}\right)\left[1 + \frac{l_3}{l_2}\left(1 - \frac{\hbar\omega}{E_i}\right)^{3/2}\right] \tag{2.33}$$

$$\frac{\Delta(\hbar\omega)_c}{E_i} = 2\left(\frac{\Delta t_c}{t_c}\right)\left[1 + \frac{l_1 + l_3}{l_2}\left(1 - \frac{\hbar\omega}{E_i}\right)^{3/2}\right] \tag{2.34}$$

l_1, l_2 and l_3 are the path lengths from the moderator to chopper, sample to detector and chopper to sample respectively. Typically the instrument resolution is optimised for a specific experiment by tuning the opening time of the chopper and the incident energy of the neutrons.

HET and MARI are very similar spectrometers in design, with the major difference between them being their detector coverage. The low angle detectors on HET cover scattering angles of 3 - 7^o and 9 - 29^o, and the high angle detector banks cover the ranges 110 - 125^o and 130 - 140^o. On the other hand, MARI has a detector bank that continuously covers the scattering angle range from 3 - 135^o, thereby mapping a much larger range of $(\mathbf{Q}, \omega)$-space in a single measurement than HET.

2.3.6 Multiple scattering and phonon subtractions

Generally in a neutron scattering experiment it is the flux of neutrons that have only been scattered once that is of interest. However, the measured flux may also contain contributions from multiply scattered neutrons. In the work of this thesis the computer program DISCUS has been used to calculate the effect of twice-scattered neutrons by employing a Monte Carlo simulation technique [36].

From the measured scattering function the simulation predicts the ratio of once-scattered to twice-scattered neutrons detected and enables the correction of the data for multiple scattering, attenuation due to re-scattering and absorption. The cross section for twice-scattered neutrons is essentially a self-convolution of the once-scattered cross section over $|\mathbf{Q}|$ and ω. In general, the multiple scattering contribution is therefore a smoothed out version of the once-scattered data.

The DISCUS program can also calculate and subtract an approximation to the phonon contribution of the measured data based on the scattering function measured at high $|\mathbf{Q}|$. After the multiple scattering contribution has been calculated and subtracted, the scattering function in the high $|\mathbf{Q}|$ region is assumed to be purely from phonon scattering, which has a $|\mathbf{Q}|^2$-dependence. On this assumption, the phonon contribution as a function of $|\mathbf{Q}|$ and $\hbar\omega$ is calculated by DISCUS, and is subtracted along with the multiple scattering contribution in order to leave a purely magnetic scattering function (given the assumption).

DISCUS corrections have been performed on some of the NIS results for $Cu_2Te_2O_5(Br_xCl_{1-x})_2$ presented in chapter 5. In these DISCUS corrections it is assumed that the scattering detected in the high angle MARI detector bank ($120^\circ < 2\theta < 135^\circ$, which corresponds to approximately 4.7 $Å^{-1} < |\mathbf{Q}| <$ 4.9 $Å^{-1}$ at 5 meV), contained only phonon and multiple scattering contributions. In order to attempt to justify this assumption, one must consider the square of the Cu^{2+} magnetic form factor. At $|\mathbf{Q}| = 3$ $Å^{-1}$ the square of the Cu^{2+} form factor is $\sim 46\%$ of its value at $|\mathbf{Q}| = 0.5$ $Å^{-1}$, and by $|\mathbf{Q}| = 5$ $Å^{-1}$ it is $\sim 14\%$. Based on this, the magnetic contribution from single ion Cu^{2+} to the overall scattering in the MARI high angle detector bank should be rather small. However, the calculation and subtraction of phonon contributions to the scattering can be a complicated matter, and it is important to note that these are only approximate corrections.

Chapter 3

Growth and Characterisation of $Cu_2Te_2O_5(Br_xCl_{1-x})_2$

3.1 Sample growth

Polycrystalline samples of $Cu_2Te_2O_5(Br_xCl_{1-x})_2$ were grown using a chemical transport reaction [37]. The starting materials CuO (Aldrich, 99.99%), $CuBr_2$ (Aldrich, 99%), $CuCl_2$ (Aldrich, 99.999%), TeO_2 (Aldrich, 99+%) were mixed in the stoichiometric molar ratio CuO : $CuBr_2$: $CuCl_2$: TeO_2 = 1 : x : $1-x$: 2. Nominal starting compositions of x = 0, 0.25, 0.5, 0.625, 0.75 and 1 were used. The powders were sealed in evacuated glass tubes and fired at 440°C (x = 1), 450°C (x = 0) or 445°C (x intermediate) for 90 hours. The samples were then reground and sintered at the same temperature several times in order to minimise any impurity phase. The products were analysed on a Hilton Brooks powder x-ray diffractometer, and the diffraction pattern of the end compounds (x = 0, 1) compared to those given in the Joint Committee on Powder Diffraction Standards (JCPDS) Powder Diffraction File (PDF) database in order to confirm that they were indeed the correct phase. Figure 3.1 shows the intensity of one of the high-intensity diffraction peaks (reflection 210) for all of the compositions.

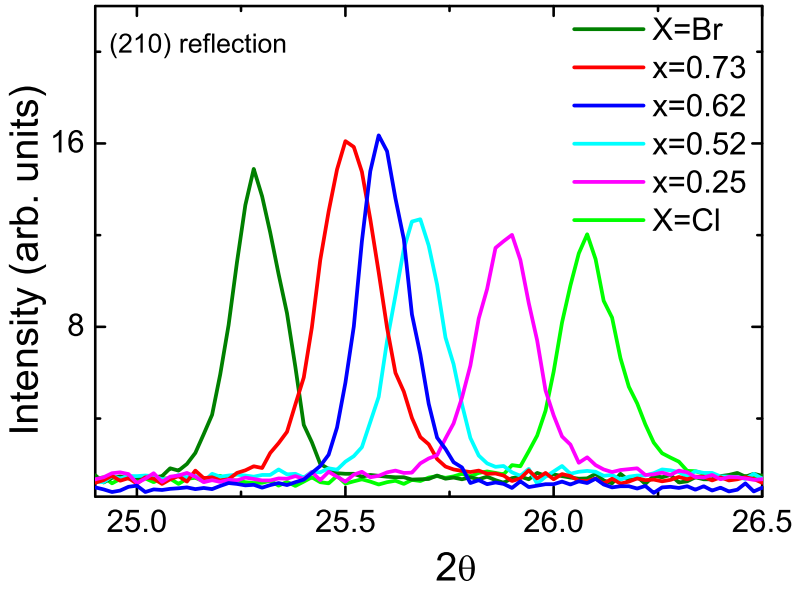

Figure 3.1: X-ray diffraction peak (210) of $Cu_2Te_2O_5(Br_xCl_{1-x})_2$, with compositions $x = 0$, 0.25, 0.52, 0.62, 0.73 and 1, focussing on a small region of 2θ.

There is no sign of split peaks or impurity peaks, indicating that the samples are of high purity and, in particular, that the mixed composition samples are single phase. The position of the peak shifts smoothly across the compositions. Using a linear interpolation of the 2θ peak value between the end X=Br and X=Cl samples (averaged over a number of peaks), the compositions of the intermediate samples have been extracted. These were very close to the starting compositions; $x = 0.25 \pm 0.02$, 0.52 ± 0.02, 0.62 ± 0.02, and 0.73 ± 0.02. The width of the diffraction peak varies little for different compositions and the peak is clearly resolved with respect to the spread over 2θ of the different compositions (the average HWHM of the peak corresponds to a range in composition of $\Delta x \sim 0.08$).

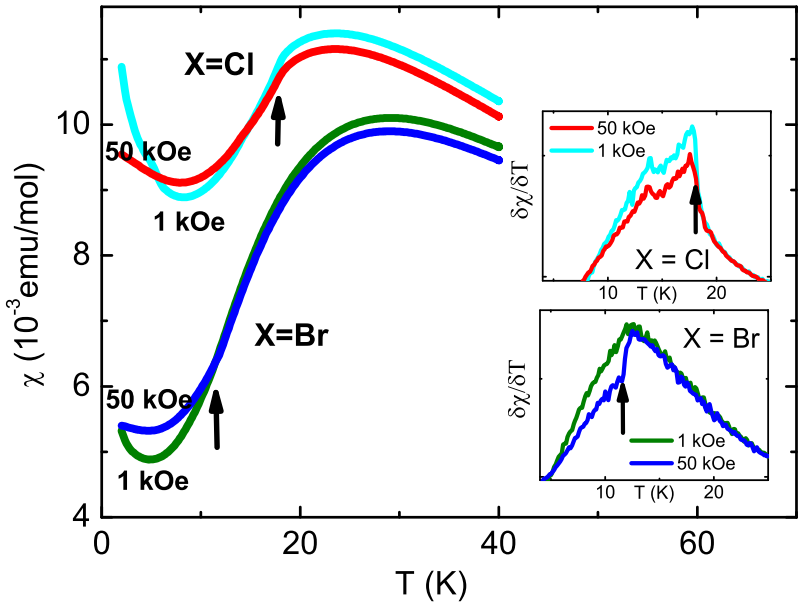

Figure 3.2: Susceptibility as a function of temperature for $Cu_2Te_2O_5Br_2$ with an applied field of 1 kOe (green) and 50 kOe (blue), and $Cu_2Te_2O_5Cl_2$ with an applied field of 1 kOe (cyan) and 50 kOe (red). The inset shows the temperature derivative of the susceptibility, $\delta\chi/\delta T$.

3.2 Magnetisation measurements

Magnetic susceptibility measurements of $Cu_2Te_2O_5(Br_xCl_{1-x})_2$, $x = 0$, 0.25, 0.52, 0.62, 0.73 and 1, were performed using a Quantum Design SQUID magnetometer. Figure 3.2 shows the susceptibility (χ) as a function of temperature (T) for $Cu_2Te_2O_5X_2$ (X=Br,Cl) in applied magnetic fields of 1 kOe (green and cyan respectively) and 50 kOe (blue and red respectively), displaying an identical temperature behaviour to that reported previously in the literature [46] (see section 1.3.3). Small impurity-related Curie tails are present at low temperatures (below $\sim$ 5 K) corresponding to 0.2% and 0.6% free Cu^{2+} impurity in the X=Br and X=Cl samples respectively. In the X=Cl sample there is a small kink in $\chi(T)$ at T_N^{Cl} =18.2

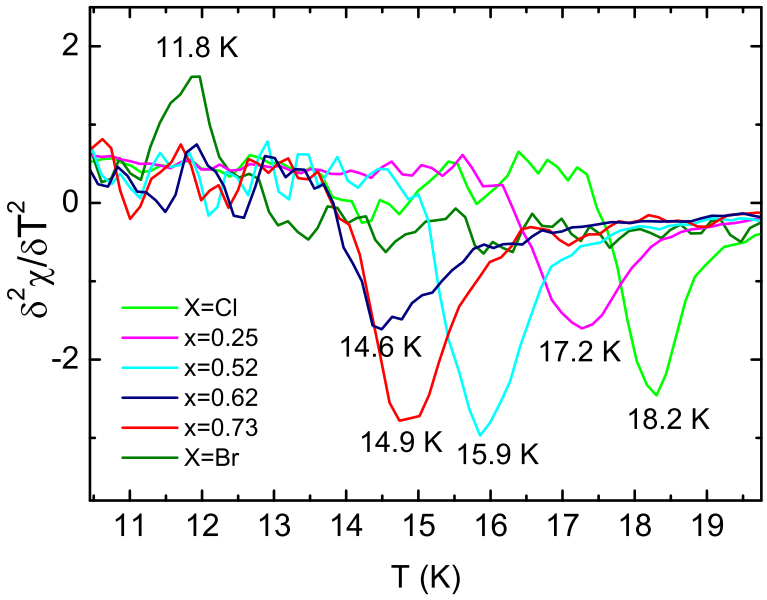

Figure 3.3: The double derivative of the susceptibility ($\delta^2\chi/\delta T^2$) is plotted as a function of temperature for the compositions x = 0, 0.25, 0.52, 0.62, 0.73 and 1. The magnetic transition temperatures are clearly visible as maxima or minima in $\delta^2\chi/\delta T^2$, and increase linearly with decreasing x.

K, but for X=Br there is no discernible feature in the raw data at T_N^{Br}= 11.4 K. However, in the temperature derivative of the data, $\delta\chi/\delta T$, small step-like features in the data are observed for both samples as indicated in figure 3.2. For X=Br, this feature is clearer in the high field (50 kOe) data, whilst in the X=Cl sample it is more prominent in the lower field (1 kOe) data. These features become clear peaks in the double derivative ($\delta^2\chi/\delta T^2$) of the data, as shown in figure 3.3. Also included in figure 3.3 is data collected for the mixed composition samples, $Cu_2Te_2O_5(Br_xCl_{1-x})_2$ with x = 0.25, 0.52, 0.62, and 0.73. The data shown here was taken in an applied field of 50 kOe for the x = 0.62 and 1 samples, and in an applied field of 1kOe for the x= 0, 0.25, 0.52 and 0.73 samples.

From these measurements the transition temperatures of the intermediate

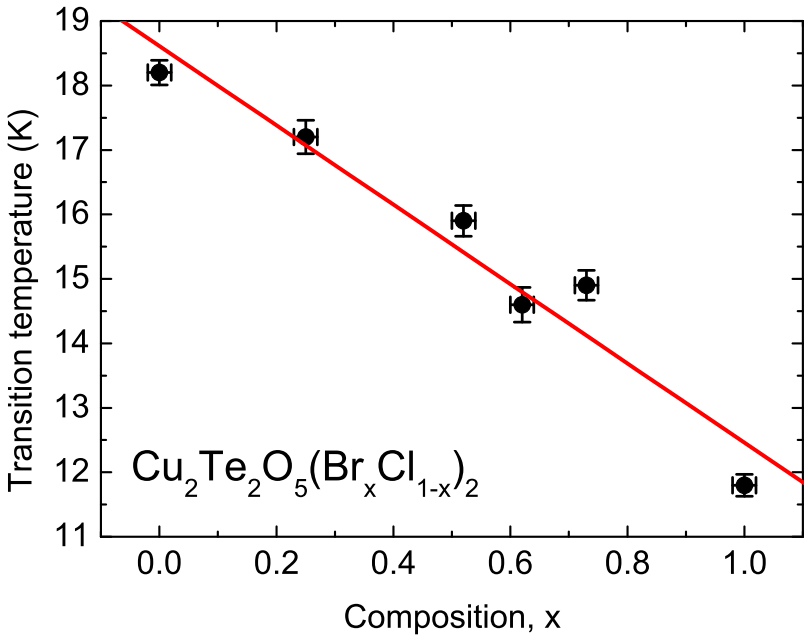

Figure 3.4: The transition temperatures for compositions $x = 0$, 0.25, 0.52, 0.62, 0.73 and 1 are plotted as a function of x.

composition samples can be extracted, and the transition temperature as a function of composition is shown in figure 3.4. The transition temperatures increase in a reasonably linear fashion on doping of Cl for Br (i.e. decreasing x), in agreement with reference [45]. Also of interest in this work, is the value of the temperature at the maxima in $\chi(T)$ (T_{max}) for each sample, as shown in figure 3.5. The maximum in $\chi(T)$ is at significantly larger temperatures for the end compounds (X=Br,Cl) than for the mixed compositions. This may be due to disorder, which could have the effect of reducing the overall coupling strength of the magnetic interactions. With increasing x, T_{max} decreases from the pure X=Cl sample to a minimum at $x = 0.25$, before increasing steadily to $x = 0.73$, followed by a large increase of ~ 8 K to the pure X=Br compound.

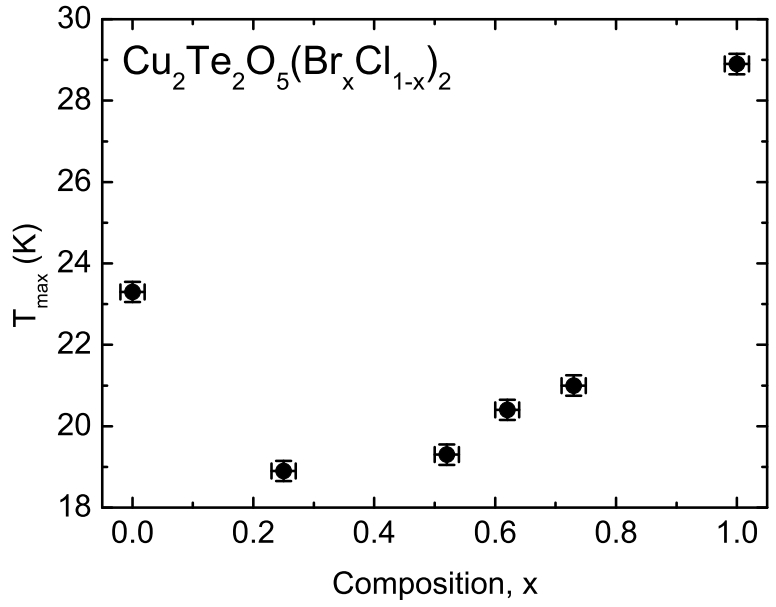

Figure 3.5: The temperature at the maximum in $\chi(T)$ (T_{max}) is plotted as a function of composition, x.

3.3 Heat capacity measurements

Heat capacity measurements of $Cu_2Te_2O_5(Br_xCl_{1-x})_2$, x = 0, 0.25, 0.52, 0.73 and 1 were performed using a Quantum Design Physical Properties Measurement System (PPMS). Figure 3.6 shows heat capacity ($C_p(T)$) data as a function of temperature for compositions x = 0, 0.52, and 1, both in zero applied field, and in an applied field of 90 kOe. Clear features in the data are observed in the end compounds X=Br and X=Cl at the respective transition temperatures T_N^{Br}= 11.4 K and T_N^{Cl}= 18.2 K. The X=Cl compound shows a sizeable anomaly, the magnitude and transition temperature of which reduces by a small amount in an applied field, whilst the X=Br compound has a much smaller anomaly, which shifts to higher temperatures and increases in magnitude in an applied field. This agrees well with previously published data [46]. It is interesting to note

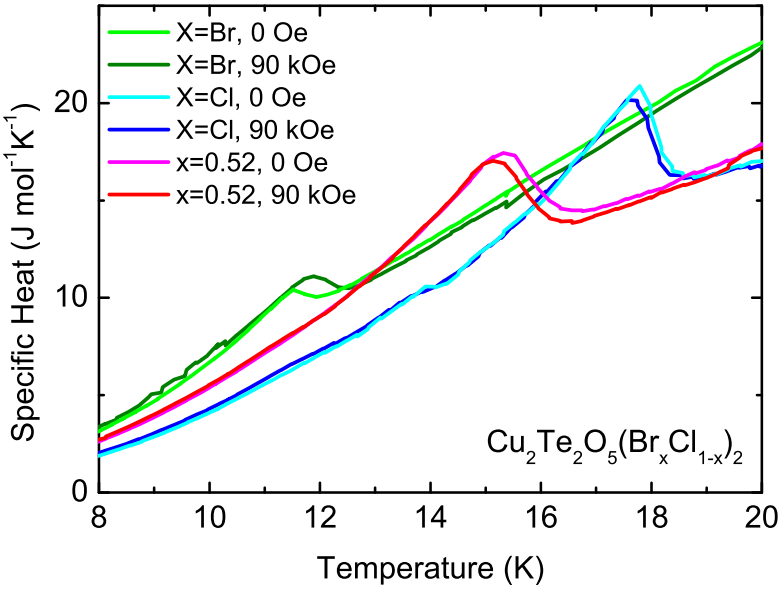

Figure 3.6: Heat capacity as a function of temperature for $Cu_2Te_2O_5(Br_xCl_{1-x})_2$, with compositions $x = 0$, 0.52 and 1, taken in 0 and 90 kOe.

the observed field-dependence of the anomaly in the $x = 0.52$ sample, which appears to follow the character of the Cl sample rather than the Br sample. This is more clearly illustrated in figures 3.7 and 3.8, from which it can be seen that all of the mixed compositions follow a similar field-dependence to the chloride. Figure 3.7 shows the transition temperature as a function of composition in 0 and 90 kOe, where the transition temperature has been taken as the peak of the anomaly (which, whilst perhaps not precisely the true transition temperature, is a consistent measure between the different compositions). The zero-field anomaly is observed to shift smoothly in temperature with increasing Cl substitution for Br, in agreement with the transition temperatures extracted from susceptibility data (see above), and with previously published data [27]. The inset of figure 3.7 shows the difference between the zero field and 90 kOe transition temperature (ΔT_N) divided by the zero field transition temperature, i.e. $\Delta T_N/T_N$, as a function of

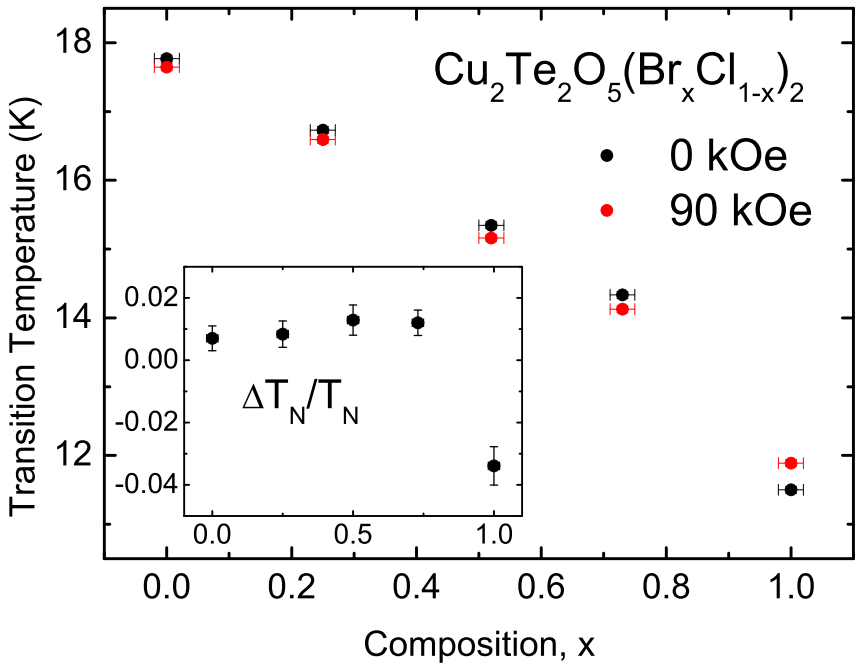

Figure 3.7: The transition temperatures of the $Cu_2Te_2O_5(Br_xCl_{1-x})_2$ both in 0 (black) and 90 kOe (red), are plotted as a function of composition, x. The inset shows $\Delta T_N/T_N$ (that is, the difference between the zero field and 90 kOe transition temperature divided by the zero field transition temperature) as a function of composition.

composition. Whilst the value of $\Delta T_N/T_N$ is small and positive for $x = 0$, 0.25, 0.52, and 0.73, for X=Br it becomes negative and significantly larger ($\sim$ 4 times larger) in magnitude. Figure 3.8 shows the height of the anomaly as a function of composition, both in 0 and 90 kOe. The inset shows the difference between the zero field and 90 kOe anomaly height (Δh) divided by the zero field anomaly height, i.e. $\Delta h/h$, as a function of composition. Again, the compositions $x = 0$, 0.25, 0.52 and 0.73 show a small, positive value for $\Delta h/h$, whilst the X=Br compound has a larger, negative value.

When comparing the heat capacity data of the different compositions it is also interesting to observe the differing amounts of entropy associated with the transitions. The size of the anomalies indicates that with decreasing x, increasing

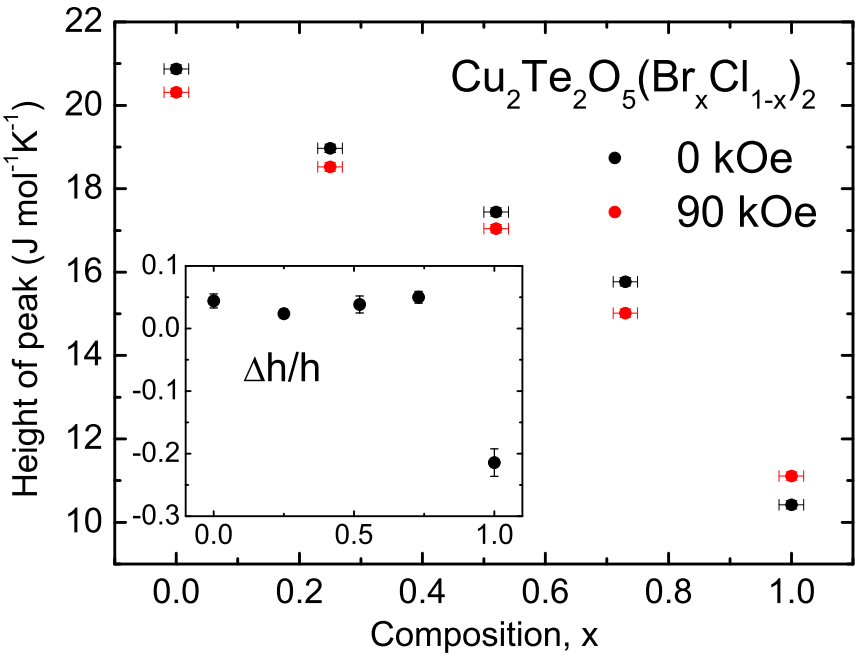

Figure 3.8: The height of the anomaly for each sample in 0 (black) and 90 kOe (red) is plotted as a function of the composition. The inset shows $\Delta h/h$ (that is, the difference between the zero field and 90 kOe anomaly height divided by the zero field anomaly height) as a function of composition.

amounts of entropy are associated with the transition. The total entropy (S) up to a temperature T can be extracted from heat capacity data using the expression [26],

$$S(T) = \int_0^T \frac{C}{T} dT. \tag{3.1}$$

Using equation 3.1, the total entropy up to the respective transition temperatures of the different compositions was calculated and the results are displayed in table 3.1. From equation 1.6, the magnetic entropy is predicted to be $2 \times R \ln 2 \sim$ 11.5 J mol^{-1} K^{-1}). Therefore, even if it is assumed that **all** of the entropy below the transition temperatures is magnetic, in none of the samples will all of the magnetic entropy have been recovered by T_N. Table 3.1 lists the percentage of magnetic entropy that has been recovered by T_N under the assumption that all of the entropy below T_N is magnetic. In fact, some of the entropy below T_N must

x	Total S up to T_N	% of total magnetic entropy
1	3.3 J mol^{-1} K^{-1}	28.6 %
0.73	6.3 J mol^{-1} K^{-1}	54.6 %
0.52	6.8 J mol^{-1} K^{-1}	59.0 %
0.25	7.0 J mol^{-1} K^{-1}	62.3 %
0	7.5 J mol^{-1} K^{-1}	65.0 %

Table 3.1: The total entropy (S) up to the transition temperature (T_N) is listed for the compositions $x = 0$, 0.25, 0.52, 0.73 and 1. The right hand column gives this as a percentage of the total expected magnetic entropy ($2 \times R \ln 2 \sim 11.5$ J mol^{-1} K^{-1}).

be associated with the phonons (the contribution of the phonons has been ignored thus far), and hence this is a lower limit on the amount of 'missing' magnetic entropy up to T_N. For the X=Br compound in particular there must be a large amount of magnetic entropy above the transition temperature, as only 29% at most has been recovered by T_N. Indeed, above the transition temperatures the heat capacity of the X=Br compound remains significantly higher than for the other compositions, by $\sim$ 25% at 20 K. The magnetic entropy above T_N may be associated with low dimensional and/or short range correlations.

Chapter 4

Magnetic Structure of $Cu_2Te_2O_5(Br_xCl_{1-x})_2$

4.1 Introduction and experimental details

The spin-tetrahedral compounds $Cu_2Te_2O_5X_2$ (X=Br,Cl) have recently attracted attention as a result of their unusual magnetic behaviour, details of which are discussed in chapter 1. The present chapter is concerned with the nature of the magnetic ordering in $Cu_2Te_2O_5X_2$ (X=Br,Cl), and how this changes with doping of Cl for Br in mixed composition samples $Cu_2Te_2O_5(Br_xCl_{1-x})_2$.

The magnetic ordering was initially investigated by neutron diffraction measurements on polycrystalline $Cu_2Te_2O_5(Br_xCl_{1-x})_2$, x = 0, 0.25, 0.52, 0.73, 1 (section 4.2). These measurements were performed on the high flux D20 diffractometer at the ILL, Grenoble (see section 2.3.3 for details). Details of the sample growth and characterisation are presented in chapter 3. Subsequently, a single crystal neutron diffraction study of $Cu_2Te_2O_5Br_2$ has been performed in order to refine the magnetic structure (section 4.3). This measurement was performed on the four-circle D10 diffractometer at the ILL, Grenoble (see section 2.3.3 for details). The high quality single crystal sample of $Cu_2Te_2O_5Br_2$, with dimen-

sions 1.5 mm x 1.5 mm x 4 mm, was provided by O. Zaharko and grown by H. Berger [80] using a halogen vapour transport technique, with $TeBr_4$ and Br_2 as transport agents. In light of this single crystal magnetic structure refinement and recent developments in the field [80, 81], the D20 polycrystalline work is briefly revisited in section 4.4. Finally, the work presented in this chapter is summarised in section 4.5.

4.2 Neutron diffraction study of polycrystalline $Cu_2Te_2O_5(Br_xCl_{1-x})_2$

4.2.1 Results

Anomalies have previously been observed in the temperature dependence of magnetization [37, 46], heat capacity [46, 27] and thermal conductivity measurements [61, 69] at T_N^{Cl} =18.2 K and T_N^{Br}= 11.4 K for $Cu_2Te_2O_5Cl_2$ and $Cu_2Te_2O_5Br_2$ respectively, which have been associated with the development of some form of magnetic ordering. Studies of mixed composition samples (presented in chapter 3) show that upon doping of Cl for Br, the anomaly associated with the magnetic transition shifts linearly to higher temperatures. In order to investigate this further, neutron diffraction measurements of polycrystalline samples of $Cu_2Te_2O_5(Br_xCl_{1-x})_2$, x = 0, 0.25, 0.52, 0.73 and 1 have been performed on the D20 diffractometer at the ILL with a neutron wavelength of λ = 2.4 Å. The scattering angle coverage of the detector was $10^\circ < 2\theta < 150^\circ$, corresponding to a range in $|\mathbf{Q}|$-space of 0.4 Å^{-1} $< |\mathbf{Q}| <$ 5 Å^{-1}.

Firstly, the nuclear scattering profile of each of the samples was examined by measuring the diffraction pattern in the paramagnetic phase above T_N (at T = 25 K). The lattice parameters and atomic positions, as well as a number of instrumental parameters, were refined using the Rietveld method from the

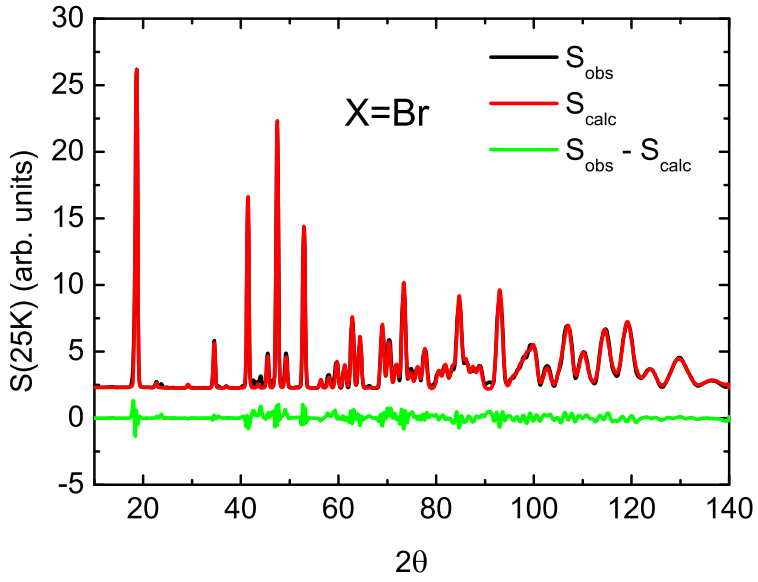

Figure 4.1: Nuclear scattering profile of $Cu_2Te_2O_5Br_2$, taken at T = 25 K. The x-axis is 2θ and the y-axis is the observed scattering intensity (black), calculated scattering intensity (red) and the difference between the observed and calculated scattering intensity (green).

nuclear profiles using a least squares algorithm in the program FULLPROF (see section 2.3.4 for details on the refinement procedure and FULLPROF). Figure 4.1 shows the scattering profile of $Cu_2Te_2O_5Br_2$ in the paramagnetic state (black), with the calculated nuclear scattering profile determined from the Rietveld refinement also displayed (red). The difference between the observed and calculated scattering profiles is plotted as a function of 2θ in green. Whilst there are small deviations of the calculated profile from the observed profile, the overall fit is good, with an agreement factor for the nuclear structure of RF = 4.0 % (see section 2.3.4 for a definition of the RF-factor). In a similar manner, the nuclear structures were refined for all of the compositions. The lattice parameters of each composition (x = 0, 0.25, 0.52, 0.73 and 1) are listed in table 4.1 along with the agreement RF-factors of the Rietveld refinement. The lattice parameters are seen to increase smoothly with increasing x from $Cu_2Te_2O_5Cl_2$ to $Cu_2Te_2O_5Br_2$ in agreement with

x	a, b	c	RF-factor
1	7.7774(5)	6.3690(5)	3.99 %
0.73	7.7448(7)	6.3721(6)	5.38 %
0.52	7.6951(5)	6.3576(5)	4.88 %
0.25	7.6386(8)	6.3435(5)	5.56 %
0	7.5913(7)	6.3181(5)	3.26 %

Table 4.1: The Rietveld refined lattice parameters for $Cu_2Te_2O_5(Br_xCl_{1-x})_2$, $x =$ 0, 0.25, 0.52, 0.73 and 1 at T=25 K, and the agreement RF-factor of the refinements.

reference [45].

The scattering profiles of each composition were also measured at T = 2 K, which is well below the transition temperature in all of the samples (11.8 K $< T_N^x <$ 18.2 K). In the low temperature phase additional magnetic peaks appear. The high temperature paramagnetic scattering profile has been subtracted from the scattering profile in the magnetic phase to give a difference plot that corresponds to purely magnetic scattering. The difference plot of $Cu_2Te_2O_5Br_2$ in the region 0.5 Å^{-1} $< |\mathbf{Q}| <$ 2 Å^{-1} is shown in figure 4.2. Due to the thermal expansion of the sample the lattice parameters are slightly different at T = 2 and 25 K, and hence there is a small shift of the nuclear Bragg peaks with temperature. The subtraction of the high temperature phase from the low temperature phase therefore does not completely remove the nuclear contribution, but instead leaves a characteristic 'negative-positive' intensity profile at the positions of the nuclear Bragg peaks in the higher temperature phase, as indicated by red lines in figure 4.2. This is in contrast to the magnetic peaks, which have a Gaussian-like profile.

Figure 4.3 is a difference plot as a function of $|\mathbf{Q}|$ for all of the compositions, showing the two lowest order magnetic peaks. Peaks are observed at $|\mathbf{Q}|$= 0.63 and 0.77 Å^{-1} for X=Br, and $|\mathbf{Q}|$= 0.66 and 0.74 Å^{-1} for X=Cl respectively, with the peak positions shifting linearly between these values with x. These magnetic peaks cannot be indexed using a simple model in which the magnetic structure is commensurate with the nuclear unit cell, implying that the magnetic structure in all

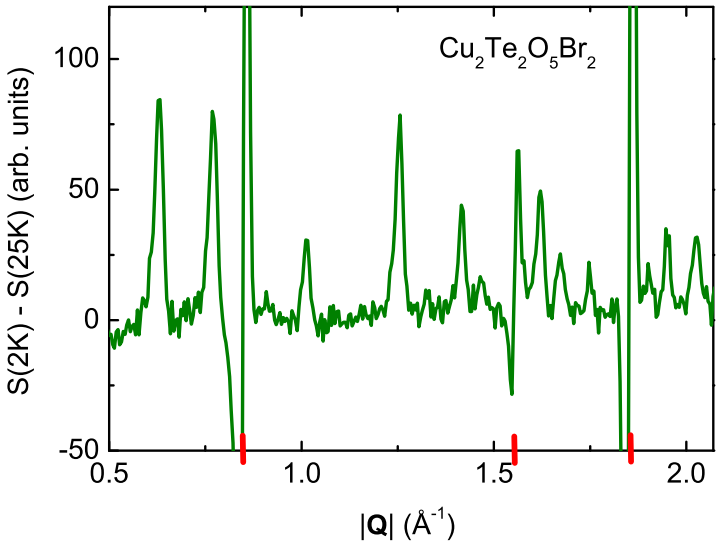

Figure 4.2: Magnetic neutron diffraction scattering profile of $Cu_2Te_2O_5Br_2$. This is a difference plot, showing the high temperature scattering intensity (T = 25 K) subtracted from the low temperature scattering intensity (T = 2 K) as a function of momentum transfer. The red lines indicate the positions of strong nuclear Bragg peaks.

compositions is incommensurate with the nuclear lattice. The propagation vector ($\boldsymbol{\kappa}$) that defines the modulation of the spin arrangement has been determined for all of the compositions by fitting the positions of the magnetic peaks with respect to the nuclear peaks, and these are listed in table 4.2. The modulation vector is found to shift linearly with decreasing x, from $\boldsymbol{\kappa}_{Br}$ = [0.170, 0.350, 1/2] for the bromide to $\boldsymbol{\kappa}_{Cl}$ = [0.150, 0.420, 1/2] for the chloride. The z-component of the modulation vector is 1/2, which is commensurate with the nuclear structure and means that along the z-axis the spins are rotated by 180 degrees with respect to the corresponding spin in the neighbouring unit cell.

4.2.2 Discussion

Previous macroscopic measurements have indicated that $Cu_2Te_2O_5Br_2$ and $Cu_2Te_2O_5Cl_2$ have rather different magnetic behaviours. Firstly, the anomalies observed at T_N

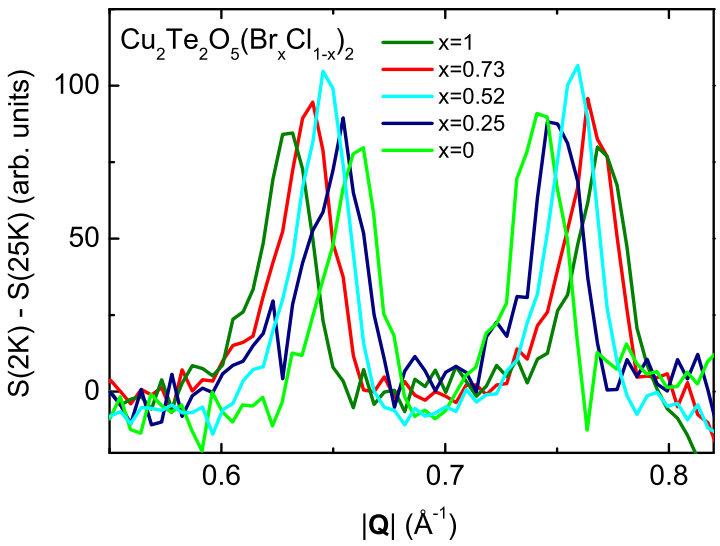

Figure 4.3: Magnetic neutron diffraction scattering profile of $Cu_2Te_2O_5(Br_xCl_{1-x})_2$ for $x = 0$, 0.25, 0.52, 0.73 and 1. This is a difference plot, showing the high temperature scattering intensity (T = 25 K) subtracted from the low temperature scattering intensity (T = 2 K) as a function of momentum transfer.

x	$\boldsymbol{\kappa}$
1	[0.170, 0.350, 1/2]
0.73	[0.168, 0.373, 1/2]
0.52	[0.161, 0.391, 1/2]
0.25	[0.155, 0.406, 1/2]
0	[0.150, 0.420, 1/2]

Table 4.2: The propagation vector of the magnetic structure, $\boldsymbol{\kappa}$, listed as a function of x for $Cu_2Te_2O_5(Br_xCl_{1-x})_2$.

in zero-field temperature dependent susceptibility and heat capacity measurements are far more pronounced in the case of X=Cl than X=Br [46]. Furthermore, the applied magnetic field dependence of the anomaly observed in heat capacity measurements acts in the opposite sense for $Cu_2Te_2O_5Br_2$ than for each of the other compositions (see section 3.3). The anomaly in the heat capacity of compositions $x = 0$, 0.25, 0.52 and 0.73 shows a small reduction in magnitude and decrease in transition temperature in an applied magnetic field, which corresponds to the type of behaviour expected from antiferromagnetic ordering. However, the anomaly in the heat capacity of the bromide shows a field-dependence opposite to that expected from simple antiferromagnetic order, with the magnitude and temperature of the anomaly increasing with applied magnetic field. These results, along with further differences observed in the thermal conductivity [61, 69] of the end compounds, led many to believe that the underlying magnetic structure of the chloride and bromide would be significantly different. It is therefore somewhat surprising that the neutron diffraction results presented in section 4.2.1 reveal that both end compounds have a similar incommensurate magnetic structure, and that doping of Cl for Br leads to a linear shift of the modulation vector.

As discussed in section 2.3.4, the spin moment $\mathbf{m}_{nj}$ of the jth atom in the nth unit cell can be expressed for an incommensurate magnetic structure as

$$\mathbf{m}_{nj} = \mathbf{A}_j \cos 2\pi(\boldsymbol{\kappa} \cdot \mathbf{R}_n + \psi_j) + \mathbf{B}_j \sin 2\pi(\boldsymbol{\kappa} \cdot \mathbf{R}_n + \psi_j). \qquad (4.1)$$

where $\mathbf{A_j}$ and $\mathbf{B_j}$ are orthogonal vectors that define the plane of rotation of the jth atom and ψ_j defines its phase. Figure 4.4 illustrates the geometry and angles that define $\mathbf{A_j}$, $\mathbf{B_j}$ and ψ_j in a particular case, known as the generalised helix model, in which $|\mathbf{A_j}| = |\mathbf{B_j}|$, and hence the jth spin has a constant moment magnitude in all cells. In the generalised helix model each atom can be defined by four parameters; $|\mathbf{A_j}| = |\mathbf{B_j}|$, ψ_j and the two polar angles θ_{B_j} and ϕ_{A_j}, because $\mathbf{A_j}$ can always be chosen such that it lies in the xy plane ($\theta_{A_j} = 90°$), and $\phi_{B_j} = \phi_{A_j} + 90$ due to orthogonality.

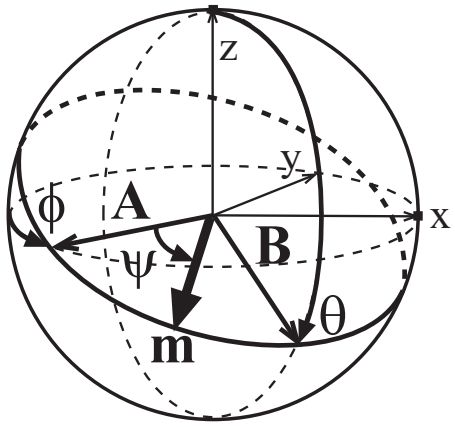

Figure 4.4: Two orthogonal vectors $\mathbf{A_j}$ and $\mathbf{B_j}$ define the plane of rotation of the jth magnetic moments, and ψ_j defines its phase. $\mathbf{A_j}$ and $\mathbf{B_j}$ are, in turn, expressed by the polar coordinates θ and ϕ as illustrated here.

In $Cu_2Te_2O_5(Br_xCl_{1-x})_2$, the moments of the four Cu^{2+} ions in the unit cell are independent, that is, they are not related by the symmetry of the magnetic phase. In the most general case this would mean that a total of 28 independent parameters are required to describe the magnetic structure. In the generalised helix model (in which the moments propagate within a circular envelope), one would require 16 parameters. This would reduce to 12 parameters under the additional assumption that all of the Cu^{2+} ions have the same moment (and by also defining $\psi_j = 0$ for one of the ions in the zeroth cell without loss of generality). For the polycrystalline neutron diffraction data presented above, only $\sim$ 12 magnetic peaks are resolved above the background due to a combination of the small magnetic moment (spin-1/2) and the decreasing intensity of the magnetic peaks with increasing $|\mathbf{Q}|$ (due to the magnetic form factor). Even with the assumptions of the generalised helix model with equal moments on all four Cu^{2+} ions, this still leaves as many parameters to be refined as there are magnetic peaks. In this sense, the polycrystalline data does not provide enough information to enable the refinement of what appears to be a rather complicated magnetic structure.

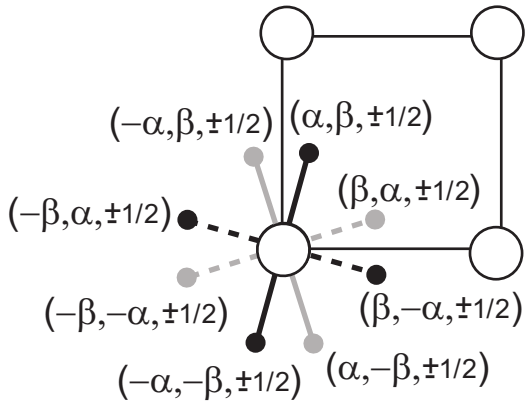

Figure 4.5: hk0 and hk1/2 projections of reciprocal space with the lowest 2θ satellites of the 000 reflection marked. The four black spots are the four arms that make up the star of the wave vector $\boldsymbol{\kappa}$ =(α,β,1/2) in the space group P$\overline{4}$. A second star, of the wave vector $\boldsymbol{\kappa'}$ =($-\alpha$,β,1/2) is illustrated by the four grey spots. The dotted lines indicate the configuration domains that are 90° rotated. This figure has been adapted from reference [80].

Recently, independent neutron diffraction results have been published by Zaharko et al. [80]. Their results reveal that both the bromide and chloride compounds have an incommensurate magnetic structure modulated by the vectors $\boldsymbol{\kappa}_{Br} \approx$ [0.158, 0.354, 1/2] and $\boldsymbol{\kappa}_{Cl} \approx$ [0.150, 0.422, 1/2] respectively, which is in close agreement with the results presented above. However, the authors also present a single crystal neutron diffraction investigation of $Cu_2Te_2O_5Cl_2$ that provides considerable information about the magnetic structure. Firstly, the investigation reveals the presence of multiple magnetic domains, which are described with the help of figure 4.5 (adapted from reference [80]). The four black spots in figure 4.5 are the four arms that make up the star of the wave vector $\boldsymbol{\kappa}$ =(α,β,1/2) in the space group P$\overline{4}$. They originate from two configuration domains in which the wave vector rotates by 90 degrees (black dotted line in figure 4.5). However, their investigation also revealed the presence of a second set of 4 reflections from the star of a different wave vector, $\boldsymbol{\kappa'}$ =($-\alpha$,β,1/2) (grey spots in figure 4.5), which must give rise to a separate magnetic structure as the two wave vectors are not related by the symmetry of P$\overline{4}$. It is worth noting that the presence of reflections

arising from both wave vectors, and indeed from both configuration domains, was reported to be sample dependent. The authors refine the $\boldsymbol{\kappa}_{Cl}$ magnetic structure from 59 reflections (please note that in reference [80] the $\boldsymbol{\kappa}_{Cl}$ and $\boldsymbol{\kappa}'_{Cl}$ propagation vectors were incorrectly assigned due to a confusion between a^* and b^*, therefore the true structure reported in that work was that of the propagation vector $\boldsymbol{\kappa}_{Cl}$ =[0.15, 0.422, 1/2] [79]). They propose a model in which the four Cu^{2+} ions of each tetrahedron split into two pairs, Cu1-Cu2 and Cu3-Cu4, where the positions of the Cu atoms are Cu1(x,y,z), Cu2($1-x$,$1-y$,z), Cu3(y,$1-x$,$-z$) and Cu4($1-y$,x,$-z$), with $x \sim 0.730$, $y \sim 0.452$ and $z \sim 0.158$. The angle between the spins of each pair remains constant as the spin pairs rotate on independent helices with propagation vector $\boldsymbol{\kappa}$. The cant angle is γ_{12} =38° between Cu1 and Cu2, and γ_{34} =111° between Cu3 and Cu4. The refined moment (equal by assumption for all Cu^{2+} ions) is $0.67\mu_B$/ion. Figure 1.10 in section 1.3 shows this proposed magnetic structure over several unit cells. Finally, it is important to note that this model did not fit at all well the data set corresponding to the other wave vector, $\boldsymbol{\kappa}'_{Cl}$, and the authors therefore believe that the two magnetic structures must be different in terms of the spin arrangements. Not enough reflections of the $\boldsymbol{\kappa}'_{Cl}$ domain were collected to enable this magnetic structure to be determined.

As discussed earlier, the magnetic structure in these compounds is too complicated to be refined solely from the polycrystalline data presented in section 4.2.1. However, as evidenced by the work of Zaharko et al. discussed above, a single crystal neutron scattering investigation can provide more information and allow for a refinement of the magnetic structure. To this end, a single crystal neutron diffraction investigation of $Cu_2Te_2O_5Br_2$ has been performed and is the subject of the following section. In section 4.4 the polycrystalline data presented above is re-evaluated with respect to the conclusions drawn from the single crystal study.

4.3 Neutron diffraction study of single crystal $Cu_2Te_2O_5Br_2$

The single crystal neutron diffraction study of $Cu_2Te_2O_5Br_2$ was performed on D10 with an incident neutron wavelength of $\lambda = 2.36$ Å, and a sample of dimensions 4 x 1 x 1 mm^3 (provided by O. Zaharko and H. Berger [80]). Two magnetic reflections at the lowest 2θ value were observed in this crystal, corresponding to a single configuration domain with wave vector $\boldsymbol{\kappa}'_{Br}$ = [-0.172, 0.356, 1/2]. Referring to figure 4.5, these correspond to the black spots linked by a solid line. In contrast to the data presented for the chloride in reference [80], no peaks were observed at the 90 degree rotated positions in the bromide crystal studied here. Furthermore, no peaks arising from a second independent wave vector ($\boldsymbol{\kappa}_{Br}$ = [0.172, 0.356, 1/2]) were observed, as was the case in the chloride studied by Zaharko et al. A set of integrated intensities containing 44 magnetic reflections arising from the propagation vector $\boldsymbol{\kappa}'_{Br}$ = [-0.172, 0.356, 1/2] were collected at T = 2 K. In addition, 23 nuclear reflections were collected. The integrated intensities of the magnetic and nuclear reflections were normalised to the monitor count and corrected for the Lorentz geometric factor. Possible models for the magnetic structure of $Cu_2Te_2O_5Br_2$ were refined using FULLPROF, with a combination of the simulated annealing and least squares algorithms (see section 2.3.4 for details). The scale factor was fixed to that determined from the nuclear structure refinement of the 23 nuclear reflections.

4.3.1 Magnetic structure refinement

The magnetic structure refinement of $Cu_2Te_2O_5Br_2$ has been made under the assumption that the structure is a generalised helix with all of the Cu^{2+} moments equal. This model has 12 free parameters to be refined, which are listed in table 4.3 and can be visulised with the help of figure 4.4.

Initially, the specific case of collinear spin arrangements was investigated.

On a tetrahedron with a dominant antiferromagnetic exchange, one can have either dimers or tetramers, both of which form singlet states (see section 1.3.4). Both the dimer and tetramer collinear spin arrangements gave a very poor fit to the data, with agreement factors of RF$\sim$ 63.5 % and 52.1 % respectively. Secondly, in order to test whether or not the structure is the same as that refined for $Cu_2Te_2O_5Cl_2$ by Zaharko et al. [80], this model has been fixed and fitted to the bromide data allowing only the moment to be refined. A moment of 0.324(4)μ_B/ion was refined, compared to 0.67μ_B/ion [80] in the chloride. However, the agreement RF-factor of the refinement is RF $=$ 72.4 %, which is not a good fit and indicates that the structures of the two compounds are different.

In order to generate other possible models for the magnetic structure of $Cu_2Te_2O_5Br_2$, a simulated annealing algorithm in FULLPROF was utilised, allowing all 12 parameters of the generalised helix model to be refined from arbitrary initial starting values. The simulated annealing technique is a global search technique ideal for this type of problem, as discussed in section 2.3.4. Table 4.3 lists the results of the generalised helix refinement with all parameters unconstrained (referred to as model I), and figure 4.6 shows the resulting magnetic structure over several unit cells. Three key points can be extracted from this general refinement;

1. The Cu1 and Cu2 moments appear to share the same plane of rotation and are approximately parallel.

2. The Cu3 and Cu4 moments appear to share the same plane of rotation and have a canting angle of approximately 120 deg.

3. All four Cu^{2+} moments have planes of rotation that are tilted only slightly from the xz plane.

From these observations one can go on to constrain the generalised helix model further in order to develop a consistent model. In the following text, several models will be described for which the parameters are listed in tables 4.3 and 4.4. For

		Model I	Model II	Model III	Model IV
μ_B/Cu^{2+}		0.392(3)	0.404(4)	0.406(4)	0.399(4)
Cu1	ϕ_A	5(8)	-9(5)	-8(5)	-10(5)
	θ_B	16(7)	7(6)	12(4)	10(3)
	ψ_1	0	0	0	0
Cu2	ϕ_A	-7(8)	$=$Cu1ϕ_A	$=$Cu1ϕ_A	$=$Cu1ϕ_A
	θ_B	-4(6)	$=$Cu1θ_B	$=$Cu1θ_B	$=$Cu1θ_B
	ψ_2	21(3)	$=\psi_1$	$=\psi_1$	18(3)
Cu3	ϕ_A	12(8)	33(7)	30(4)	18(4)
	θ_B	-7(6)	-16(5)	-11(4)	-5(4)
	ψ_3	255(3)	248(3)	248(3)	254(3)
Cu4	ϕ_A	-9(7)	25(8)	$=$Cu3ϕ_A	$=$Cu3ϕ_A
	θ_B	11(7)	3(8)	$=$Cu3θ_B	$=$Cu3θ_B
	ψ_4	130(2)	125(2)	125(2)	129(2)
RF-factor		14.6 %	17.5 %	17.5 %	14.8 %
χ^2		3.34	4.58	4.50	3.37

Table 4.3: Refined parameters of magnetic structure models I - IV based on the notation of the generalised helix model. The imposed constraints for different models are marked and the RF-factor and χ^2 of the refinement are also listed.

each of the models a simulated annealing algorithm was used to locate the correct minimum and subsequently the resulting model was improved by refining with a least squares algorithm.

Firstly, in order to investigate point 1 above, the moments on Cu1 and Cu2 can be constrained to be parallel whilst all other parameters are left free to be refined. This is achieved by constraining the plane of rotation for both Cu1 and Cu2, as well as their phases, to be equal (Cu1ϕ_A=Cu2ϕ_A; Cu1θ_B=Cu2θ_B; $\psi_1 = \psi_2$). This model is referred to as model II. Under this constraint, the Cu1 and Cu2 moments remain approximately in the xz plane, consistent with point 3. However, whilst Cu3 and Cu4 remain at a constant angle of approximately 120 degrees (point 2), they begin to rotate in a plane that is substantially tilted to the xz plane (in contrast with point 3). Moreover, the agreement RF-factor worsens (increases) when this constraint is introduced. Model III in table 4.3 constrains the moments of Cu3 and Cu4 to cant, that is, rotate in the same plane

		Model V	Model VI	Model VII	Model VIII
μ_B/Cu^{2+}		0.398(3)	0.395(3)	0.394(3)	0.395(3)
Cu1	ϕ_A	0	8(2)	6(3)	-8(5)
	θ_B	0	0	5(2)	0
	ψ_1	0	0	0	0
Cu2	ϕ_A	0	=Cu1ϕ_A	=Cu1ϕ_A	=Cu1ϕ_A
	θ_B	0	0	=Cu1θ_B	0
	ψ_2	28(2)	22(2)	24(3)	18(3)
Cu3	ϕ_A	0	=Cu1ϕ_A	=Cu1ϕ_A	15(3)
	θ_B	0	0	=Cu1θ_B	0
	ψ_3	257(3)	257(3)	255(3)	255(2)
Cu4	ϕ_A	0	=Cu1ϕ_A	=Cu1ϕ_A	=Cu3ϕ_A
	θ_B	0	0	=Cu1θ_B	0
	ψ_4	137(2)	135(2)	133(2)	130(2)
RF-factor		13.7 %	14.0 %	13.7 %	14.8 %
χ^2		3.77	3.56	3.56	3.33

Table 4.4: Refined parameters of magnetic structure models VI - VIII based on the notation of the generalised helix model. The imposed constraints for different models are marked and the RF-factor and χ^2 of the refinement are also listed.

(Cu3ϕ_A=Cu4ϕ_A; Cu3θ_B=Cu4θ_B) with a fixed angle between them defined by their phases. This confirms that the moments on Cu3 and Cu4 cant at an angle of γ_{34} ∼120°. In model IV the constraint on Cu1 and Cu2 being parallel is released, and they are constrained instead to cant at a refinable angle. Model IV therefore consists of two pairs of canting moments, similar to the chloride model refined by Zaharko et al. [80], but with the angles defining the planes of rotation free to refine. For this model the agreement RF-factor improves and the cant angles are refined to be γ_{12} =18° and γ_{34} =125° for the Cu1-Cu2 and Cu3-Cu4 pairs respectively, in line with points 1 and 2. Again, all of the moments rotate in planes that are fairly close to the xz plane (point 3). Model IV is illustrated in figure 4.7, and can be seen to be very similar to model I despite the additional constraints.

In order to investigate point 3, all of the Cu^{2+} moments have been constrained to the xz-plane in model V (ϕ_A=0 and θ_B=0 for all moments), see table 4.4. For this model all of the moments are constrained to rotate in the same

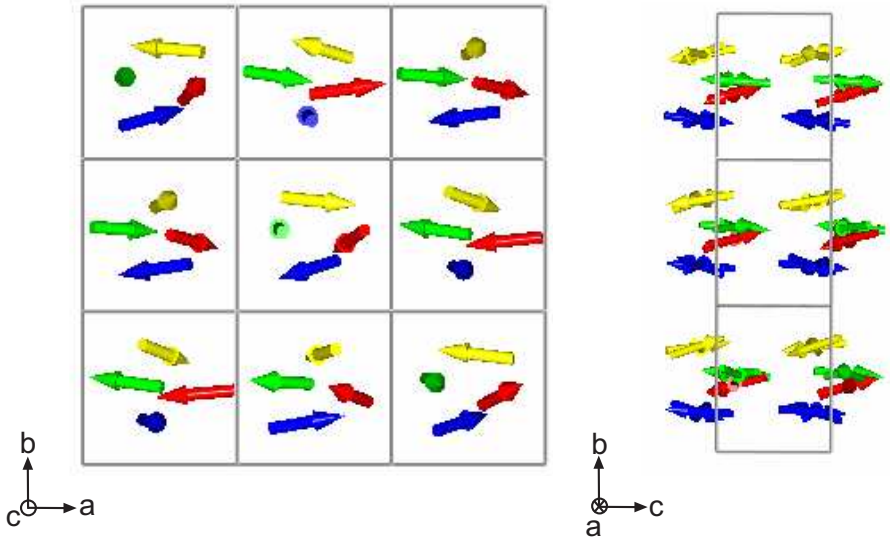

Figure 4.6: Magnetic structure model I. The Cu1 moment is red, Cu2 green, Cu3 blue and Cu4 yellow. All 12 parameters of the generalised helix model were free to be refined.

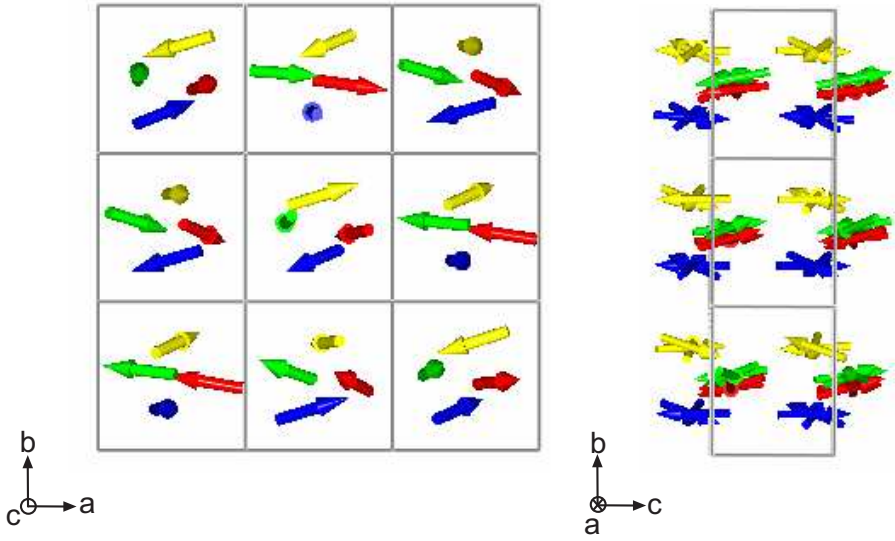

Figure 4.7: Magnetic structure model IV. The Cu1 moment is red, Cu2 green, Cu3 blue and Cu4 yellow. The pairs Cu1-Cu2 and Cu3-Cu4 were constrained to rotate in the same plane with fixed angles, whose refined values are γ_{12} =18° and γ_{34} =125°.

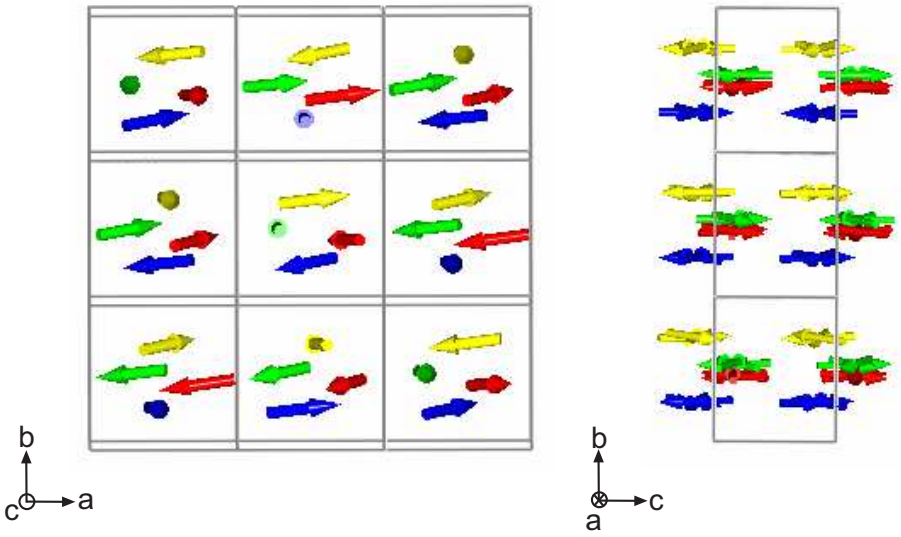

Figure 4.8: Magnetic structure model VI. The Cu1 moment is red, Cu2 green, Cu3 blue and Cu4 yellow. All four Cu moments are constrained to rotate in the same plane, which contains the z-axis. The four moments are constrained to have equal values of ϕ_A, which is refined.

plane, and hence they all cant at fixed angles to each other. The respective angles are γ_{12} =28°, γ_{43} =120°, γ_{31} =103°, γ_{14} =137°, γ_{32} =131° and γ_{24} =109°. In particular, the canting angles of Cu1-Cu2 and Cu3-Cu4 remain close to those refined in the canting pair model (model IV) and in line with points 1 and 2. Moreover, the agreement RF-factor remains low.

Starting from model V, one can begin to release some of the constraints to test how sensitive the refinement is to the parameters. For example, one can maintain the constraint that all of the moments rotate in the same plane, but allow this plane to tilt away from the xz-plane. Model VI releases the constraint on ϕ_A=0, but maintains the constraint that ϕ_A is equal for all Cu^{2+} moments. The agreement RF-factor of the refinement changes little, and the plane of rotation is found to tilt at an angle $\phi_A = 8°$ (see figure 4.8). In Model VII the constraint on θ_B=0 is also released, but θ_B remains constrained to be equal for all of the moments. The refined structure only tilts slightly away from the xz-plane ($\phi_A = 6$ and $\theta_B = 5$), and the agreement RF-factor remains low. Finally, model VIII is

similar to model VI, but with the two pairs independent through release of the constraint Cu3θ_B = Cu1θ_B. The planes of rotation of the two pairs of Cu^{2+} ions are refined to be at an angle of $\sim 20^\circ$ to each other, and there is a slight increase in the RF-factor.

4.3.2 Discussion

The refinement of the $Cu_2Te_2O_5Br_2$ magnetic structure was very stable. The models described above (in tables 4.3 and 4.4) had a range of constraints and initial starting values, but all of them converged to a very similar magnetic structure. Most significantly, the simulated annealing refinement in which all 12 of the generalised helix parameters were free to refine, gave a magnetic structure that was little altered by adding further constraints. The refinement agreement RF-factors of all of the models (excluding models II and III in which the moments of Cu1 and Cu2 were incorrectly assigned to be parallel) are within 1.1% of each other. There is also very little difference in χ^2 between the different models, which is a measure of the overall goodness of fit for the profile parameters as well as the structural parameters (see section 2.3.4). There is therefore little to distinguish between these models and it is difficult to assign one in particular as 'correct'. However, the common features of all of the models are clear. Firstly, the spins pair up such that the helices of the Cu1 and Cu2 moments rotate in the same plane with a canting angle of $\gamma_{12} \sim 20^\circ$. Secondly, the Cu3 and Cu4 moments rotate in the same plane with a canting angle of $\gamma_{34} \sim 120^\circ$. Finally, all four Cu^{2+} moments rotate in planes that are close to the xz-plane. From this data alone, further details of the magnetic structure cannot be determined due to the relative insensitivity of the refinement to additional constraints such as those in models IV - VIII above. For example, it cannot be concluded whether or not all four of the Cu^{2+} moments rotate in helices that share a common plane, as described in models V, VI and VII. Neither can it be concluded whether or not this plane is

confined to the xz-plane, or is slightly tilted to the xz-plane. However, very recent spherical neutron polarimetric measurements and unpolarised integrated intensity measurements of the $\boldsymbol{\kappa_{Cl}}'$ =[-0.15, 0.422, 1/2] magnetic structure of $Cu_2Te_2O_5Cl_2$ by Zaharko et al. [79] may possibly enable one of these models to be singled out. These measurements suggest that the refined magnetic structure associated with the $\boldsymbol{\kappa_{Cl}}'$ =[-0.15, 0.422, 1/2] propagation vector may be rather different from that of the $\boldsymbol{\kappa}_{Cl}$ =[0.15, 0.422, 1/2] structure previously reported [80]. The structure of the propagation vector $\boldsymbol{\kappa}'_{Cl}$ =[-0.15, 0.422, 1/2] was found to be like that of model VI, but with slightly differing canting angles (γ_{12} ∼12° and γ_{34} ∼70°) and a refined moment of 0.88(1) μ_B/ion. This suggests that the $Cu_2Te_2O_5Cl_2$ $\boldsymbol{\kappa}'_{Cl}$ and $Cu_2Te_2O_5Br_2$ $\boldsymbol{\kappa}'_{Br}$ magnetic structures may be very similar, and that perhaps model VI is best able to describe them both.

In discussing the physical significance of the $Cu_2Te_2O_5Br_2$ structure refinement, it is important to firstly recognise that there are a number of competing interactions in this system. There may be geometrical frustration of the spins within a tetrahedron, significant competition between intra- and inter-tetrahedral couplings, and also the possibility of a Dzyaloshinski-Moriya anisotropy interaction of significant strength. Section 1.3 discusses the possible exchange paths, and their proposed relative strengths on the basis of both theoretical and experimental studies. In particular, the work of Whangbo et al. [78] highlights the importance of super-superexchange inter-tetrahedral exchange interactions mediated by the Br atoms, J_a and J_b (see figure 1.9).

In the presence of geometrical frustration, a highly degenerate ground state is not uncommon. For the chloride measurements reported by Zaharko et al., the presence of two different magnetic structures (defined by $\boldsymbol{\kappa}_{Cl}$ and $\boldsymbol{\kappa}'_{Cl}$) indicates that at least two ground states with either equal or close energies exist [80]. However, it is unclear whether the presence of these two wave vectors arises from degeneracy of the ground state, or from localised differences in the stoichiometry.

In any case, the fact that the presence of both structures is sample dependent indicates the high sensitivity of the ground state stability. The bromide sample studied in this work does not show two magnetic structures as only the reflections from one propagation vector, $\boldsymbol{\kappa}'_{Br}$, are observed. Whether or not a different magnetic structure associated with a second propagation vector would be present in different bromide crystals remains to be seen. A wider study is required in order to determine the degeneracy of the ground state, and how this may differ between the two compounds.

Despite the similarity of their magnetic structures, a further significant difference between the chloride and the bromide are their refined moments. The reduced Cu^{2+} moment of $\sim$ 0.40 μ_B/ion in the bromide compared with a proposed moment of 0.88 μ_B/ion in the chloride [79], indicates that there may be important differences between their underlying exchange interactions, for example greater frustration on the tetrahedra in the bromide. Also of interest is the total sum of the moment on a tetrahedral unit, which depends upon the model adopted for the magnetic structure. Common to all of the models put forward in section 4.3 are the canting pairs Cu1-Cu2 and Cu3-Cu4 with canting angles of $\sim 20^\circ$ and $\sim 120^\circ$ degrees respectively. The vector sum of the moments on each pair give total pair moments of magnitude $\sim$ 0.79 μ_B/pair and $\sim$ 0.40 μ_B/pair for the Cu1-Cu2 and Cu3-Cu4 pairs respectively. The magnitude of the pair moments are the same on any tetrahedron in the structure due to the fact that within a pair the moments rotate in the same plane with a fixed cant angle. However, the magnitude of the overall tetrahedral moment would vary between different unit cells unless both pairs shared the same plane of rotation, as is the case in models V, VI and VII. For these models, the magnitude of the total magnetic moment of a Cu^{2+} tetrahedron (that is, the magnitude of the vector sum of all four moments) is $\sim 0.39\mu_B$/tetrahedron. In these models, it is more appropriate to consider the moments as forming a 'tetramer' rather than pairs. In terms of the underlying

exchange interactions, this may indicate that the intra-tetrahedral interaction J_1 is dominant or is at least of comparable strength to J_2. In contrast, the magnetic structures which consist of two pairs (Cu1-Cu2 and Cu3-Cu4) that do not both rotate in the same plane (for example models III, IV and VIII), imply that the J_2 interaction is dominant over the J_1 interaction.

Yet the fact that there is long range order requires that there is also inter-tetrahedral coupling of some description. As discussed in reference [81] for the case of $Cu_2Te_2O_5Cl_2$, there is a link between the wave vector $\boldsymbol{\kappa}'_{Cl}$ =[-0.15, 0.422, $1/2$] and the J_b coupling. In fact, it is the vector [-0.15, 0.58, 0], which is related to $\boldsymbol{\kappa}'_{Cl}$ by a lattice translation, that lies orthogonal to a set of planes, of which one passes through the Cu2-Cu4 ions whose exchange is mediated by the J_b coupling. The same correspondence is approximately true also for $Cu_2Te_2O_5Br_2$, suggesting that perhaps the exchange interaction J_b plays a dominant role in establishing the magnetic order. This exchange interaction involves super-superexchange via two Br atoms. In fact, for a magnetic structure in which the inter-tetrahedral coupling is significant relative to the intra-tetrahedral coupling, it is perhaps more instructive to think of the system in terms of interacting square planar units as displayed in figure 1.9, rather than in terms of the interacting tetrahedra. In this case the units consist of Cu^{2+} ions that interact predominantly via exchange interactions J_a and J_b, rather than J_1 and J_2 as is the case for the tetrahedral units. In particular, consider the canted pair magnetic structures, for example models III, IV and VIII. Here, the pairs Cu1-Cu2 and Cu3-Cu4 could equally have been described as pairs interacting via J_a in a square planar unit, instead of by pairs interacting via J_2 within a tetrahedron. Similarly, the magnetic structures consisting of 'tetramers' (models V, VI and VII), could equally be thought of as tetramers interacting via J_b on a square planar unit, as tetramers interacting via J_1 on a tetrahedron. In this sense, it is difficult to be definite on the relative strength of the intra- and inter- tetrahedral coupling from these results.

4.4 Neutron diffraction study of polycrystalline $Cu_2Te_2O_5(Br_xCl_{1-x})_2$ (revisited)

In section 4.2.1 neutron diffraction data were presented that revealed the magnetic structure of $Cu_2Te_2O_5(Br_xCl_{1-x})_2$ to be incommensurate with the underlying nuclear lattice and the magnetic propagation vector to increase linearly with decreasing x, from $\boldsymbol{\kappa}_{Br} = [0.170, 0.350, 1/2]$ for the bromide to $\boldsymbol{\kappa}_{Cl} = [0.150, 0.420, 1/2]$ for the chloride. However, the magnetic structure could not be conclusively refined from this data due to the limited number of magnetic peaks observable in these polycrystalline measurements, along with the large number of parameters involved in the refinement of a complicated incommensurate structure such as this. In section 4.3 the results of a single crystal neutron diffraction study of $Cu_2Te_2O_5Br_2$ were presented and a number of possible models of the magnetic structure proposed based on refinements of the data. In this section the proposed single crystal determined models are applied to the $Cu_2Te_2O_5Br_2$ polycrystalline data. Subsequently, the nature of the progression of the magnetic structure with composition x will be investigated.

Table 4.5 lists the refined magnetic moment determined from six models whose other parameters are all fixed to those refined in the single crystal case (see tables 4.3 and 4.3). The models give a consistent value of the Cu^{2+} moment of $\sim 0.48\ \mu_B$/ion, and there is very little variance in the χ^2 or agreement RF-factors of the refinements. This compares to a consistent moment of $\sim 0.40\ \mu_B$/ion refined with precisely the same models in the single crystal case. This small discrepancy between the moment refined in the single crystal and polycrystalline cases will be re-addressed below.

Figures 4.9 and 4.10 show the observed and calculated scattering profiles of model I (generalised helix) and model V (moments confined to the xz-plane) respectively for $Cu_2Te_2O_5Br_2$ polycrystalline data. These represent the two most

Model	μ_B/Cu^{2+} ion	RF-factor	χ^2
I	0.472(6)	22.2 %	5.03
IV	0.482(6)	22.3 %	4.79
V	0.479(6)	23.9 %	5.11
VI	0.478(6)	23.6 %	5.19
VII	0.476(6)	23.4 %	5.13
VIII	0.481(6)	22.8 %	4.94

Table 4.5: The refined moments of the polycrystalline $Cu_2Te_2O_5Br_2$ data, based on six different model magnetic structures determined by the single crystal refinements of section 4.3.1

extreme cases in which either all of the parameters were free to be refined in the single crystal case (model I), or most parameters were constrained and only the phases and moment free to be refined in the single crystal case (model V). Despite this, the calculated scattering profiles of these models, based only on refinement of the moment, are extremely similar in both cases. All of the models listed in table 4.5 have a refined scattering profile lying between these models. Several points about the fit of these models to the observed scattering profiles can be noted. Firstly, both models predict the ratio of the two lowest $|\mathbf{Q}|$ peaks incorrectly. Secondly, the three highest $|\mathbf{Q}|$ peaks in the observed data have a significantly higher intensity than calculated by either model. This reflects possible differences between the overall magnetic structure in the polycrystalline and single crystal cases, which may possibly arise due to domains. Whilst only a single magnetic structure was measured in the single crystal case, it is possible that a number of different magnetic structures are present in the polycrystalline sample, which give rise to different intensities of the diffraction peaks. As discussed in section 4.3.2, there is geometrical frustration as well as competition between different inter-tetrahedral exchange interactions in this system, which can result in a number of states lying close in energy to each other. Even if the ground state is not strictly degenerate it can be highly sensitive to slight imperfections or inhomogeneities in the stoichiometry. It is possible that a polycrystalline sample

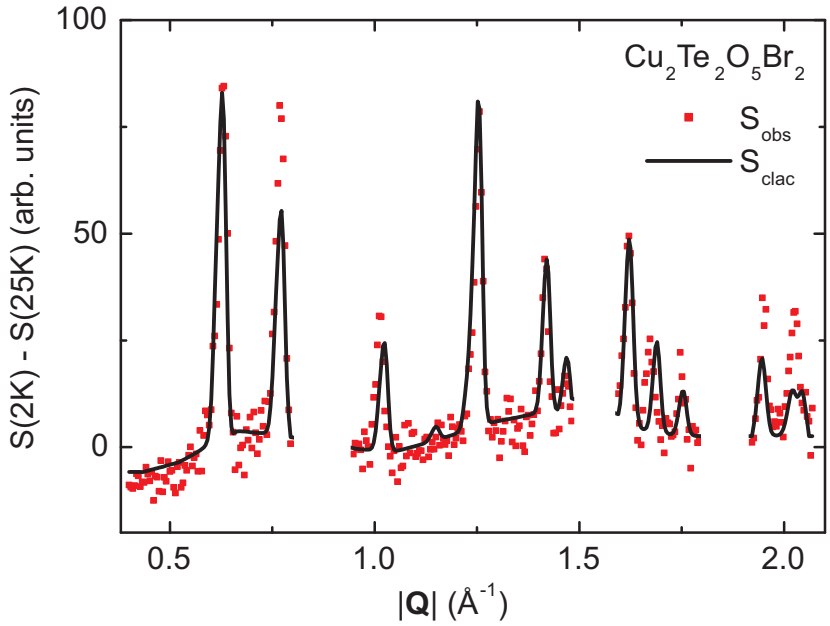

Figure 4.9: Magnetic scattering profile of polycrystalline $Cu_2Te_2O_5Br_2$. The calculated scattering profile of magnetic structure model I (determined by the single crystal refinement) is marked in black.

may therefore contain a number of domains that correspond to slightly different magnetic structures. This would also affect the overall magnetic moment refined by assuming a single domain, and could be the reason for the discrepancy observed between the polycrystalline and single crystal moment refinements.

The models determined by the single crystal diffraction study of $Cu_2Te_2O_5Br_2$ may also be used to investigate the development of the magnetic structure with doping of Cl for Br. Firstly, the parameters of model VI were fixed to those refined for single crystal $Cu_2Te_2O_5Br_2$ (see table 4.4), and the Cu^{2+} moments in the mixed composition samples were refined from the polycrystalline scattering profiles of $Cu_2Te_2O_5(Br_xCl_{1-x})_2$, $x = 0$, 0.25, 0.52 and 0.73. Table 4.6 lists the results of the refinements along with the χ^2 and agreement RF-factors. Also displayed in table 4.6 are the magnetic moments obtained by fixing the magnetic structure to that proposed for the chloride $\boldsymbol{\kappa}_{Cl}$ structure by Zaharko et al. [80] and allowing the moment to be refined. Surprisingly, the bromide model gives a much better fit to

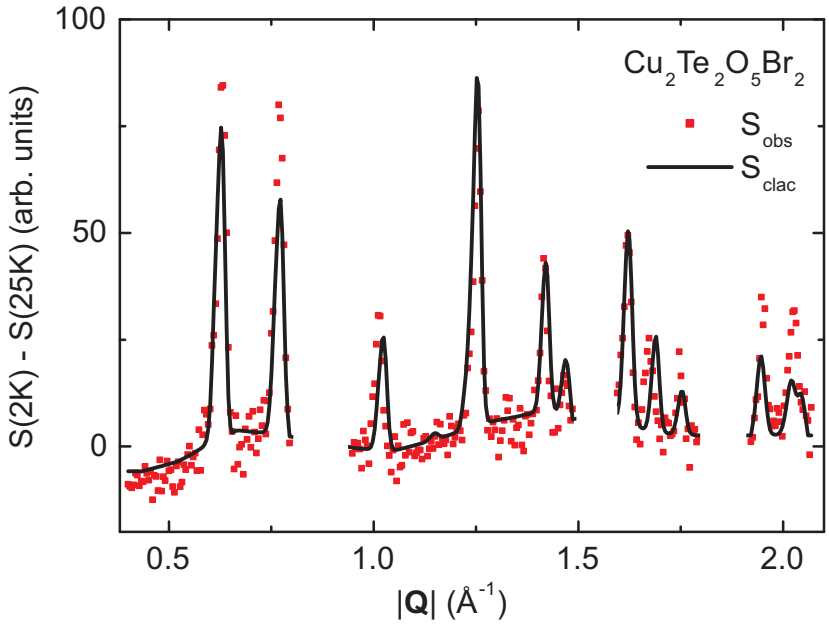

Figure 4.10: Magnetic scattering profile of polycrystalline $Cu_2Te_2O_5Br_2$. The calculated scattering profile of magnetic structure model V (determined by the single crystal refinement) is marked in black.

the data than the $\boldsymbol{\kappa}_{Cl}$ chloride model of Zaharko et al., even for the polycrystalline $Cu_2Te_2O_5Cl_2$ data. Figures 4.11 and 4.12 show the calculated and observed scattering profiles of $Cu_2Te_2O_5Cl_2$ for the chloride Zaharko et al. $\boldsymbol{\kappa}_{Cl}$ model and the bromide model VI respectively. It is clear that the bromide model fits the data far better (the agreement RF-factors are 23.9 % and 50.5 % respectively). However, as discussed in section 4.3.2, recent measurements by Zaharko et al. [79] reveal that the $\boldsymbol{\kappa}'_{Cl}$ structure of $Cu_2Te_2O_5Cl_2$ is rather different from the $\boldsymbol{\kappa}_{Cl}$ structure, and is in fact very similar to the magnetic structure of model VI proposed here for the bromide. This would suggest that the predominant domain present in the polycrystalline sample of $Cu_2Te_2O_5Cl_2$ is that corresponding to the $\boldsymbol{\kappa}'_{Cl}$ structure. The small discrepancies may be due to the fact that there is a small contribution also from the magnetic domain corresponding to propagation vector $\boldsymbol{\kappa}_{Cl}$. For example, the peaks occuring at $|\mathbf{Q}| \sim 0.95$ Å^{-1} and $|\mathbf{Q}| \sim 1.2$ Å^{-1} have more relative intensity in the chloride $\boldsymbol{\kappa}_{Cl}$ model, whereas they are underestimated in

x	Model	μ_B/Cu^{2+} ion	RF-factor	χ^2
0	Model VI	1.03(1)	23.9 %	8.1
	Cl Model	0.85(2)	50.5 %	34.0
0.25	Model VI	0.65(1)	31.2 %	1.85
	Cl Model	0.53(1)	54.5 %	3.90
0.52	Model VI	0.668(5)	14.5 %	6.74
	Cl Model	0.55(1)	57.1 %	38.4
0.73	Model VI	0.580(8)	20.9 %	5.64
	Cl Model	0.48(1)	53.2 %	13.6
1	Model VI	0.478(6)	23.6 %	5.19
	Cl Model	0.407(9)	52.6 %	12.8

Table 4.6: The refined Cu^{2+} moment of the polycrystalline data for $Cu_2Te_2O_5(Br_xCl_{1-x})_2$, $x = 0$, 0.25, 0.52, 0.73 and 1 for two different models; Model VI determined for the single crystal bromide data in section 4.3.1, and 'Cl Model', which is the model determined by Zaharko et al. for the single crystal $\boldsymbol{\kappa}_{Cl}$ structure of the chloride [80].

the bromide model. However, the intensity of the lowest $|\mathbf{Q}|$ peak is calculated to be greater than that of the second lowest $|\mathbf{Q}|$ peak in the proposed magnetic structures of both domains, whereas the opposite is observed in the data. Therefore no combination of contributions from the two proposed structures can give rise to the observed scattering profile. Indeed, attempts to fit both of these structures together to the data result in almost all of the scattering being attributed to bromide model VI. Finally, it is worth noting that for model VI the refined Cu^{2+} moment is close to 1 μ_B/ion as may be expected from a free spin-1/2 moment.

As in the case of the chloride, a much better fit to the doped polycrystalline data is obtained from the bromide model VI than the chloride model proposed by Zaharko et al. for the $\boldsymbol{\kappa}_{Cl}$ structure. Figures 4.13, 4.14 and 4.15 show the observed scattering profiles of samples x= 0.25, 0.52 and 0.73 respectively, along with the calculated profile based on model VI with only the moment refined. Generally model VI fits the doped polycrystalline data fairly well although again there are discrepancies, most notably in the ratio of the two lowest-$|\mathbf{Q}|$ peaks. However, this is consistent across the whole range of x, including the end compounds. The

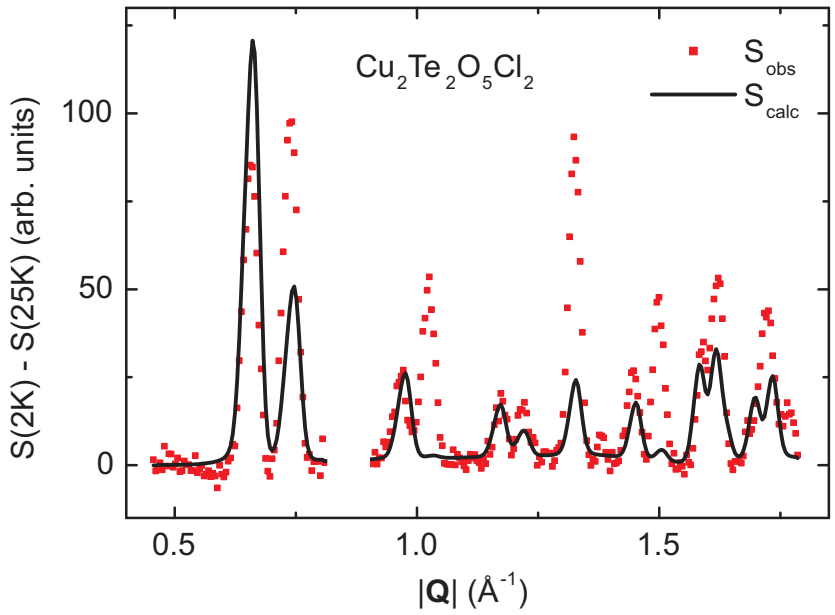

Figure 4.11: Magnetic scattering profile of polycrystalline $Cu_2Te_2O_5Cl_2$. The calculated scattering profile (black) is the magnetic structure determined by Zaharko et al. for the $\boldsymbol{\kappa}_{Cl}$ structure of single crystal $Cu_2Te_2O_5Cl_2$ [80].

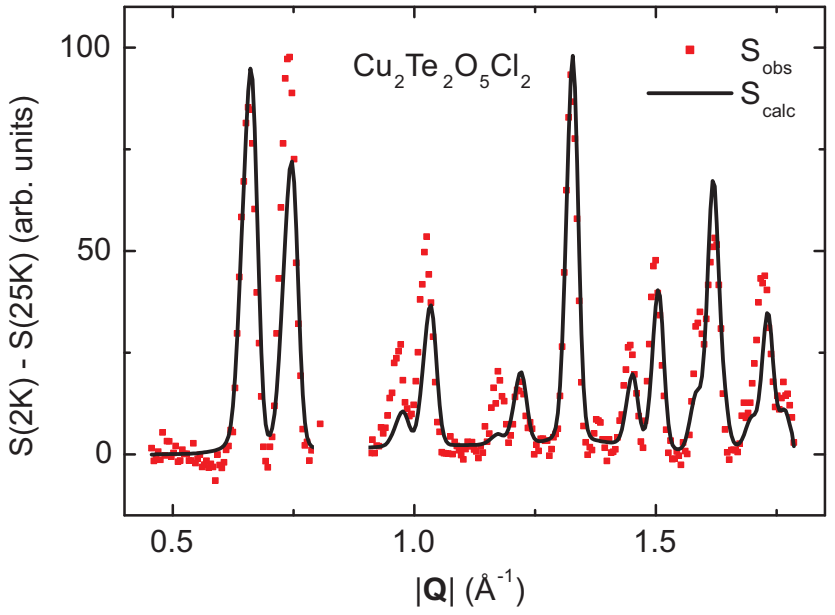

Figure 4.12: Magnetic scattering profile of polycrystalline $Cu_2Te_2O_5Cl_2$. The calculated scattering profile (black) is the magnetic structure model VI determined by the single crystal refinement of $Cu_2Te_2O_5Br_2$ in section 4.3.1.

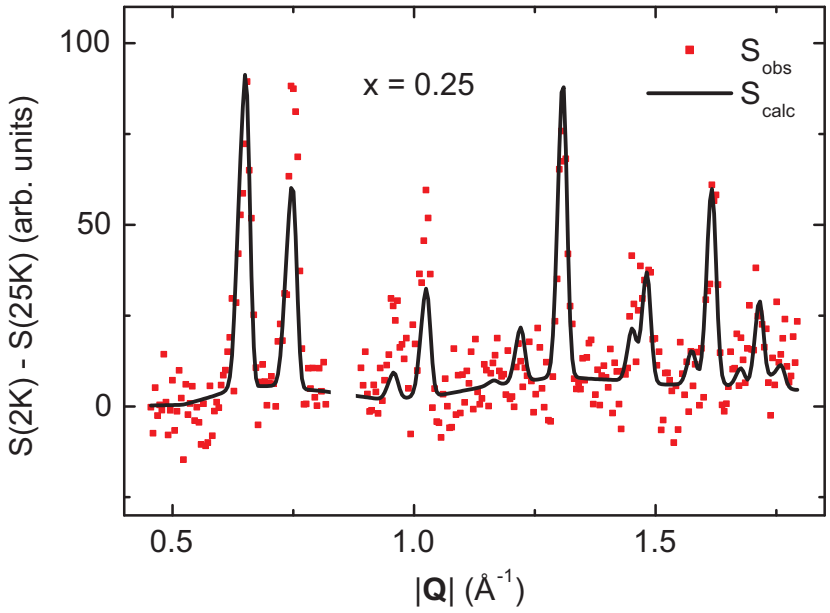

Figure 4.13: Magnetic scattering profile of polycrystalline $Cu_2Te_2O_5(Br_xCl_{1-x})_2$, $x = 0.25$. The calculated scattering profile (black) is the magnetic structure model VI determined by the single crystal refinement of $Cu_2Te_2O_5Br_2$ in section 4.3.1.

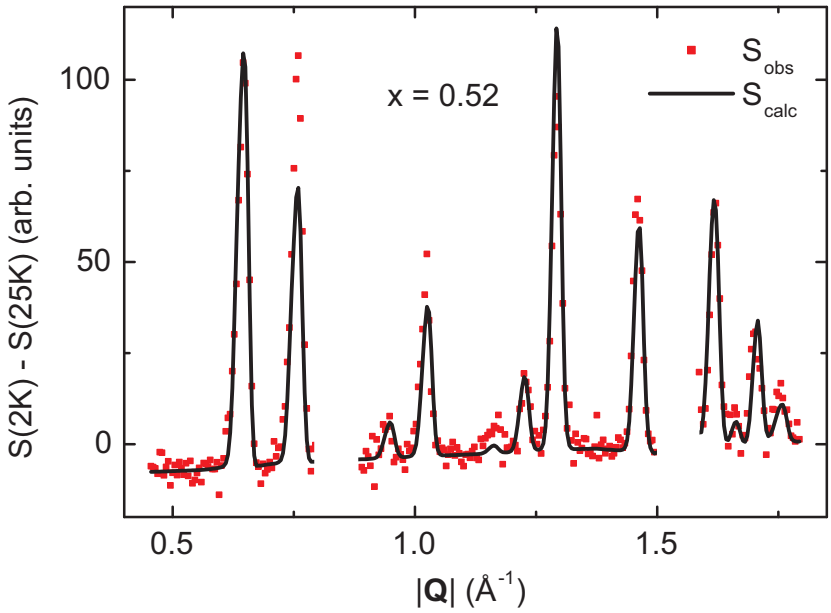

Figure 4.14: Magnetic scattering profile of polycrystalline $Cu_2Te_2O_5(Br_xCl_{1-x})_2$, $x = 0.52$. The calculated scattering profile (black) is the magnetic structure model VI determined by the single crystal refinement of $Cu_2Te_2O_5Br_2$ in section 4.3.1.

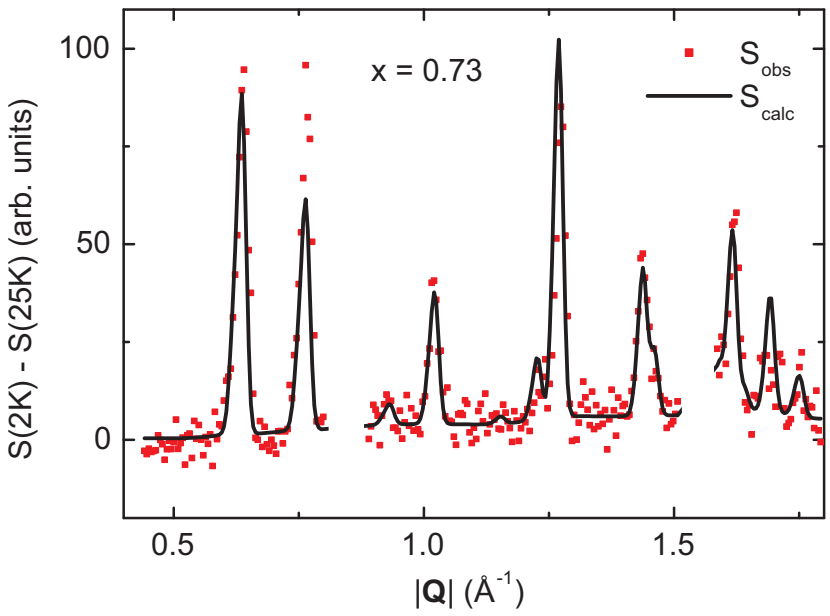

Figure 4.15: Magnetic scattering profile of polycrystalline $Cu_2Te_2O_5(Br_xCl_{1-x})_2$, $x = 0.73$. The calculated scattering profile (black) is the magnetic structure model VI determined by the single crystal refinement of $Cu_2Te_2O_5Br_2$ in section 4.3.1.

model provides a consistent fit to all of the compositions, with no clear indication that the magnetic structure is changing by a significant amount with doping. The moment, however, is quickly reduced with only a small substitution of Br for Cl, falling from ~ 1 μ_B/ion for $x = 0$ to ~ 0.65 μ_B/ion for $x = 0.25$. The moment value is further reduced with increasing x to ~ 0.48 μ_B/ion for $x = 1$. Although single crystal measurements of the doped compositions would be desirable, the evidence presented from the polycrystalline data strongly suggests that there is a very similar common magnetic structure for the compounds $Cu_2Te_2O_5(Br_xCl_{1-x})_2$, with a decreasing moment as x increases from 0 to 1.

4.5 Chapter summary

The magnetic structure of $Cu_2Te_2O_5(Br_xCl_{1-x})_2$ has been investigated with a combination of polycrystalline and single crystal neutron diffraction measurements. The magnetic structure of all compositions (x = 0, 0.25, 0.52, 0.73 and 1) was found to be incommensurate, with propagation vectors varying linearly with x from $\boldsymbol{\kappa}_{Cl} \approx$ [0.150, 0.420, 1/2] for X=Cl to $\boldsymbol{\kappa}_{Br} \approx$ [0.170, 0.350, 1/2] for X=Br. Several possible models for the magnetic structure of single crystal $Cu_2Te_2O_5Br_2$ have been refined and examined. These have a number of consistent features; (i) the Cu1 and Cu2 moments rotate in the same plane with a cant angle of $\sim 20^\circ$, (ii) the Cu3 and Cu4 moments rotate in the same plane with a cant angle of $\sim 120^\circ$, (iii) all four Cu moments rotate in planes that lie approximately in the xz-plane and (iv) the Cu moment is refined to be $\sim$ 0.40 μ_B/ion. However, this investigation does not provide a definite answer to the question of the underlying magnetic structure. The single crystal refined models have been applied to the polycrystalline data of all compositions and compared to the model proposed by Zaharko et al. for the $\boldsymbol{\kappa}_{Cl}$ structure of $Cu_2Te_2O_5Cl_2$ [80]. For the bromide, small discrepancies between the single crystal and polycrystalline refined moments are observed. This may possibly be attributed to the presence of different magnetic domains in the two cases, which could perhaps be the result of inhomogeneities in the samples. For the mixed composition samples, the data suggests that the magnetic structure of all compositions is reasonably similar to that refined for the single crystal $Cu_2Te_2O_5Br_2$ case, but with a significant reduction of the Cu moment with increasing x. However, the agreement and understanding of the magnetic structure in all of these compounds is still poor.

Chapter 5

Dynamic Magnetic Behaviour of $Cu_2Te_2O_5(Br_xCl_{1-x})_2$

5.1 Introduction and experimental details

There has been considerable debate over the nature of the ground states of $Cu_2Te_2O_5X_2$ (X=Br,Cl), an overview of which is presented in chapter 1. Whilst the previous chapter looked in detail at the magnetic *structure* of these materials below T_N, in this chapter the *dynamics* of the system are investigated. Neutron inelastic scattering measurements (NIS) will be described, in which the energy-momentum dispersion relations of the magnetic excitations are probed.

Polycrystalline samples of $Cu_2Te_2O_5(Br_xCl_{1-x})_2$ were prepared using the method described by Johnsson et al. [37]. Details of the samples growth and characterisation are presented in chapter 3. NIS measurements were carried out using the MARI time of flight chopper spectrometer at the ISIS pulsed neutron facility, Rutherford Appleton Laboratory, UK. Details of this instrument are given in section 2.3.5. In section 5.2.1 results obtained for the two end compounds, $Cu_2Te_2O_5Br_2$ and $Cu_2Te_2O_5Cl_2$, are presented. These results are then discussed in section 5.2.2. Sections 5.3.1 and 5.3.2 extend to the case of the intermediate

composition samples, $Cu_2Te_2O_5(Br_xCl_{1-x})_2$, and finally section 5.4 summarises the work presented in this chapter.

5.2 Neutron inelastic scattering of $Cu_2Te_2O_5X_2$ (X=Br,Cl)

5.2.1 Results

In order to access the low energy ($\hbar\omega$) and low momentum transfer ($|\mathbf{Q}|$) region that is of interest in this system, an incident energy of $E_i = 17$ meV and chopper frequency of 150 Hz were found to be optimal in terms of resolution and flux. In this configuration, a $|\mathbf{Q}|$ range of $\sim$ 0.5 to 5 Å^{-1} is accessible at an energy of 5 meV. This configuration has been used for all of the measurements discussed in this chapter. Figure 5.1 shows 2D plots of the raw neutron scattering data at 8 K for (a) $Cu_2Te_2O_5Br_2$ and (b) $Cu_2Te_2O_5Cl_2$. The y-axis is the energy transfer from the neutron to the sample, the x-axis is the momentum transfer, and the colour scale denotes the scattering intensity. The data is normalised with respect to the sample mass and molecular weight such that the colour scale is equivalent for both samples. Due to the polycrystalline nature of the samples, the scattering function $S(|\mathbf{Q}|, \hbar\omega)$ in these measurements is the powder average of $S(\mathbf{Q}, \hbar\omega)$, that is, a weighted average of all directions in momentum space.

The elastic line contains Bragg peaks, which can all be indexed on the basis of the crystal structure of $Cu_2Te_2O_5X_2$ (for more information see chapter 4). However, in this chapter it is the inelastic channels that are of interest. $S(|\mathbf{Q}|, \hbar\omega)$ shows a clear band of strong intensity centred about an energy of approximately 5 meV and 6 meV for X=Br and X=Cl respectively. The magnetic character of these peaks in $S(|\mathbf{Q}|, \hbar\omega)$ is seen from the decreasing intensity with increasing momentum transfer in the low $|\mathbf{Q}|$ region ($|\mathbf{Q}| < 3$ Å^{-1}). This is more clearly

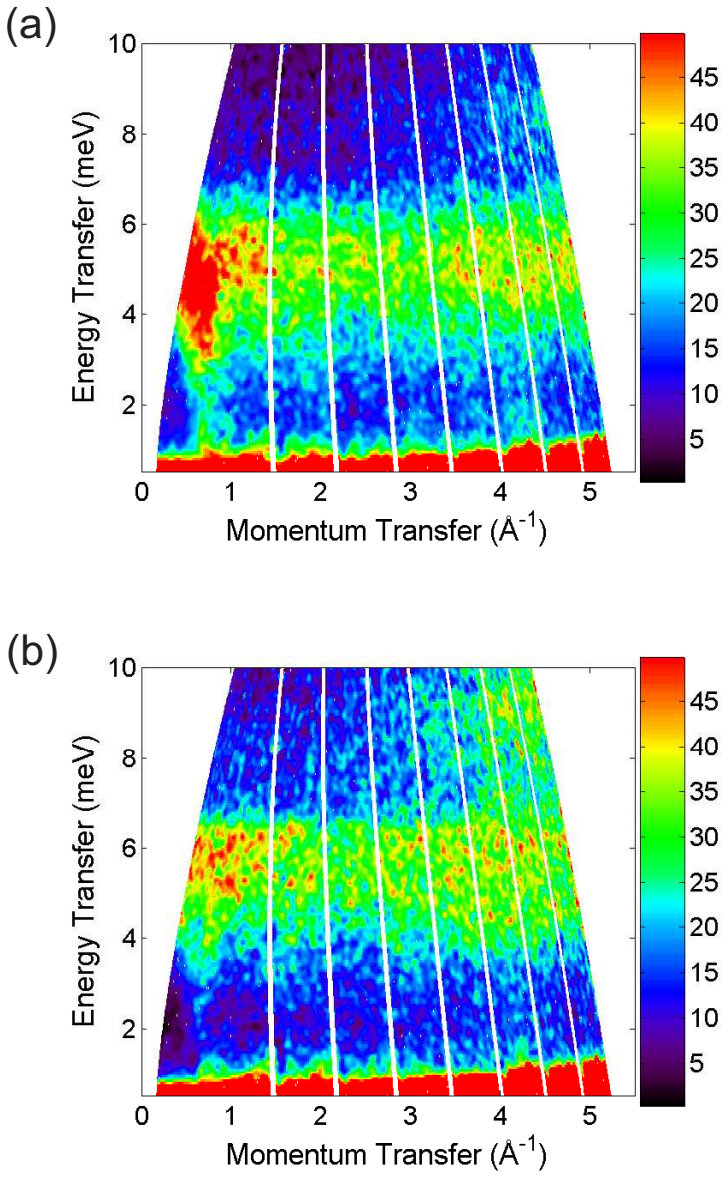

Figure 5.1: 2D map of the scattering intensity of (a) $Cu_2Te_2O_5Br_2$ and (b) $Cu_2Te_2O_5Cl_2$ as a function of energy transfer ($\hbar\omega$) and momentum transfer($|\mathbf{Q}|$), obtained at 8 K, with incident energy 17 meV. The colour scale denotes the scattering intensity ($S(|\mathbf{Q}|, \hbar\omega)$, arb. units), which is equivalent for both samples.

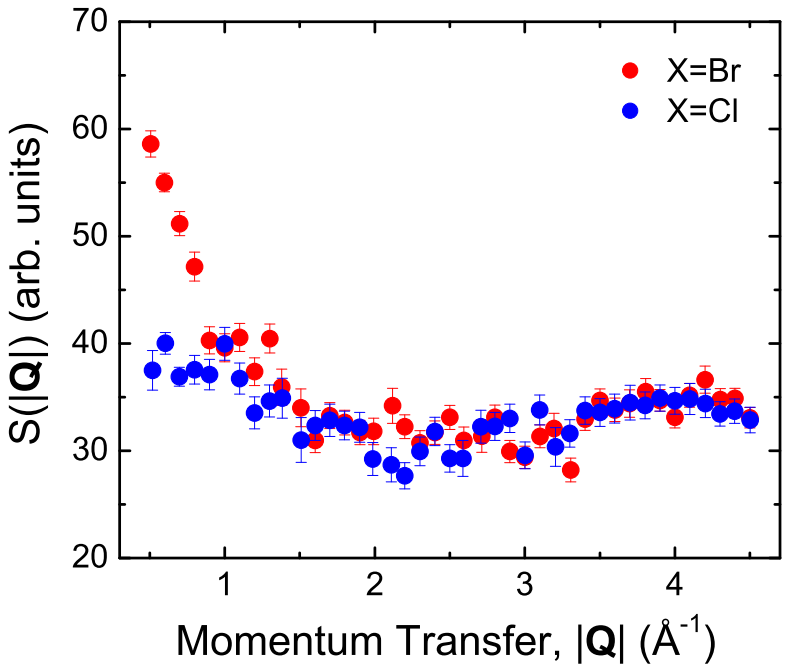

Figure 5.2: $S(|\mathbf{Q}|, \hbar\omega)$ as a function of momentum transfer for $Cu_2Te_2O_5Br_2$ (red) and $Cu_2Te_2O_5Cl_2$ (blue), taken at 8 K. The data was summed over an energy range 4 - 6 meV for X=Br and 4.75 - 6.75 meV for X=Cl.

illustrated in figure 5.2, which depicts $S(|\mathbf{Q}|, \hbar\omega)$ versus momentum transfer taken for the energy transfer range 4 - 6 meV for X=Br, and 4.75 - 6.75 meV for X=Cl.

It is clear from figures 5.1 and 5.2 that the bands of intensity centred at $\sim$ 5 meV (X=Br) and $\sim$ 6 meV (X=Cl) extend in to the high $|\mathbf{Q}|$ region, where one expects vanishing intensity of the magnetic excitation in both compounds due to the magnetic form factor. At $|\mathbf{Q}| = 3$ Å^{-1} the square of the Cu^{2+} form factor is $\sim 46\%$ of its value at $|\mathbf{Q}| = 0.5$ Å^{-1}, and by $|\mathbf{Q}| = 5$ Å^{-1} it is $\sim 14\%$. However, in this data the scattering intensity levels off to an almost constant value between 2 Å^{-1} $< |\mathbf{Q}| <$ 3 Å^{-1} and begins to increase above $|\mathbf{Q}| \sim 3$ Å^{-1}. This indicates the dominance of vibrational modes above ~ 3 Å^{-1}. Figure 5.3 shows $S(|\mathbf{Q}|, \hbar\omega)$ versus $\hbar\omega$ plots of the (a) bromide and (b) chloride, in which the data cuts have been summed over both the low (blue) and three highest (red) angle detector banks. The low angle detector bank covers scattering angles $3 < 2\theta <$

13^o. The corresponding $|\mathbf{Q}|$ range of the summation is energy dependent but does not vary significantly over the energy range of interest, and is approximately 0.5 Å^{-1} $< |\mathbf{Q}| <$ 1.4 Å^{-1}. Summing over an entire detector bank rather than a fixed $|\mathbf{Q}|$ range avoids problems with interpolation and extrapolation of the data. Similarly, the three highest angle detector banks together cover scattering angles $90^\circ < 2\theta < 135^\circ$, which corresponds approximately to 4 Å^{-1} $< |\mathbf{Q}| <$ 5 Å^{-1}. Throughout the text the low angle and three highest angle detector banks will be referred to as the 'low $|\mathbf{Q}|$' and 'high $|\mathbf{Q}|$' detector banks, or regions, respectively. The low $|\mathbf{Q}|$ region ($\sim$ 0.5 - 1.4 Å^{-1}) is dominated by the magnetic excitations, whilst the high $|\mathbf{Q}|$ region ($\sim$ 4 - 5 Å^{-1}) is dominated by vibrational modes. It can be seen that the magnon energy coincides with that of a peak in the phonon density of states, and also that a second peak in the phonon density of states at $\sim$ 9.5 meV is present in both samples, most strongly in the chloride.

One can attempt to subtract the phonon contribution by assuming a purely vibrational contribution to the inelastic scattering detected in the high angle detector bank ($120^\circ < 2\theta < 135^\circ$, which corresponds to 4.7 Å^{-1} $< |\mathbf{Q}| <$ 4.9 Å^{-1} at 5 meV). On this assumption, the phonon contribution as well as multiple scattering contribution as a function of $|\mathbf{Q}|$ and $\hbar\omega$ has been calculated using the DISCUS simulation program [36] (see section 2.3.6). The phonon and multiple scattering contributions have then been subtracted in order to obtain a purely magnetic response from our data, given the assumptions, which is shown in figure 5.4 as 2D plots of $S(|\mathbf{Q}|, \hbar\omega)$.

Figure 5.5 shows $S(|\mathbf{Q}|, \hbar\omega)$ versus momentum transfer for the corrected data, with the square of the Cu^{2+} magnetic form factor [9] also displayed (solid line). The square of the Cu^{2+} form factor has been normalised to the high $|\mathbf{Q}|$ region ($|\mathbf{Q}| >$ 3 Å^{-1}) of the data. For the X=Cl compound, the $|\mathbf{Q}|$-dependence of the scattering is close to that expected from the square of the Cu^{2+} form factor.

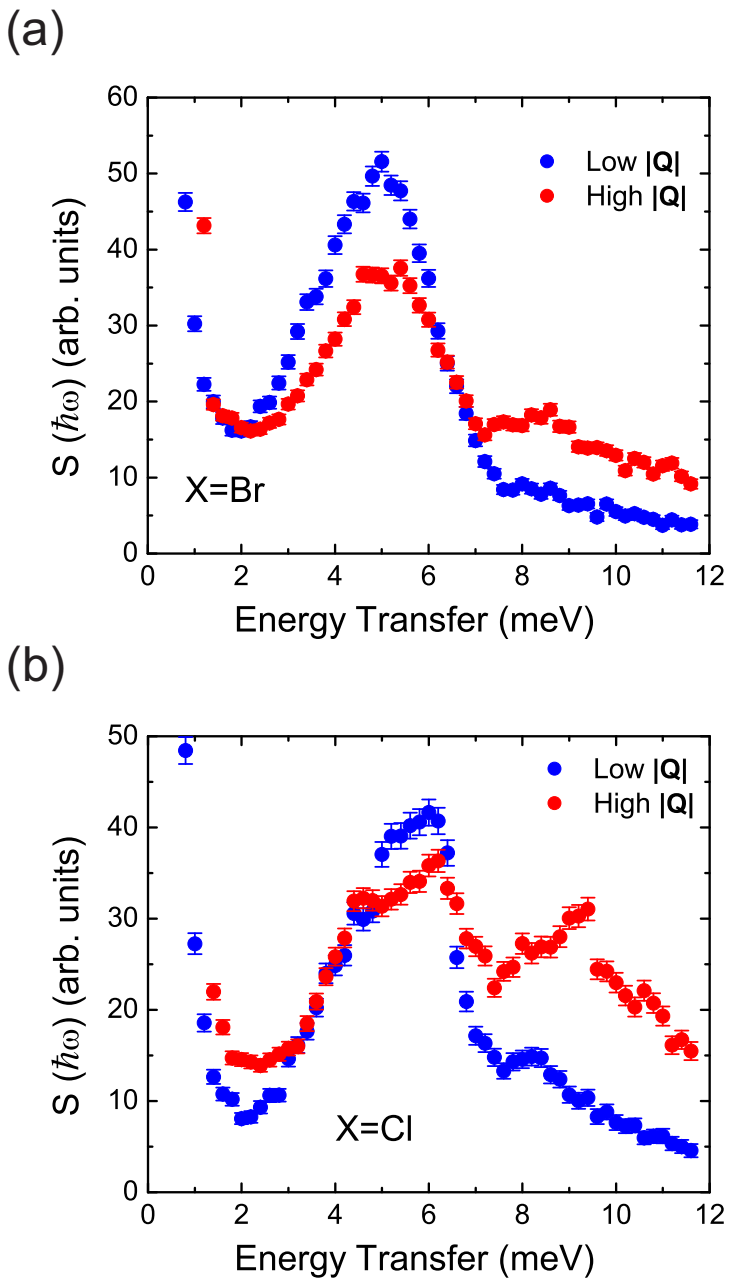

Figure 5.3: $S(|\mathbf{Q}|, \hbar\omega)$ versus $\hbar\omega$ for (a) $Cu_2Te_2O_5Br_2$ and (b) $Cu_2Te_2O_5Cl_2$, in which the data cuts have been summed in both low (blue) and high (red) regions of $|\mathbf{Q}|$. The low $|\mathbf{Q}|$ region corresponds to $\sim$ 0.5 - 1.4 Å^{-1} and the high $|\mathbf{Q}|$ region corresponds to $\sim$ 4 - 5 Å^{-1}.

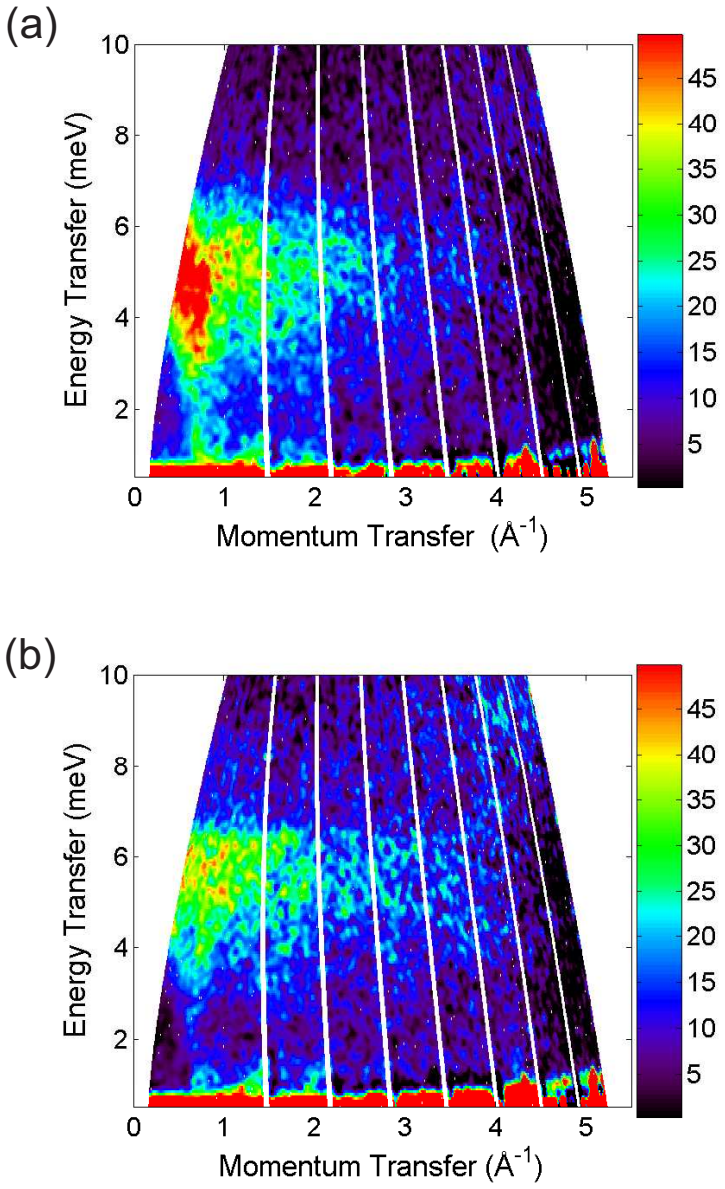

Figure 5.4: 2D map of the scattering intensity of (a) $Cu_2Te_2O_5Br_2$ and (b) $Cu_2Te_2O_5Cl_2$ with corrections made for phonon and multiple scattering.

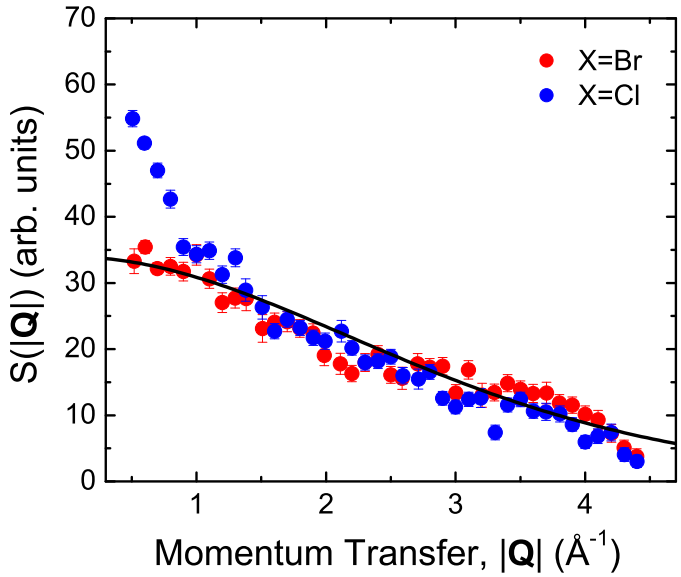

Figure 5.5: $S(|\mathbf{Q}|, \hbar\omega)$ as a function of momentum transfer for $Cu_2Te_2O_5Br_2$ (red) and $Cu_2Te_2O_5Cl_2$ (blue), with phonon and multiple scattering corrections applied to the data. The solid line is the square of the Cu^{2+} magnetic form factor [9], which has been normalised to the high $|\mathbf{Q}|$ region ($|\mathbf{Q}| > 3$ Å^{-1}) of the data.

However, whilst for the X=Br compound the $|\mathbf{Q}|$-dependence of the scattering above $\sim$ 1.5 Å^{-1} is also close to that expected from the square of the Cu^{2+} form factor, at low $|\mathbf{Q}|$ (< 1 Å^{-1}) the scattering intensity shows a clear deviation from the square of single-ion Cu^{2+} form factor. This suggests that there is a structure factor effect in addition to the form factor, which arises from a larger sized scattering entity, the nature of which (e.g. tetrahedral or square planar arrangement of Cu^{2+} ions) depends upon the relative strength of the exchange interactions present.

In the 2D plots for inelastic scattering of $Cu_2Te_2O_5X_2$ (figure 5.4), two components to the magnetic excitations are observed; a flat, constant energy ($\sim$ 5 meV for X=Br and $\sim$ 6 meV for X=Cl) component that falls in intensity with increasing $|\mathbf{Q}|$ as previously discussed, and a narrow, dispersive band of intensity centered at $|\mathbf{Q}| \sim 0.7$ Å^{-1} in the energy range around 1 to 4 meV. Figure 5.6 shows $S(|\mathbf{Q}|, \hbar\omega)$ versus $|\mathbf{Q}|$ summed over three different energy regions for each

compound; 1.5 - 2.75 meV (green), 2.75 - 4 meV (blue) and 4 - 6 meV (red) for X=Br, and 1.5 - 2.5 meV (green), 2.5 - 4 meV (blue) and 4.75 - 6.75 meV (red) for X=Cl. The high energy cuts (4 - 6 meV (X=Br), 4.75 - 6.75 meV (X=Cl)) are centred on the flat mode of each sample, and are the same as those shown in figure 5.2, the $|\mathbf{Q}|$-dependence of which were discussed above. However, the lower energy cuts show a rather different $|\mathbf{Q}|$-dependence, due to the dispersive nature of the excitation in this region. In both samples the scattering intensity peaks at $|\mathbf{Q}| \sim 0.7$ Å^{-1}, and falls toward zero as $|\mathbf{Q}|$ decreases further.

In chapter 4, neutron diffraction measurements of polycrystalline $Cu_2Te_2O_5X_2$ (X=Cl,Br) were presented. The lowest order (and strongest intensity) magnetic peaks arising from the incommensurate magnetic order were observed at $|\mathbf{Q}|=$ 0.63 and 0.77 Å^{-1} for X=Br, and $|\mathbf{Q}|=$ 0.66 and 0.74 Å^{-1} for X=Cl respectively (see figure 4.3 in section 4.2.1). The dispersive component observed in NIS measurements appears to stretch towards the magnetic Bragg peaks, suggesting that the dispersive excitations are supported by the incommensurate magnetic order. In the bromide, the dispersive excitations are particularly clear, and no gap is resolved between the excitation and the elastic magnetic Bragg peak. However, in the chloride there appears to be an energy gap between the magnetic Bragg peaks and the excitation of ~ 2 meV, although this is difficult to ascertain precisely due to the weak intensity of the dispersive component in this compound.

The energy dependence of the magnetic peak in each compound at $T =$ 8 K is shown in figure 5.7, which is an $S(|\mathbf{Q}|, \hbar\omega)$ versus $\hbar\omega$ plot of the raw data (not corrected for phonon and multiple scattering), summed over the low $|\mathbf{Q}|$, 0.5 Å^{-1} $< |\mathbf{Q}| <$ 1.4 Å^{-1}, region. The red (blue) line shows the non-magnetic background for the X=Br (X=Cl) sample, as determined by the multiple scattering and phonon corrections discussed previously. It should be noted that in this $|\mathbf{Q}|$ range the non-magnetic contribution to the overall scattering is very small. For both samples the excitation has a width that it is not resolution limited

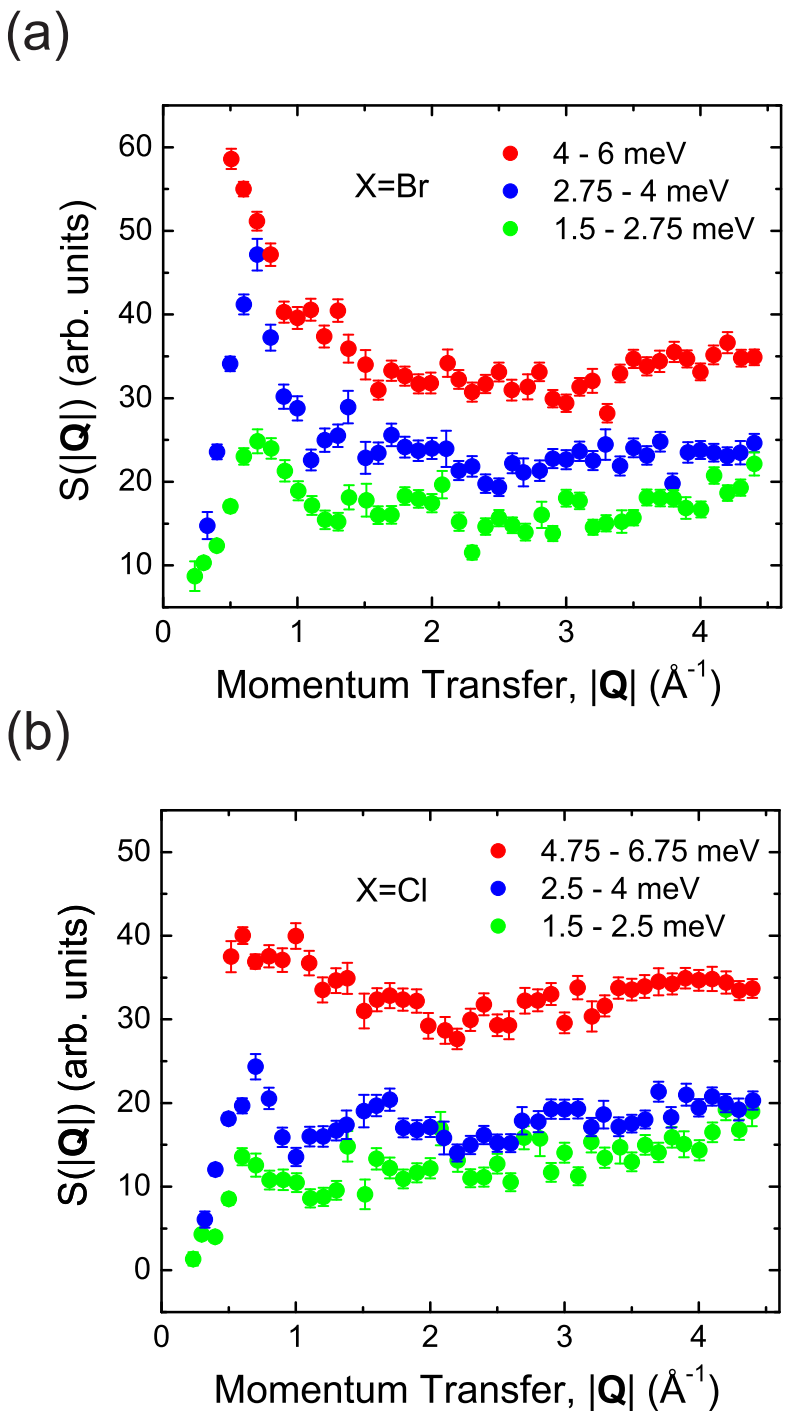

Figure 5.6: Scattering intensity of (a) $Cu_2Te_2O_5Br_2$ and (b) $Cu_2Te_2O_5Cl_2$ as a function of momentum transfer at 8 K. The cuts are taken over an energy range 1.5 - 2.75 meV (green), 2.75 - 4 meV (blue) and 4 - 6 meV (red) for X=Br and 1.5 - 2.5 meV (green), 2.5 - 4 meV (blue) and 4.75 - 6.75 meV (red) for X=Cl.

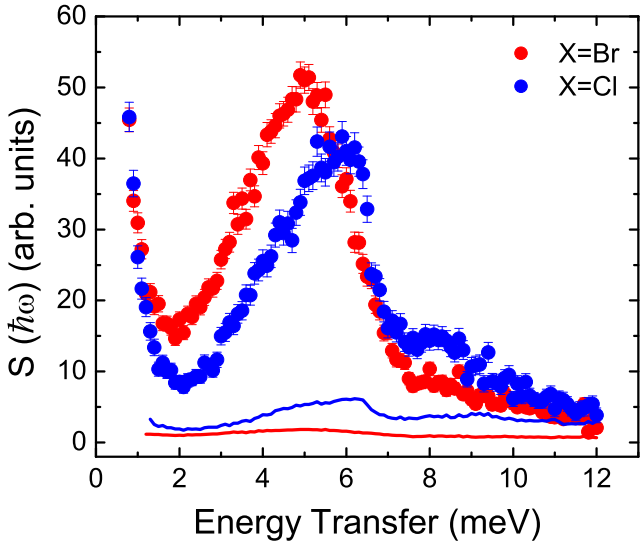

Figure 5.7: $S(|\mathbf{Q}|, \hbar\omega)$ versus energy transfer for $Cu_2Te_2O_5Br_2$ and $Cu_2Te_2O_5Cl_2$, summed over the low $|\mathbf{Q}|$ region (approximately 0.5 Å$^{-1} < |\mathbf{Q}| <$ 1.4 Å^{-1}), taken at T = 8 K. This data is not corrected for multiple and phonon scattering, however, the red (blue) line shows the contribution of the non-magnetic background for X=Br (X=Cl), as determined by the phonon and multiple scattering calculations.

(the instrumental resolution is $\sim$ 0.5 meV at 5 meV), which may reflect the dispersive nature of the excitations, lifetime effects, or possibly the fact that there are several branches of the excitations. In the bromide sample only one peak is resolved, which is Gaussian in shape to a reasonable approximation. In contrast, the chloride excitation peak is asymmetric, with a sharp fall on the high energy side, and appears to be made up of constituent peaks. Again, this structure may be due to the dispersion of the excitations.

Figure 5.8 shows 2D plots of the scattering intensity for data taken at 15 K, 25 K and 50 K for both compounds. This data has not been corrected for phonon and multiple scattering. As before, the colour scale denotes the scattering intensity, whilst the x and y-axes are the momentum and energy transfer respectively. The temperature dependence (at 8 K, 15 K, 25 and 50 K) of the $S(|\mathbf{Q}|, \hbar\omega)$ versus $\hbar\omega$ data is shown for the Br and Cl compounds in figures 5.9. Again, the data is

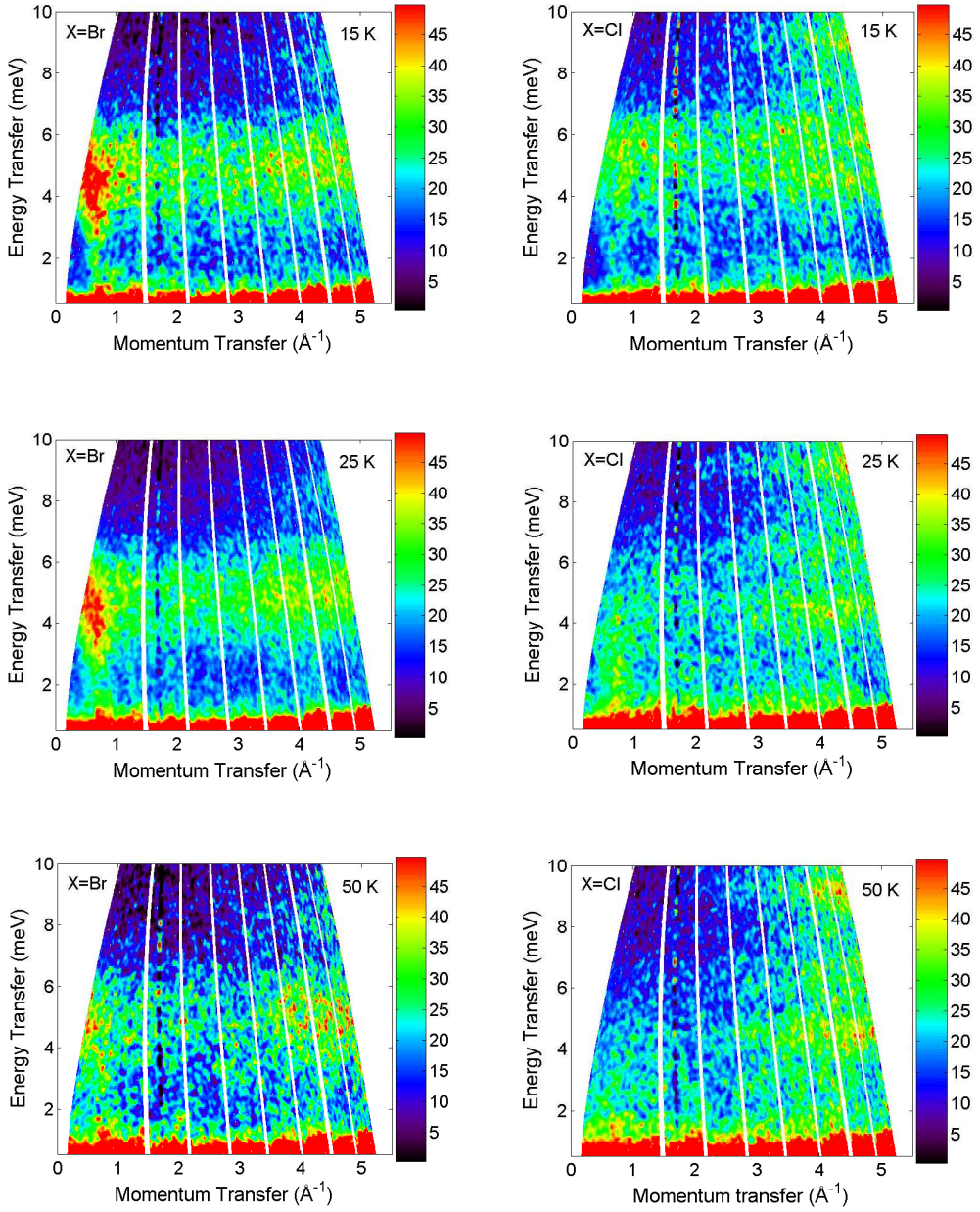

Figure 5.8: 2D colour plot of the scattering intensity of $Cu_2Te_2O_5Br_2$ (lefthand column) and $Cu_2Te_2O_5Cl_2$ (righthand column) as a function of energy and momentum transfer. The first, second and third rows are data collected at T =15 K, 25 K and 50 K respectively.

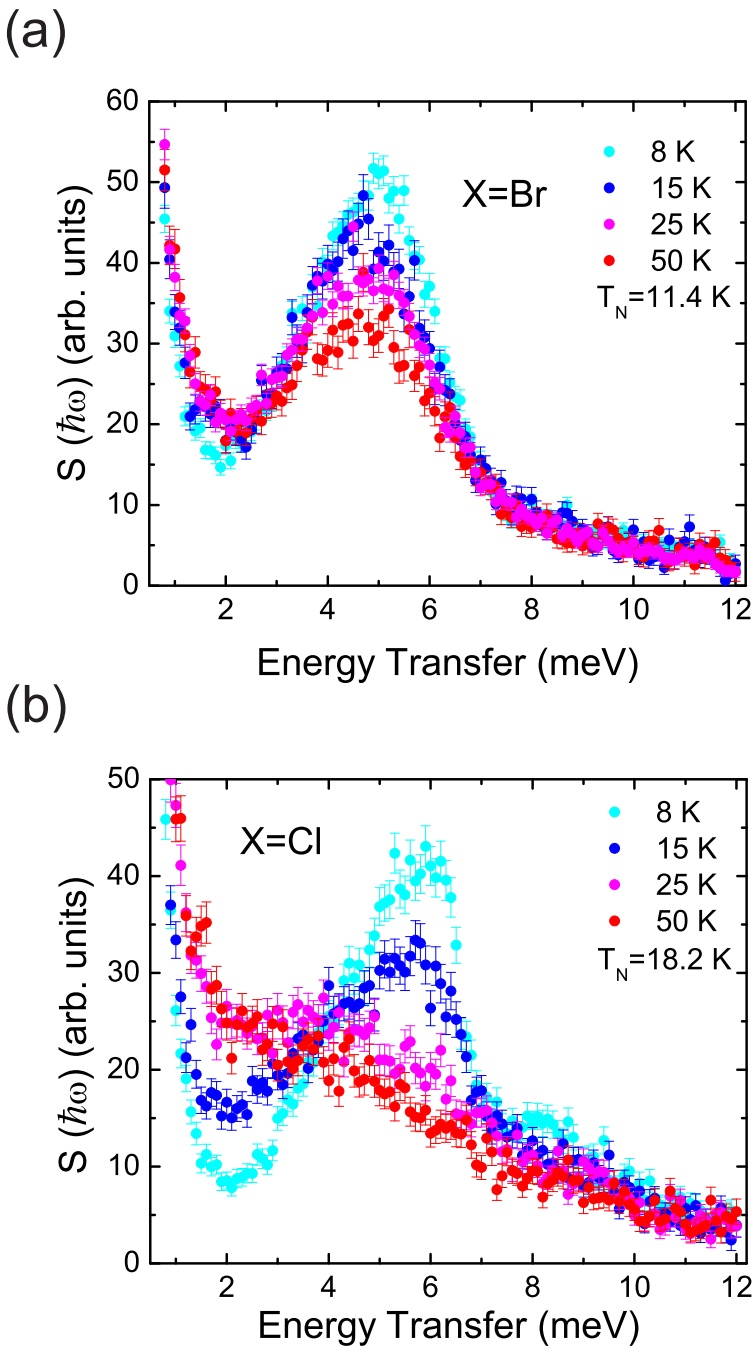

Figure 5.9: Scattering intensity versus energy transfer at 8 K, 15 K, 25 K and 50 K for (a) $Cu_2Te_2O_5Br_2$ and (b) $Cu_2Te_2O_5Cl_2$. The data is summed over the low $|\mathbf{Q}|$ detector bank (approximately 0.5 Å^{-1} $< |\mathbf{Q}| <$ 1.4 Å^{-1}). This data is not corrected for phonon and multiple scattering, which give only a small contribution to the overall scattering in this low $|\mathbf{Q}|$ region.

summed over the low $|\mathbf{Q}|$ detector bank (0.5 Å^{-1} $< |\mathbf{Q}| <$ 1.4 Å^{-1}). The data shown is not corrected for phonon and multiple scattering, which only has a small contribution in this low $|\mathbf{Q}|$ region (see figure 5.7).

The two compounds show a striking contrast in their temperature dependence. Firstly, for $Cu_2Te_2O_5Br_2$ the integrated intensity of the peak decreases smoothly with increasing temperature, showing no change in lineshape across the transition temperature $T_N^{Br} \sim$ 11.4 K. Both the flat, constant energy component and the dispersive component are present at all temperatures, falling uniformly in intensity with increasing temperature. A very different temperature dependence is observed in the X=Cl compound, in which the centre of mass of the scattering moves to lower energy with increasing temperature. Initially, a fall in the intensity of the 6 meV peak is observed when the temperature increases from 8 K to 15 K, accompanied by an increase in the intensity around 2.5 meV. However, above the transition temperature T_N^{Cl} =18.2 K, the inelastic structure is replaced by a quasi elastic lineshape from a diffusive response.

5.2.2 Discussion

The results presented in section 5.2.1 are concerned with the nature of the magnetic excitations in $Cu_2Te_2O_5X_2$ (X=Br,Cl). These results are now discussed with respect to the underlying magnetic interactions.

Firstly, the case in which the system consists of independent tetrahedra of Cu^{2+} ions will be considered. In this model, the excitations are dispersionless, and the $|\mathbf{Q}|$-dependence follows the structure factor of a single tetrahedron, characterised by exchange couplings on intra-tetrahedral distances. In our data, the dispersionless component of the excitations centered at $\sim$ 5 meV (X=Br) and 6 meV (X=Cl) would correspond, in the isolated tetrahedral model, to singlet-triplet spin-gaps of $\Delta_{Br} = 5$ meV and $\Delta_{Cl} = 6$ meV. This does not compare closely with Raman scattering measurements, which in the bromide show evidence

of a singlet-triplet excitation of $\sim$ 3.7 meV [46, 27]. In addition, below T_N^{Br} a lower energy peak appears in Raman spectra at $\sim$ 2.2 meV, which is associated with an excitation between a ground state singlet and a low lying excited singlet. No clear evidence of magnetic excitations is observed in Raman scattering of the chloride, in contrast to the measurements presented here.

However, for the system to magnetically order there must be some form of interaction between the tetrahedra. If one takes inter-tetrahedral coupling into account, the magnetic units of interest may no longer be tetrahedra but, for example, plaquettes such as the square planar arrangement displayed in figure 1.9, which is mediated by exchange couplings that act over longer inter-tetrahedral distances. If these are non-interacting then they also give rise to dispersionless excitations, but with a $|\mathbf{Q}|$-dependence arising from the structure factor of an inter-tetrahedral exchange configuration. The presence of larger scattering entities would manifest itself in the superposition of $|\mathbf{Q}|$-dependent oscillations about the square of the single-ion form factor (see section 2.3.1). This would be most dominant at low $|\mathbf{Q}|$ and dampen with increasing $|\mathbf{Q}|$. The difference observed between the $|\mathbf{Q}|$-dependence of the scattering functions for $Cu_2Te_2O_5Br_2$ and $Cu_2Te_2O_5Cl_2$ is indicative of different underlying exchange configurations. In the bromide, the steep fall in scattering intensity with increasing $|\mathbf{Q}|$ in the low $|\mathbf{Q}|$ region compared to the square of the Cu^{2+} form factor suggests the importance of exchange interactions on an inter-tetrahedral length scale. For scattering from a finite spin cluster it is expected that $S(|\mathbf{Q}|,\omega) \rightarrow 0$ as $|\mathbf{Q}| \rightarrow 0$ (see section 2.3.1). In this data an increase in $S(|\mathbf{Q}|,\omega)$ with decreasing $|\mathbf{Q}|$ is seen in the flat mode. However, in this experimental configuration the lowest accessible momentum transfer is $|\mathbf{Q}| \sim 0.6$ Å^{-1} in the energy region of interest. This suggests that there should be a peak in $S(|\mathbf{Q}|,\omega)$ below $|\mathbf{Q}| \sim 0.6$ Å^{-1}. To a first approximation, the structure factor of the scattering can be represented by $1-\frac{\sin(|\mathbf{Q}|R)}{|\mathbf{Q}|R}$, where R is the length scale of the exchange interactions (see equation 2.9). The function $1-\frac{\sin(|\mathbf{Q}|R)}{|\mathbf{Q}|R}$ is greatest at

$|\mathbf{Q}|R = 4.517$, and hence we expect a peak in the scattering intensity at $|\mathbf{Q}|R \sim 4.5$. A peak in $S(|\mathbf{Q}|)$ below $|\mathbf{Q}| \sim 0.6$ Å^{-1} therefore implies a length scale for the magnetic exchange interactions of greater than $R \sim 8$ Å. The intra-tetrahedral Cu-Cu distance in both the X=Br and X=Cl compounds is approximately 3 Å, whereas the inter-tetrahedral distances in the $(a \pm b)$-direction (J_a) and a and b directions (J_b), are approximately 8 Å and 6 Å respectively. As discussed in section 1.3.4, Whangbo et al. [78] argue that the strongest exchange interaction is J_a for both compounds. This data indicates that the interaction path length $\geq$ 8 Å has an important role in the magnetic excitation of these compounds.

The presence of inter-tetrahedral couplings also produces a splitting of the energy states of the isolated tetrahedral model, thereby allowing several excitation modes, and the presence of multiple peaks. As the relative population of the energy states develop with temperature, so would the relative intensity of the corresponding excitation peaks. In this data, multiple peaks cannot be resolved and therefore an effect such as this is not observed.

Inter-tetrahedral correlations also allow for dispersive modes, which are not present in the isolated unit model. The data shows clear evidence of dispersive magnetic excitations, which are associated with the magnetic Bragg peaks that arise from the incommensurate order below T_N. In an isotropic antiferromagnet there is no gap in the excitation spectrum at the Brillouin zone (BZ) centre. Whilst a gap cannot be resolved in the bromide, a clear gap is observed in the chloride between the bottom of the dispersive excitation (at $\sim$ 2 meV) and the elastic line, which implies anisotropy of the system. Both Jensen et al. [35] and Kotov et al. [42] introduce a Dzyaloshinskii-Moriya anisotropy term in the Hamiltonian describing the system, which goes some way to explaining the Raman scattering results and the observed anisotropy of the magnetic susceptibility below T_N. In addition, Prester et al. invoke the assumption of a gap in the excitation spectrum of the chloride but not the bromide to enable a good explanation of their thermal

conductivity measurements [61]. The dispersion of excitations in a conventional antiferromagnet is approximately linear at the BZ centre, and flattens off at the zone boundary. This behaviour is observed in the low $|\mathbf{Q}|$ region of our data ($|\mathbf{Q}|$ <1.5 Å^{-1}), but does not repeat itself periodically as we move to larger $|\mathbf{Q}|$. This is due to the fact that this is a polycrystalline measurement in which the scattering intensity at a given $|\mathbf{Q}|$ is the average intensity over a sphere of radius $|\mathbf{Q}|$ in reciprocal space. At low $|\mathbf{Q}|$, the scattering sphere only encompasses a small number of BZs and therefore the strongly dispersive centre of the zone is sampled effectively. At large $|\mathbf{Q}|$ the scattering intensity is averaged over a sphere covering many BZs, and therefore approaches a density of states for the magnetic excitations, which the flat component at the zone boundary dominates. Therefore, in this data only the flat component of the excitations is seen at high $|\mathbf{Q}|$, and the dispersive feature appears only at low $|\mathbf{Q}|$. In fact, it is unclear in this data whether the flat component is a separate dispersionless excitation, or arises from the flat part of the dispersive excitation at the zone boundary. In order to fully understand the dispersive excitations in this system, single crystal inelastic measurements are required. Indeed, recent single crystal NIS results for the chloride by Zaharko et al. [81] are of useful comparison with the data presented here. In scanning along the $\mathbf{Q}$=(h, $h/3$, 3/2), (0.45, 0.15, l) and (0, 0, l) directions they observe two well defined excitation modes; one completely dispersionless mode centred at 6 meV and a second mode that is strongly dispersive along both accessible directions from a maximum energy close to the flat mode, down to 2.1 meV, and centred at the same position in $\mathbf{Q}$ as the incommensurate Bragg peaks. Whilst no data is shown in their work, the description agrees extremely well with the data presented and discussed in this chapter.

Another question of interest in this system is the role of magnon-phonon coupling. In particular, thermal conductivity measurements [61] point toward the prominent role of spin-lattice interactions in determining the ground state prop-

erties of the $Cu_2Te_2O_5X_2$ (X=Br,Cl) compounds, and predict the existence of enhanced magnetic-phonon coupling in the X=Cl compound. In the NIS data presented above, the presence of a peak in the phonon density of states at approximately the same energy as the magnon excitation in both compounds suggests the possibility of spin-lattice coupling. Nevertheless, the phonon scattering intensity above $|\mathbf{Q}| \geq 2$ Å^{-1} (see figure 5.2) is found to be identical (within the statistics of our measurements) for both compounds. The approximate corrections made for phonon scattering are based on the assumption that the high angle region ($120^o < 2\theta < 135^o$) contains only phonon scattering. Extrapolating back, using the $\mathbf{Q}^2$-dependence of phonon scattering, the subtraction leaves a contribution which falls off with the square of the Cu^{2+} form factor in the case of the chloride. As discussed above, for the bromide there is also a superposition of the structure factor on top of the single ion form factor, which is most noticeable at low $|\mathbf{Q}|$. If this assumption is incorrect, and the high angles contain non-phonon scattering (for example, from a strong spin-lattice interaction), then such a subtraction is no longer appropriate. Whether or not the spin-lattice coupling plays an important role in the magnetic transition in the chloride (see [61]) remains to be seen. In order to investigate the magneto-elastic coupling further one could measure a sample that is considered to be an appropriate phonon blank, from which a more direct subtraction can be made. Alternatively, the phonon modes could be investigated in a single crystal NIS experiment.

The difference in the observed temperature dependence of these two materials is particularly interesting. $Cu_2Te_2O_5Cl_2$ shows a structured inelastic response below the magnetic ordering transition, T_N^{Cl}, and a diffusive response corresponding to short range correlations in the paramagnetic state. $Cu_2Te_2O_5Br_2$ on the other hand, shows a rather different temperature dependence with respect to the transition at T_N^{Br}. In fact, the excitation spectra shows no significant change at T_N^{Br}, but continues to fall uniformly with increasing temperature, similar to what

might be expected from a two-level system such as a simple singlet-triplet configuration. However, the dispersive component of the excitation is present well above T_N^{Br}, and falls in intensity at the same rate as the flat component with increasing temperature. A tendency of the system to short range order, or the build up of low dimensional order well above T_N^{Br} may provide a mechanism by which the dispersive excitations are supported above T_N^{Br}, thus explaining the temperature dependence observed in the bromide. This may also explain the small anomaly at T_N^{Br} observed in heat capacity measurements (see figure 3.6), as the presence of low dimensional correlations at higher temperatures results in less entropy being associated with the transition to 3D long range order. As discussed in section 3.3, a maximum of 29% of the magnetic entropy is accounted for below T_N^{Br} in heat capacity measurements, suggesting that a large amount of magnetic entropy is tied up in magnetic correlations well above T_N^{Br}.

Despite the similarity of the incommensurate magnetic order of these materials below $T_N^{Br,Cl}$, the nature of their transitions are markedly different, as supported by heat capacity [46] and thermal conductivity [69] measurements in addition to the results presented here and in section 3.3.

5.3 Neutron inelastic scattering of $Cu_2Te_2O_5(Br_xCl_{1-x})_2$

After considering the dynamic magnetic behaviour of $Cu_2Te_2O_5Br_2$ and $Cu_2Te_2O_5Cl_2$, their stark differences raise the obvious question, what happens when one substitutes Cl for Br and forms intermediate compositions? In chapter 4 it was shown that the low temperature magnetic structure of intermediate compositions are similar to both end compounds, with a smooth change in the incommensurate wave vector on substitution of Cl for Br. Neutron inelastic scattering results will now be presented that shed light on the development of the *dynamics* of the system as a function of composition.

5.3.1 Results

As with the X=Br and Cl samples, the optimal configuration for flux and resolution of the MARI spectrometer for the energy-momentum region of interest is an incident energy of 17 meV and chopper frequency of 150 Hz. Figures 5.10 and 5.11 are 2D plots of the raw neutron scattering data at 5 K for the compositions $x =$ 0.73 and 0.62, and $x =$ 0.52 and 0.25 respectively. The colour scales represent the intensity of the powder average of the spin-spin correlation function $S(|\mathbf{Q}|, \hbar\omega)$, and have been normalised to the mass and molecular weight of the sample.

When comparing these figures with figure 5.1, it is immediately clear that doping has a significant effect on the inelastic scattering. First consider the compositions $x =$ 0.63 and 0.73 shown in figure 5.10. Whilst there is a single band of intensity centred at $\sim$ 5 meV and $\sim$ 6 meV for the X=Br and X=Cl samples respectively, there are two bands of intensity present in the $x =$ 0.62 and 0.73 samples. The main excitation has shifted down to an energy centred at $\sim$ 4 meV, and a second mode appears at $\sim$ 7 meV in both samples. This is illustrated more clearly in figure 5.12, which shows $S(|\mathbf{Q}|, \hbar\omega)$ versus $\hbar\omega$, summed over the low angle detector bank ($3 < 2\theta < 13^o$, which corresponds approximately to the $|\mathbf{Q}|$ range 0.5 Å^{-1} $< |\mathbf{Q}| <$1.4 Å^{-1}) for the compositions $x =$ 0.73 and 0.62 as well as for the X=Br and Cl samples. The main peak has a narrower width than the X=Br sample, and the second mode is an approximately 2 meV wide shoulder on the high energy side.

In the 2D plots (see figure 5.11) of the $x =$ 0.52 and 0.25 samples it appears that there is only one mode, similar to the X=Br and Cl samples, and that the higher energy mode is no longer present. However, on closer inspection of the $S(|\mathbf{Q}|, \hbar\omega)$ versus $\hbar\omega$ plot (see figure 5.13), one can see that whilst the width and position of the main peak takes on a similar character to that of the end compounds, a shoulder is still present on the high energy side of both the x = 0.25 and 0.52 compounds. Indeed, in the X=Cl sample there is also a small

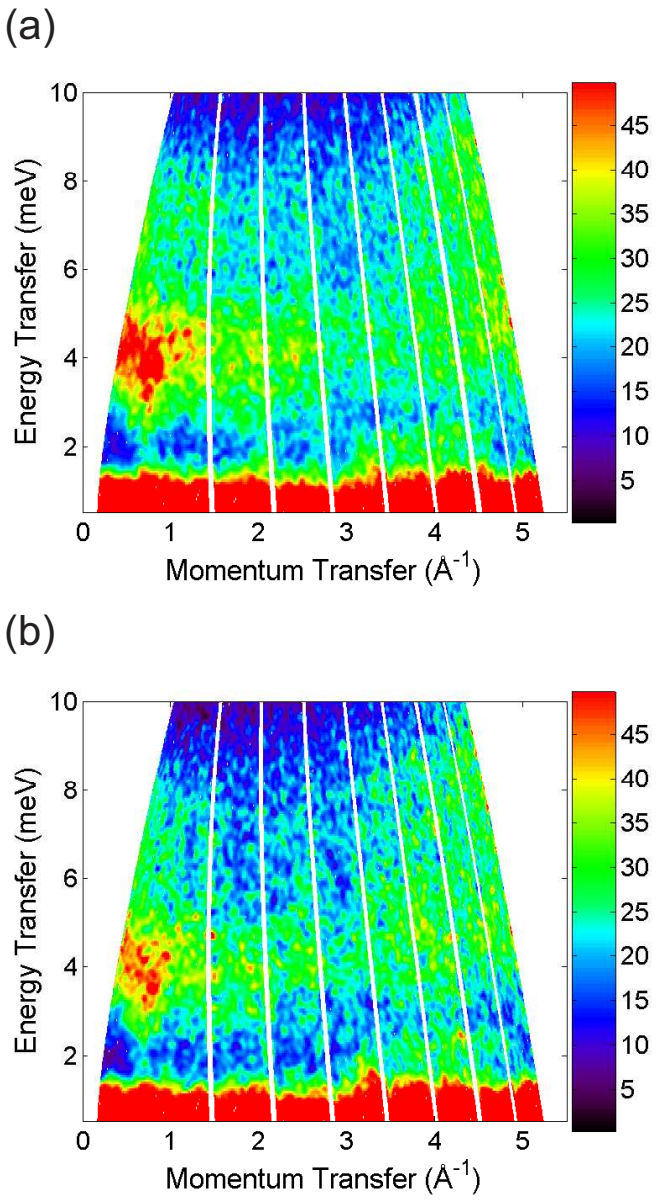

Figure 5.10: 2D map of the scattering intensity of composition (a) $x = 0.73$ and (b) $x = 0.62$ as a function of energy transfer ($\hbar\omega$) and momentum transfer ($|\mathbf{Q}|$), obtained at 5 K, with incident energy 17 meV. The colour scale denotes the scattering intensity ($S(|\mathbf{Q}|, \hbar\omega)$, arb. units).

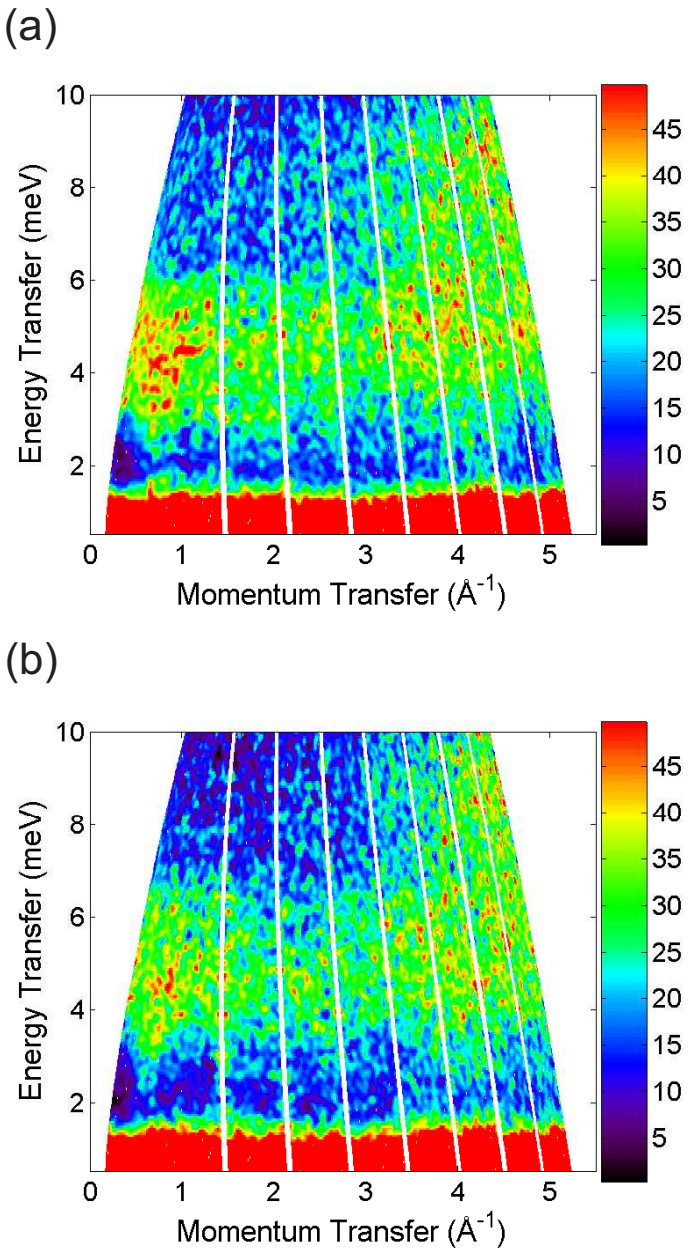

Figure 5.11: 2D map of the scattering intensity of composition (a) $x = 0.52$ and (b) $x = 0.25$ as a function of energy transfer ($\hbar\omega$) and momentum transfer ($|\mathbf{Q}|$), obtained at 5 K, with incident energy 17 meV. The colour scale denotes the scattering intensity ($S(|\mathbf{Q}|, \hbar\omega)$, arb. units).

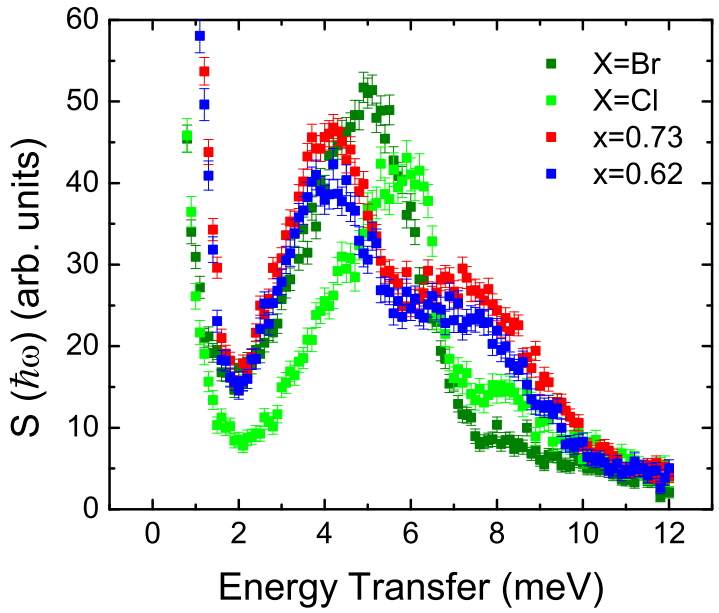

Figure 5.12: $S(|\mathbf{Q}|, \hbar\omega)$ versus $\hbar\omega$, summed over the low $|\mathbf{Q}|$ region (approximately 0.5 Å^{-1} $< |\mathbf{Q}| <$ 1.4 Å^{-1}) for the compositions x = 0, 0.62, 0.73 and 1.

shoulder-like feature in the data at $\sim$ 8 meV, which appears to become more accentuated with doping. However, the lowering of the main peak energy, and the very distinct double mode present in the composition around $x = 0.7$ seems to be somewhat localised in composition. Before proceeding further, it is worth noting that these effects are not believed to be due to phase separation. The sample growth and characterisation of these compounds are discussed in chapter 3. X-ray diffractometry shows well-resolved single peaks for all compositions. Moreover, the temperature dependence of heat capacity and susceptibility measurements reveal a single, distinct anomaly for each composition.

Figure 5.14 shows $S(|\mathbf{Q}|, \hbar\omega)$ versus $|\mathbf{Q}|$ cuts of the (a) $x = 0.25$ and (b) $x = 0.52$ data over the energy regions 1.75 - 4 meV and 4 - 6 meV. In both samples a similar two-component structure to the magnetic excitations are observed as in the case of X=Br and Cl. A flat, constant energy component centred at $\sim$ 5 meV in both compounds falls in intensity with increasing $|\mathbf{Q}|$ in the low $|\mathbf{Q}|$ region ($|\mathbf{Q}| <$

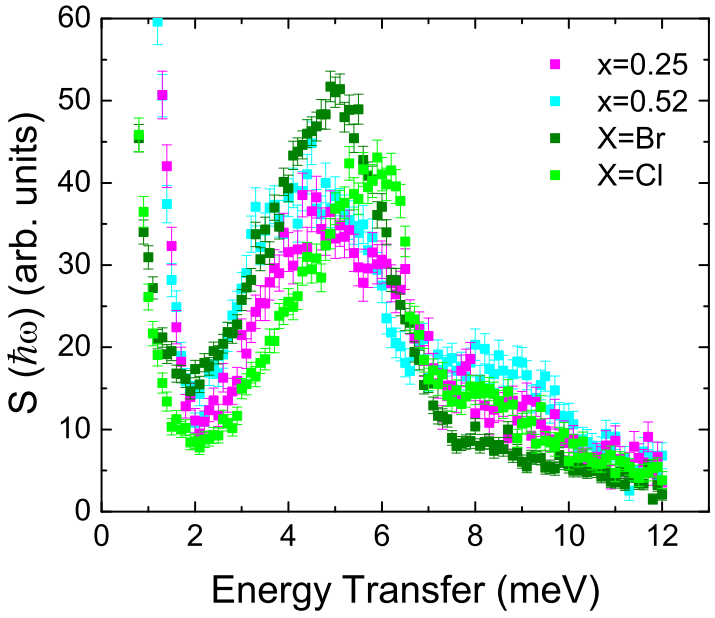

Figure 5.13: $S(|\mathbf{Q}|, \hbar\omega)$ versus $\hbar\omega$, summed over the low $|\mathbf{Q}|$ region (approximately 0.5 Å^{-1} $< |\mathbf{Q}| <$ 1.4 Å^{-1}) for the compositions x = 0, 0.25, 0.52 and 1.

3 Å^{-1}). A second, dispersive component is also present in both, which as seen in figure 5.14, is centred at $|\mathbf{Q}| \sim 0.7$ Å^{-1}. As in the X=Cl and Br compounds, the dispersive excitations are therefore centred on the incommensurate Bragg peaks. Whilst there appears to be an energy gap between the excitation at $\sim$ 2 meV and the elastic line, it is difficult to resolve a gap within the statistics of the experiment.

In the x = 0.62 and 0.73 compositions, the low energy excitation mode also has two components; a flat, dispersionless component centred at about 4 meV, and a dispersive component that stretches towards the magnetic Bragg peaks. Figure 5.15 depicts $S(|\mathbf{Q}|, \hbar\omega)$ versus $|\mathbf{Q}|$ for different energy ranges in the (a) x = 0.62 and (b) x = 0.73 compounds. Two cuts of the low-energy mode are depicted, 1.75 - 3.5 meV (blue) and 3.75 - 5 meV (red), which correspond to the dispersive and flat components respectively. In these compositions there is no clear gap between the dispersive mode and the elastic line. Also shown in figure 5.15 is a cut of the high-energy mode, 5.75 - 8 meV (green). The overall intensity of

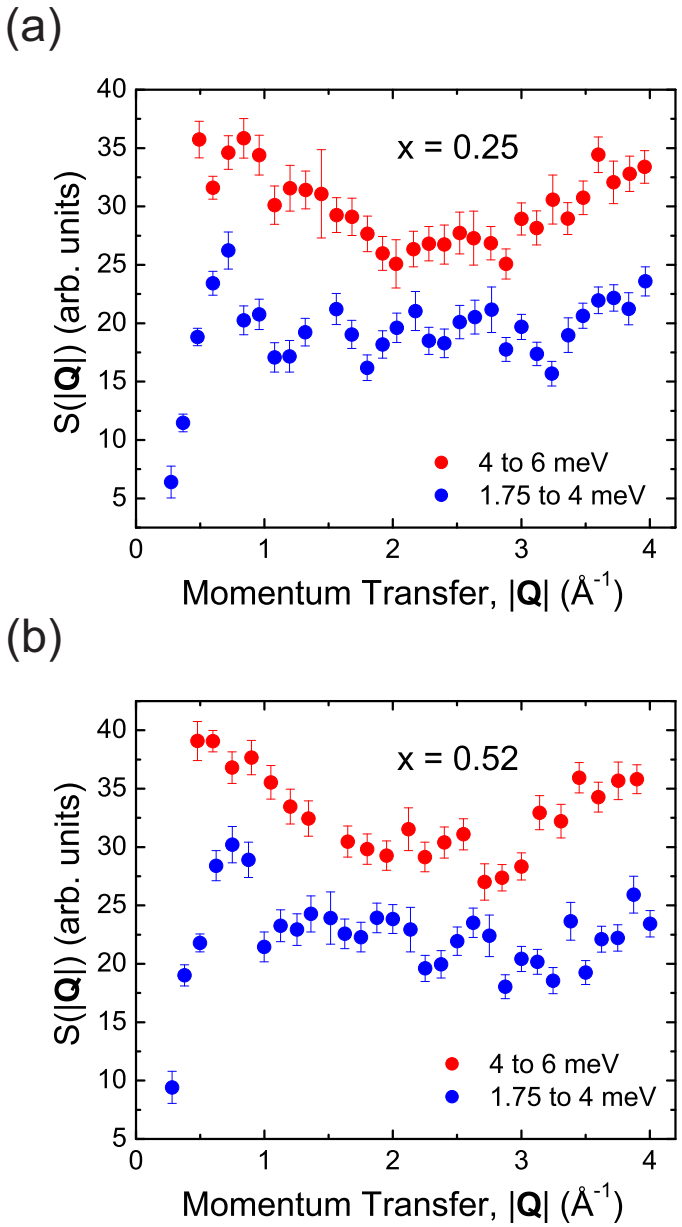

Figure 5.14: $S(|\mathbf{Q}|, \hbar\omega)$ versus $|\mathbf{Q}|$ cuts of the (a) $x = 0.25$ and (b) $x = 0.52$ data over the energy regions 1.75 - 4 meV (blue) and 4 - 6 meV (red).

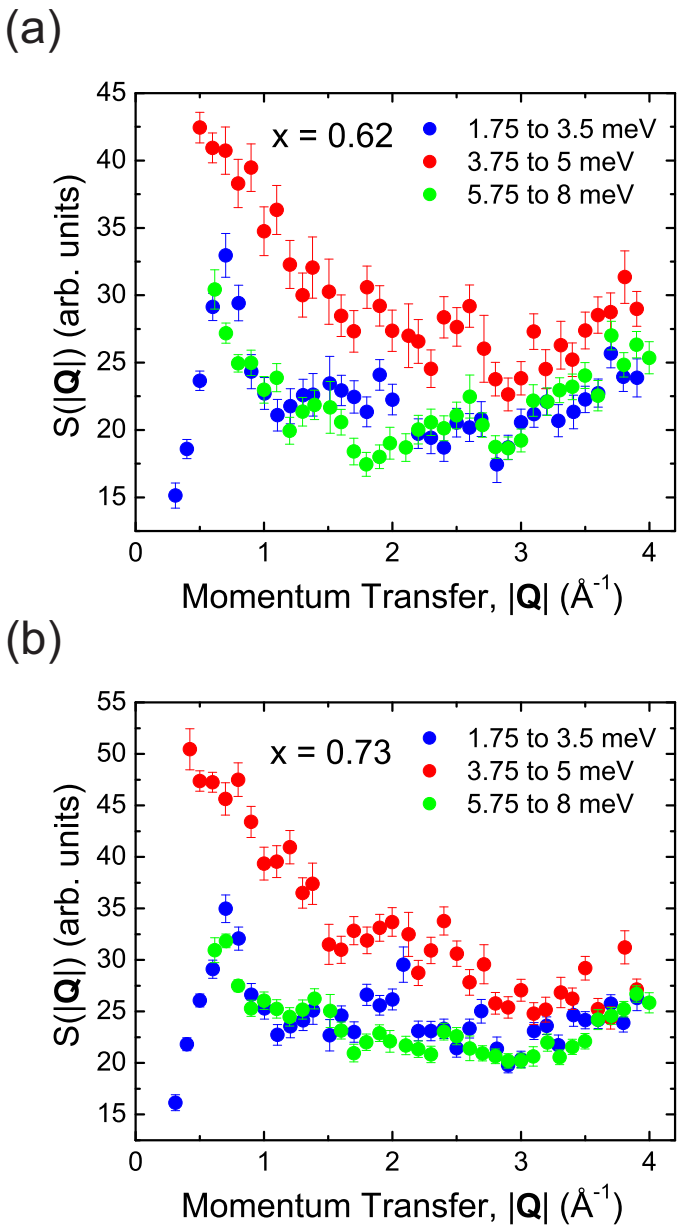

Figure 5.15: $S(|\mathbf{Q}|, \hbar\omega)$ versus $|\mathbf{Q}|$ cuts of the (a) $x = 0.62$ and (b) $x = 0.73$ data over the energy regions 1.75 - 3.5 meV (blue), 3.75 - 5 meV (red) and 5.75 - 8 meV (green).

this mode is much lower than that of the low-energy mode, and at this energy the $|\mathbf{Q}|$ range is more restricted too, making it difficult to determine the nature of the mode. However, the intensity decreases with increasing $|\mathbf{Q}|$ in the region $|\mathbf{Q}| < 3$ Å^{-1}, and the energy dependence is shoulder-like (see figure 5.12), indicating that this is perhaps a flat mode.

In all of the intermediate composition samples there are also two clear peaks in the density of states in the higher $|\mathbf{Q}|$ range (> 3 Å^{-1}) that increase in intensity with increasing $|\mathbf{Q}|$, which are attributed to phonon scattering. $S(|\mathbf{Q}|, \hbar\omega)$ versus $\hbar\omega$ plots are shown for each of the compositions in figure 5.16 ((a) $x = 0.25$, (b) $x = 0.52$) and figure 5.17 ((a) $x = 0.62$, (b) $x = 0.73$). The data cuts have been summed in both high and low regions of $|\mathbf{Q}|$, where the low $|\mathbf{Q}|$ region (approximately 0.5 Å$^{-1} < |\mathbf{Q}| < 1.4$ Å^{-1}) is dominated by the magnetic excitations, and the high $|\mathbf{Q}|$ region (approximately 4 Å$^{-1} < |\mathbf{Q}| < 5$ Å^{-1}) is dominated by vibrational modes. For $x = 0.25$ and 0.52, the magnetic excitation lies at the same energy as the lower peak in the phonon density of states, which joins on almost continuously to a second peak in the phonon density of states centred at about 8 meV. This is similar to the X=Cl magnon-phonon behaviour. However, for $x = 0.62$ and 0.73, the main magnetic excitation moves down in energy, and so the peaks in the density of states of the lattice and magnet excitations no longer reside at the same energy. Also of note, is that the second, higher energy magnetic excitation also does not lie at the same energy as either of the peaks in the phonon density of states.

As previously shown, an approximate phonon subtraction can be made by assuming a purely vibrational contribution to the inelastic scattering detected in the high $|\mathbf{Q}|$ detector bank. Using the DISCUS simulation program [36], the phonon contribution as well as multiple scattering contribution as a function of $|\mathbf{Q}|$ and $\hbar\omega$ has been calculated and subtracted in order to obtain an estimate of the magnetic response. Figure 5.18 shows a corrected $S(|\mathbf{Q}|, \hbar\omega)$ versus $|\mathbf{Q}|$ cut

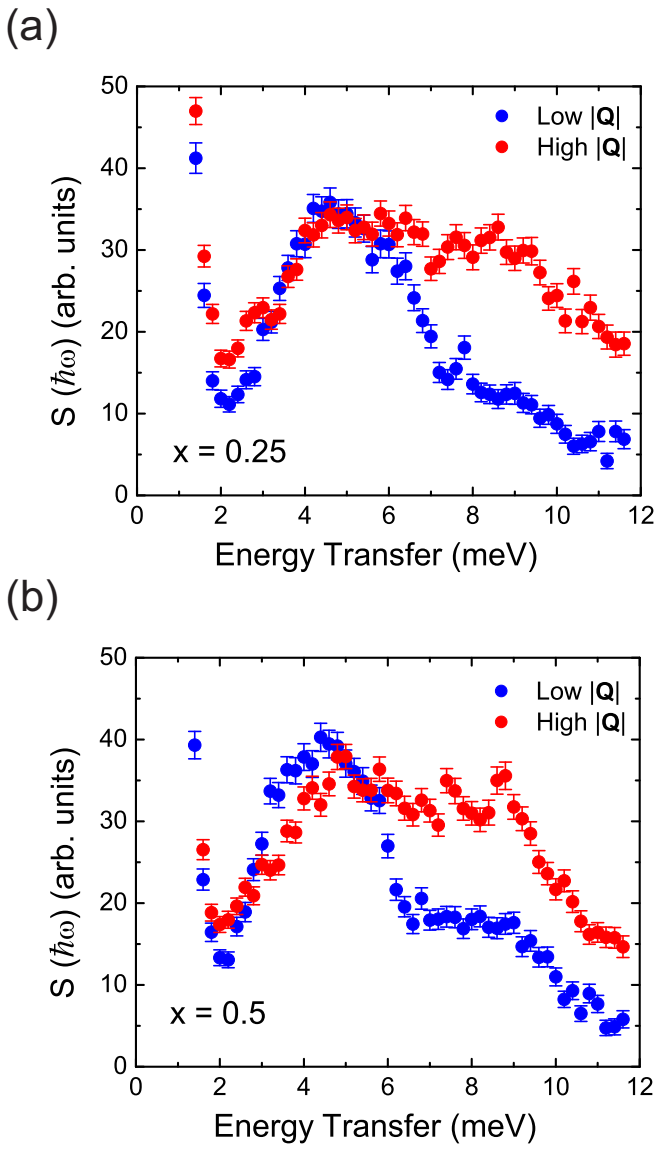

Figure 5.16: $S(|\mathbf{Q}|, \hbar\omega)$ versus $\hbar\omega$ plots are shown for compositions (a) x=0.25 and (b) x=0.52. These have been summed over a low $|\mathbf{Q}|$ region from $\sim$ 0.5 to 1.4 Å^{-1} (blue), and a high $|\mathbf{Q}|$ region from $\sim$ 4 to 5 Å^{-1} (red).

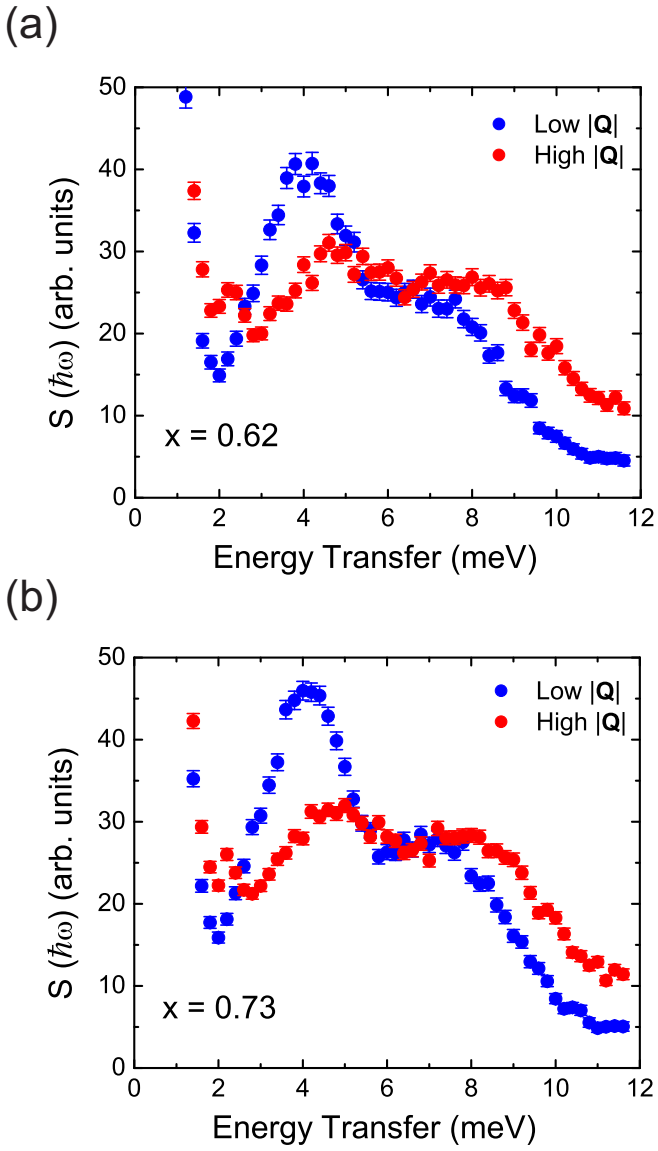

Figure 5.17: $S(|\mathbf{Q}|, \hbar\omega)$ versus $\hbar\omega$ plots are shown for compositions (a) $x = 0.62$ and (b) $x = 0.73$. These have been summed over a low $|\mathbf{Q}|$ region from ~ 0.5 to 1.4 Å^{-1} (blue), and a high $|\mathbf{Q}|$ region from ~ 4 to 5 Å^{-1} (red).

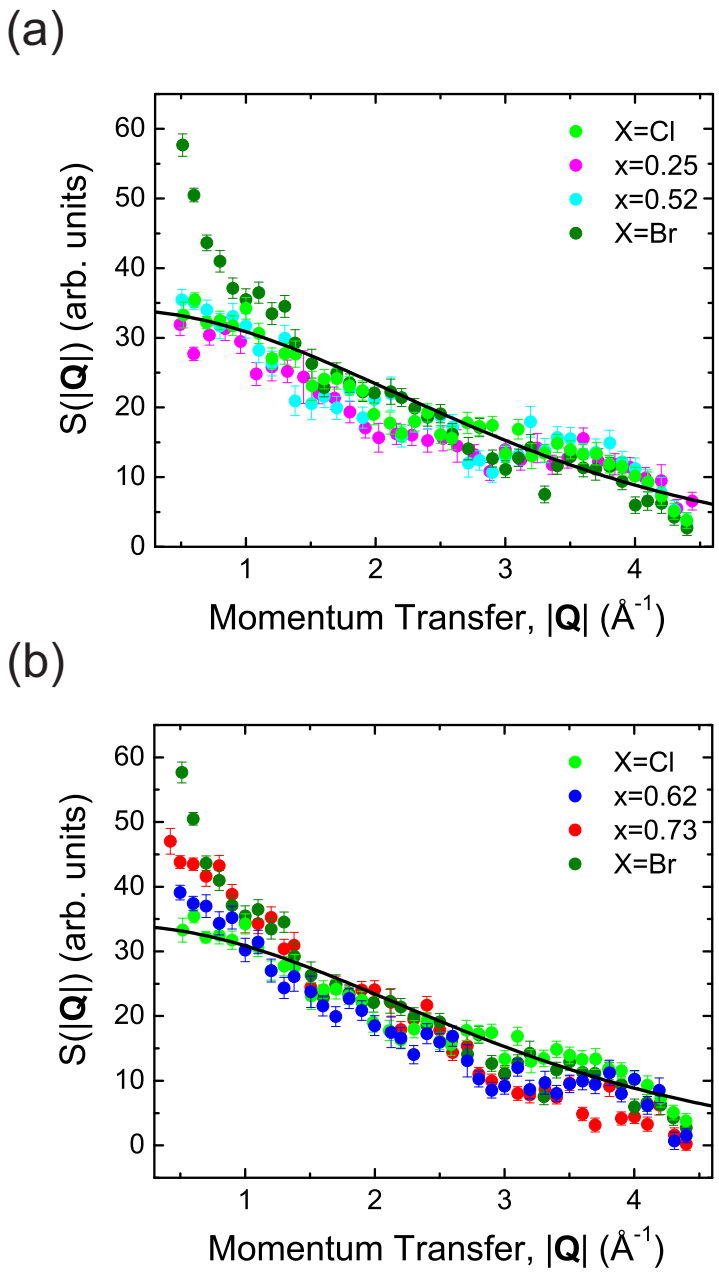

Figure 5.18: $S(|\mathbf{Q}|, \hbar\omega)$ versus $|\mathbf{Q}|$ cut for phonon and multiple scattering corrected data of the (a) $x = 0$, 0.25, 0.52 and 1, and (b) $x = 0$, 0.62, 0.73 and 1 compositions. The solid line is the square of the Cu^{2+} magnetic form factor, which has been normalised to the high $|\mathbf{Q}|$ region ($|\mathbf{Q}| > 3$ Å^{-1}) of the data.

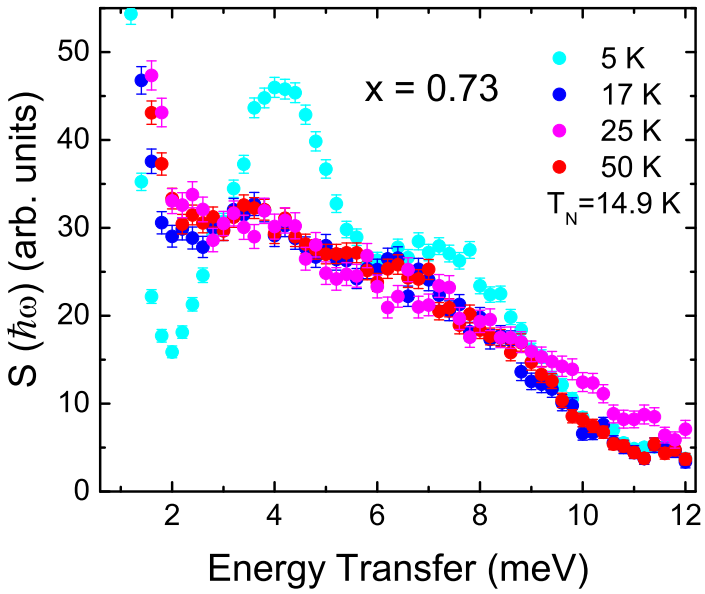

Figure 5.19: $S(|\mathbf{Q}|, \hbar\omega)$ versus $\hbar\omega$ at 5 K (cyan), 17 K (blue), 25 K (magenta) and 50 K (red), for composition $x = 0.73$. The data has been summed over the low $|\mathbf{Q}|$ region (approximately 0.5 Å^{-1} $< |\mathbf{Q}| <$ 1.4 Å^{-1}).

for the (a) $x = 0$, 0.25, 0.52 and 1, and (b) $x = 0$, 0.62, 0.73 and 1 compositions respectively. The square of the Cu^{2+} magnetic form factor [9] is also displayed (solid line), which has been normalised to the high $|\mathbf{Q}|$ region ($|\mathbf{Q}| >$ 3 Å^{-1}) of the data. The $x = 0.25$ and 0.52 compositions show a similar $|\mathbf{Q}|$-dependence to the X=Cl, which follows reasonably closely the square of the Cu^{2+} form factor. However, the $x = 0.62$ and 0.73 compositions are similar to the X=Br compound, in that at low $|\mathbf{Q}|$ ($<$ 1 Å^{-1}) the scattering intensity increases rather more than expected from the square of the single-ion Cu^{2+} form factor alone, particularly in the composition $x = 0.73$.

Results of the temperature dependence of the $x = 0.5$, 0.62, 0.73 samples will now be presented. Figures 5.19, 5.20 and 5.21 show $S(|\mathbf{Q}|, \hbar\omega)$ versus $\hbar\omega$ at 5 K (cyan), 17 K (blue), 25 K (magneta) and 50 K (red), for the $x = 0.73$, 0.62 and 0.52 compositions respectively. The data has been summed over the low $|\mathbf{Q}|$ region (0.5 Å^{-1} $< |\mathbf{Q}| <$ 1.4 Å^{-1}) and is not corrected for phonon and multiple scattering,

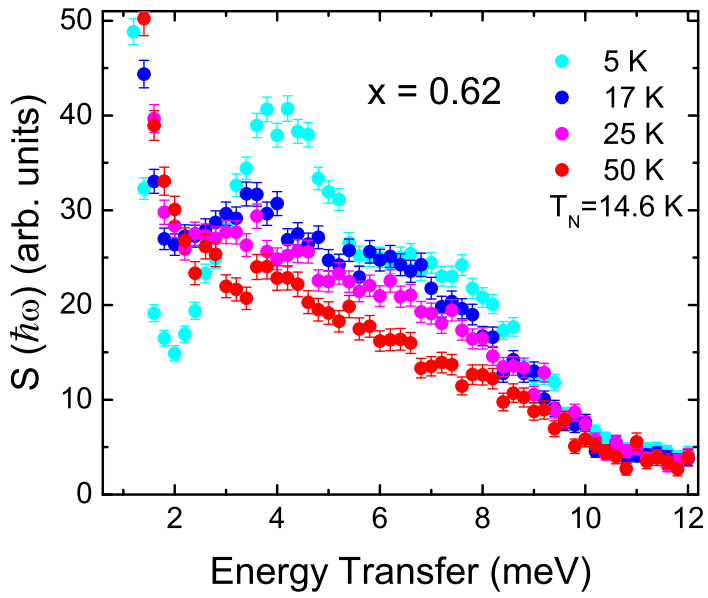

Figure 5.20: $S(|\mathbf{Q}|, \hbar\omega)$ versus $\hbar\omega$ at 5 K (cyan), 17 K (blue), 25 K (magneta) and 50 K (red), for composition $x = 0.62$. The data has been summed over the low $|\mathbf{Q}|$ region (approximately 0.5 Å^{-1} $< |\mathbf{Q}| <$ 1.4 Å^{-1}).

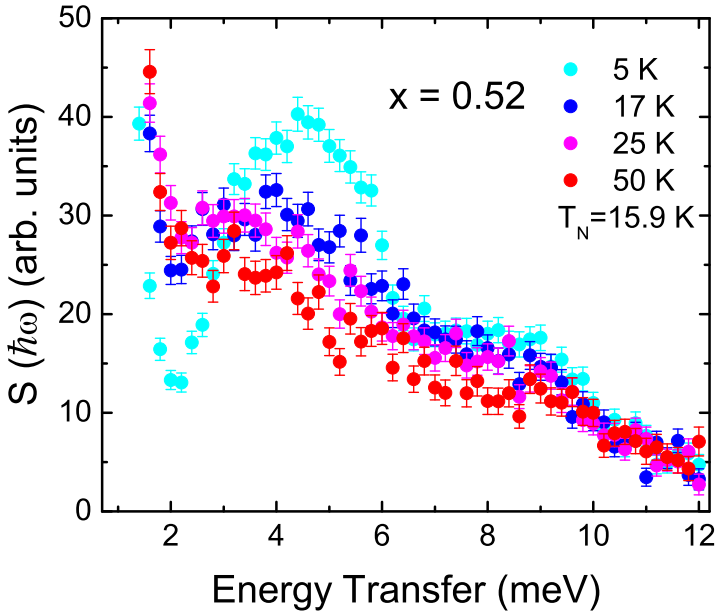

Figure 5.21: $S(|\mathbf{Q}|, \hbar\omega)$ versus $\hbar\omega$ at 5 K (cyan), 17 K (blue), 25 K (magneta) and 50 K (red), for composition $x = 0.52$. The data has been summed over the low $|\mathbf{Q}|$ region (approximately 0.5 Å^{-1} $< |\mathbf{Q}| <$ 1.4 Å^{-1}).

which only has a small contribution in this low $|\mathbf{Q}|$ region. All three doped samples show a very similar temperature dependence. The excitations observed at 5 K have been discussed in detail above. At 17 K, all of the compounds are just above their respective transition temperatures ($T_N^{x=0.73}$, $T_N^{x=0.62} \sim$ 15 K, $T_N^{x=0.52} \sim$ 16 K). Here, the clearly defined inelastic response of the low-temperature phase abruptly falls in intensity, with a shift of the centre of mass of the scattering to lower energies and a quasi elastic response. With increasing temperature the integrated intensity of the quasi-elastic scattering reduces slightly, and any remnant intensity in the low-temperature inelastic peaks disappears completely by 50 K. This is very much like the temperature dependence observed in the X=Cl compound, in which, above the transition temperature (T_N^{Cl} =18.2 K), the inelastic structure is replaced by a quasi elastic lineshape from a diffusive response. In none of the samples is there evidence of the temperature dependence observed in the case of the bromide, in which the inelastic response at low temperatures is maintained, with smoothly decreasing intensity, at temperatures well above the transition temperature.

5.3.2 Discussion

Firstly, the Cl end of the intermediate compositions, that is the compositions $x =$ 0.25 and 0.52, will be discussed. Doping of up to 50 % Br for Cl does not seem to have a very large effect on the inelastic scattering, with the $x = 0.25$ and $x = 0.52$ results similar in many ways to those of the X=Cl compound. The main effect of the doping seems to be the slight lowering of the excitation energy with respect to the chloride, and the small accentuation of a shoulder-like feature at the high energy ($\sim$ 8 meV) side. In the isolated tetrahedral model with nearest neighbour interaction J_1 and next nearest neighbour interaction J_2, a distortion of the tetrahedra (such that $J_1 \neq J_2$) can lift the degeneracy of the ground state singlets and the excited triplets, such that additional excitations become available. Referring to figure 1.11, whilst the main peak in the data at $\sim$ 5 meV

may correspond to the $E_{s1} \rightarrow E_{t1}$ transition of magnitude J_1, a second peak at $\sim$ 8 meV may correspond to an $E_{s1} \rightarrow E_{t2}$ transition with magnitude $2J_1 - J_2$. This would set $J_1 \sim$ 58 K and $J_2 \sim$ 23 K, which gives a fairly small ratio of the two exchange parameters, and would also imply that the second singlet state, E_{s1}, lies above the triplet state, E_{t2}. Indeed, Whangbo et al. support the idea that J_2 is much smaller than J_1 due to the fact that the J_2 interaction is a super-super exchange interaction via two O atoms (Cu-O··O-Cu), in which the overlap of the magnetic orbitals is practically zero [78].

However, the isolated tetrahedral model would still not produce dispersionless excitations. The presence of inter-tetrahedral couplings allows for dispersive modes and also produces a splitting of the energy states of the isolated tetrahedral model, thereby allowing several excitation modes, and the presence of multiple peaks. Like in the X=Cl compound, the main peak in the $x = 0.25$ and 0.52 compositions at $\sim$ 5 meV has both a flat and a dispersive component. The data indicates that there is a gap between the elastic line and the dispersive component at about 2 meV, which, as with the chloride, indicates anisotropy of the underlying magnetism. As with the chloride, it is not clear from this data whether the flat component arises from the flat part of the dispersive excitation at the BZ boundary, or a separate dispersionless excitation. The flat mode in both samples shows a similar $|\mathbf{Q}|$ dependence to X=Cl once corrections have been made, falling in intensity with increasing $|\mathbf{Q}|$ as the square of the Cu^{2+} form factor. This suggests that the underlying scattering exchange interactions, and therefore scattering units, are the same for each of the compositions $x = 0$, 0.25 and 0.52.

On the matter of spin-lattice coupling, the $x = 0.25$ and 0.52 compositions also have magnetic and phonon modes lying at the same energy as each other, as was the case for the chloride compound. Once again, however, little information about the spin-lattice coupling can be extracted from this data.

Finally, the temperature dependence of the $x = 0.25$ and 0.52 samples is

also very chloride-like, with the same abrupt change from a structured inelastic response below the transition temperature, to a diffusive response above it. This indicates that the nature of the transition observed in these three compounds is similar, as also indicated by heat capacity measurements (see section 3.3) in which the field dependence of the transition is the same for all of them.

Whilst little alters in the inelastic scattering when doping from the X=Cl compound up to the composition $x = 0.52$, a more distinct change is observed in the doping range $x \sim 0.6$ - 0.7. The results observed for the compositions $x = 0.62$ and 0.73 will now be discussed. The major difference observed in these compounds in comparison with the other compositions, is the double-peaked energy spectra with clear modes at 4 and 7 meV. It is unclear whether the 7 meV excitation corresponds to a large increase in the intensity of the shoulder-like feature observed in the compositions $x = 0$, 0.25 and 0.52 as discussed above, or whether it is a completely new mode. In the independent tetrahedra model this would correspond to the lowering of the exchange interactions to $J_1 = 46$ K and $J_2 = 12$ K, and a large increase in the weight of the relative scattering of the $E_{s1} \rightarrow E_{t2}$ excitation compared to the other compositions. However, inter-tetrahedral coupling is required in order to allow dispersive excitations, which are still clearly observed in the lower energy mode. Indeed, the dispersive character of the excitation in the energy region 1.75 to 3.5 meV is similar to the dispersive mode observed in the X=Br compound, with possibly gapless spin waves emerging from the magnetic Bragg peaks. Moreover, the $|\mathbf{Q}|$-dependence of the flat component also shows similarity to the X=Br compound, in that the intensity increases to rather larger values at low $|\mathbf{Q}|$ than expected from the square of the single-ion form factor. The $|\mathbf{Q}|$-dependence arising from the structure factor of an inter-tetrahedral exchange configuration would be a superposition of $|\mathbf{Q}|$-dependent oscillations about the single-ion form factor that would be most dominant at low $|\mathbf{Q}|$ and dampen with increasing $|\mathbf{Q}|$. The increase in the low $|\mathbf{Q}|$ intensity from $x = 0.62$ to $x = 0.73$ to

$x = 1$ suggests that the underlying exchange interactions are altering in this region, and that exchange interactions on an inter-tetrahedral length scale play a role in each of these compositions. This may agree with the work of Whangbo et al., who believe that the inter-tetrahedral interactions are dominant in the bromide, whereas the intra-tetrahedral J_1 interaction is still significant in the chloride [78].

As with the X=Br compound, it is unclear whether the flat component at $\sim$ 4 meV in the $x = 0.62$ and 0.73 samples is a separate dispersionless excitation, or arises from the flat part of the dispersive excitation at the BZ boundary. Indeed, the mode at 7 meV also appears to be a flat mode, although is is difficult to tell for certain due to the restricted $|\mathbf{Q}|$ range and low statistics. This could either be a new dispersionless excitation, or arise from a second flat part in the dispersion relation that would give rise to a second peak in the density of states. Alternatively, the 7 meV mode could correspond to the 5 meV flat component of the X=Br compound, which has shifted up in energy, leaving the dispersive mode whose flat part at the BZ boundary is still visible as a reduced flat component at 4 meV. This speculation cannot be clarified with polycrystalline measurements, but requires the greater insight of single crystal inelastic scattering measurements.

Whilst the $x = 0.62$ and 0.73 compositions show some similarities with the X=Br compound, and also some stark differences to both end compounds, the temperature dependence is very much X=Cl-like. All of the intermediate composition samples show an abrupt shift from a well-defined inelastic response below their respective transition temperatures, to a quasi-elastic response above. This suggests that the nature of the transition is similar in all compositions measured, except in the pure bromide, which shows a very different temperature dependence. This compares well with the heat capacity data shown in section 3.3, in which the field dependence of the transition follows the same pattern for all of the compositions except in the bromide, which acts in the opposite sense. This indicates that some significant change in the underlying interactions occurs between the

pure bromide and a doping of $\sim$ 27 % Cl for Br. Raman scattering results [45] and calculations [35] support this. A low energy mode ($\sim$ 2 meV) observed in Raman scattering of the pure bromide splits into two modes when Cl is doped in to the system, and these shift to higher energy with decreasing x. By $x \sim 0.7$ the Raman spectrum is essentially the same as that of the chloride. Whilst the modes described are not directly identifiable with the excitations observed in these NIS measurements, it does reflect considerable change of the system's characteristics in the same compositional range.

A possible explanation for the results observed is that doping with Cl rapidly suppresses the ability of the system to build up strong correlations and/or low dimensional order well above the transition temperature. This could be the result of introducing disorder, or could arise from the fragility of almost degenerate exchange configurations, which can be fine tuned with small amounts of doping. In a low dimensional system, a maximum in the magnetic susceptibility can give a good indication of the underlying strength of the magnetic interactions, more so perhaps than the actual transition temperature, which can reflect weaker 'parasitic' interactions that finally lock in the three dimensional order (examples of this are copper oxy-chlorides $CaGdCuO_3Cl$ and $Ca_4R_2Cu_3O_8Cl_4$ (R=Gd,Sm) [72]). In magnetic susceptibility measurements of $Cu_2Te_2O_5(Br_xCl_{1-x})_2$ (see section 3.2), the maximum in the susceptibility is at a slightly higher temperature in the bromide than the chloride (29 K and 23 K respectively), consistent with stronger exchange, as might be expected from the discussion above. However, in the mixed compositions the temperature of the susceptibility maxima reduces with respect to both the bromide and chloride, suggesting that disorder has the effect of reducing the overall coupling strength of the magnetic interactions. Nevertheless, on increasing the composition from $x = 0.25$ to $x = 0.73$, the temperature of the susceptibility maximum increases steadily, indicating that indeed the interactions become stronger when more concentrated with Br atoms. There is a very large

increase from $x = 0.73$ to $x = 1$ ($\sim 35\%$) in the underlying coupling strength based on this argument, which is in line with the NIS results presented here that show an abrupt change in the dynamics in this compositional range. To this end, a doping induced transition in the underlying magnetic exchange configuration appears to take place between $x = 0.73$ and 1, which supports the argument already proposed that the X=Br and Cl compounds lie either side of a quantum critical point [46, 27]. Clearly it would be beneficial to extend this study to the region of compositions between $x = 1$ and 0.73 in order to probe the question of quantum criticality further.

5.4 Chapter summary

Magnetic excitations with a dispersive component have been directly observed in neutron inelastic scattering (NIS) measurements of the spin tetrahedral $Cu_2Te_2O_5X_2$ (X=Br,Cl) materials. The chloride supports an excitation spectrum which softens toward the ordering temperature, whilst the bromide shows a rather different temperature dependence indicating the possibility of low dimensional and/or short range correlations above T_N^{Br}. The results presented show that there are clearly large differences in the dynamic behaviour of these two compounds, despite the similarity of their static magnetic order below $T_N^{Br,Cl}$. In intermediate compositions with low Br content, $Cu_2Te_2O_5(Br_xCl_{1-x})_2$ with $x = 0.25$ and 0.52, the samples maintain the chloride characteristics. However, for the compositions $x = 0.62$ and 0.73, an additional excitation appears and the excitation spectrum is rather different from either X=Br or Cl. Nevertheless, all of the intermediate compositions show a temperature dependence similar to the chloride, indicating that the type of transition observed in the X=Br is confined to a small region of the compositional range ($x > 0.73$). Further NIS measurements of samples with composition $0.73 < x < 1$ would be highly beneficial in furthering the understanding of the

development of the dynamics with composition. Moreover, the availability of large single crystal mosaics would allow clearer measurements of the dispersive magnetic excitations to be performed.

Chapter 6

The Effect of Pressure on the Magnetic Behaviour of $Cu_2Te_2O_5(Br_xCl_{1-x})_2$

6.1 Introduction and experimental details

The previous two chapters have focused on the structural and dynamic magnetic behaviour of $Cu_2Te_2O_5(Br_xCl_{1-x})_2$ respectively. Whilst the underlying magnetic structures of $Cu_2Te_2O_5Br_2$ and $Cu_2Te_2O_5Cl_2$ are found to be similar, there are a number of differences between their dynamic behaviour. In both cases the progression of the behaviour between the two compounds was investigated by systematic substitution of Cl for Br. This doping, which can be thought of as applying chemical pressure, alters the relative bond lengths and unit cell volume of the compound, affecting the relative strength of the underlying exchange interactions. Similarly, the application of an external pressure may be used to alter interatomic dimensions within the compound, thereby probing the underlying exchange interactions. External pressure can be applied in a systematic way as a single controllable parameter. External pressure has been used as a tool to tune the underlying interactions

in many magnetically ordered systems, and has proved to be an invaluable tool for investigating quantum critical points (see, for example, references [52, 59, 60]). In this chapter, the effect of externally applied pressure on the magnetic behaviour of $Cu_2Te_2O_5(Br_xCl_{1-x})_2$ is investigated.

In section 6.2.1, results showing the effect of applied pressure on the magnetic susceptibility of polycrystalline samples of $Cu_2Te_2O_5(Br_xCl_{1-x})_2$ for $x = 0$, 0.73 and 1, are presented. Details of the sample growth and characterisation can be found in chapter 3. Subsequently, section 6.2.2 presents results from a neutron diffraction study of single crystal $Cu_2Te_2O_5Cl_2$ under applied pressure on the D10 four-circle diffractometer, ILL (see section 2.3.3 for instrumental details). The single crystal was grown by H. Berger using a halogen vapour transport technique [80]. Section 6.3 presents details of a study of the dynamic magnetic behaviour of polycrystalline $Cu_2Te_2O_5Br_2$ under applied pressure by inelastic neutron scattering on the direct geometry spectrometer HET at ISIS. Again, the sample growth and characterisation details are presented in chapter 3, and instrumentation details are given in section 2.3.5.

6.2 The effect of externally applied pressure on the magnetic transition in $Cu_2Te_2O_5(Br_xCl_{1-x})_2$

6.2.1 Susceptibility measurements of $Cu_2Te_2O_5(Br_xCl_{1-x})_2$ under pressure

Previous magnetic susceptibility measurements of polycrystalline $Cu_2Te_2O_5Br_2$ under applied pressure have been reported by Kreitlow et al. [43]. In ambient pressure measurements $Cu_2Te_2O_5Br_2$ shows a maxima in the susceptibility (χ) at $T_{max} \sim 25$ K, and a feature in $d\chi/dT$ at $T_N^{Br} = 11.6$ K, which corresponds to the magnetic transition temperature. The authors track both of these features as a function of

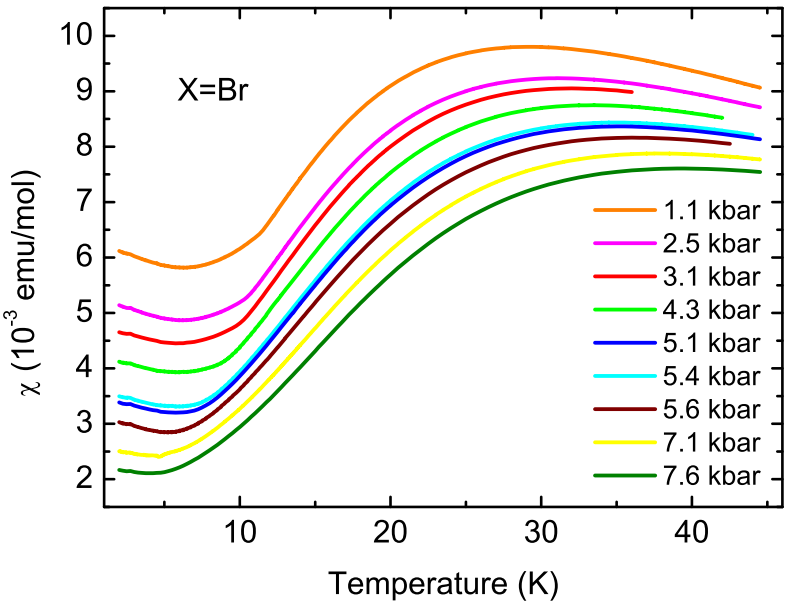

Figure 6.1: Magnetic susceptibility (χ) versus temperature for $Cu_2Te_2O_5Br_2$ in several externally applied pressures. The measurements were performed in an applied magnetic field of 50 kOe.

pressure, with applied pressures of 0.1 kbar, 1.5 kbar, 3.5 kbar and 8.2 kbar. They observe that T_{max} increases with increasing applied pressure, by up to 25 % under 8.2 kbar, which they associate with an increase in the overall magnetic coupling strength. However, they find that T_N^{Br} quickly decreases under pressure and the feature in χ associated with the transition is no longer observable at 8.2 kbar, indicating that $Cu_2Te_2O_5Br_2$ lies close to a non-magnetic phase. In this chapter, a more detailed study of the susceptibility of $Cu_2Te_2O_5Br_2$ under applied pressure is presented, along with similar measurements of $Cu_2Te_2O_5Cl_2$ and the mixed composition sample $Cu_2Te_2O_5(Br_xCl_{1-x})_2$, $x = 0.73$.

Susceptibility measurements as a function of temperature were performed on a Quantum Design SQUID magnetometer (see section 2.1.1 for instrumental details). External pressure was applied using an easyLab Technologies Mcell 10 pressure cell, using Sn as an *in situ* manometer (see section 2.2). Figure 6.1 shows the susceptibility (χ) of $Cu_2Te_2O_5Br_2$ in an applied magnetic field of 50 kOe as

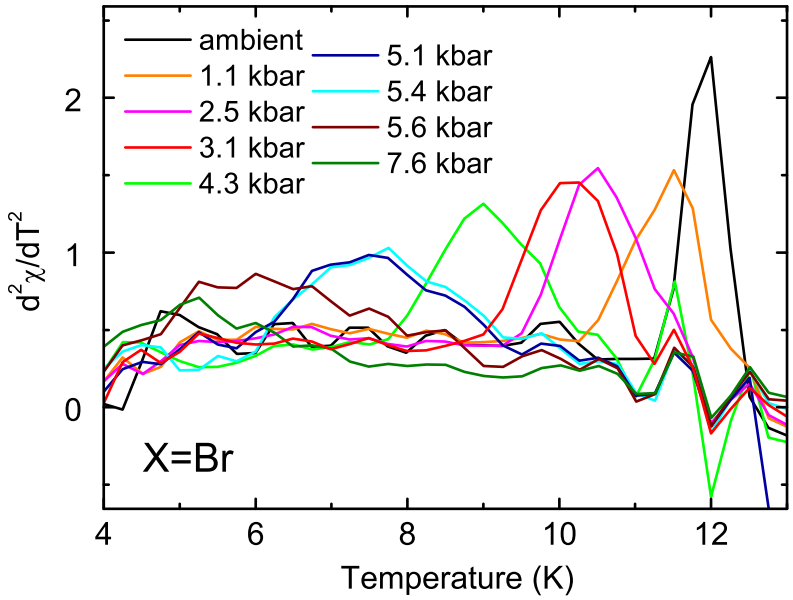

Figure 6.2: The second derivative of the magnetic susceptibility ($d^2\chi/dT^2$) as a function of temperature for $Cu_2Te_2O_5Br_2$ under a number of externally applied pressures.

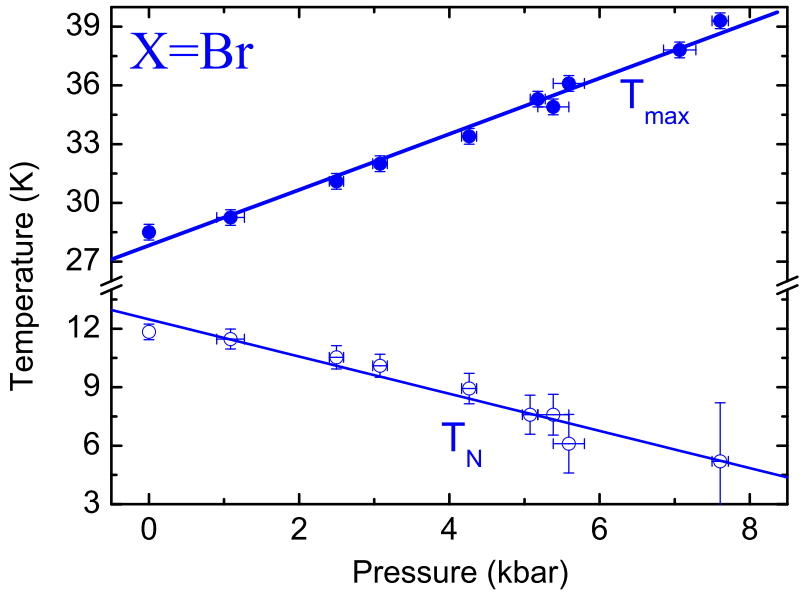

Figure 6.3: The transition temperature, T_N^{Br}, and the temperature of the maxima in the susceptibility T_{max} of $Cu_2Te_2O_5Br_2$ as a function of pressure.

a function of temperature in a number of different applied pressures. Three main features of this data should be highlighted. Firstly, the overall magnitude of the susceptibility decreases systematically as the pressure is increased, with the low temperature minima falling from $\sim$ 6 x 10^{-3} emu/mol in 1.1 kbar, to $\sim$ 2 x 10^{-3} emu/mol in 7.6 kbar. Secondly, the temperature at which the maxima in the susceptibility occurs shifts linearly to higher temperatures with increasing pressure, from $\sim$ 29 K in 1.1 kbar, to $\sim$ 39 K in 7.6 kbar. These observed points are both in good agreement with the work of Kreitlow et al. [43]. Finally, the transition temperature, T_N^{Br}, is observed to decrease in temperature with applied pressure. The transition temperature is seen much more clearly in the double derivative of the data ($d^2\chi/dT^2$), which is displayed in figure 6.2. Here, the transition temperature (corresponding to the maxima in the peak of $d^2\chi/dT^2$) is seen to decrease linearly in applied pressure, from $\sim$ 11.5 K in 1.1 kbar, to $\sim$ 6.1 K in 5.6 kbar. The peak width increases significantly with increasing applied pressure. By 7.6 kbar there is no longer a clearly defined peak that can be associated with the magnetic transition, although there is a small, broad peak centred at $\sim$ 5 K. Unfortunately, below $\sim$ 4 K, $d^2\chi/dT^2$ becomes rather noisy. This is believed to be because of problems with the background subtraction at low temperatures where the sample susceptibility is very low, and the signal from the pressure cell becomes large due to the presence of paramagnetic impurities in the cell. It is therefore difficult to ascertain whether or not the ordering temperature is suppressed toward $T = 0$ K by further increasing the applied pressure. Figure 6.3 summarises the susceptibility data by plotting both T_N^{Br} and T_{max} as a function of pressure. Linear fits give gradients of -0.95(9) K/kbar and 1.42(6) K/kbar for T_N^{Br} and T_{max} respectively. The pressure dependence of T_N^{Br} observed in this data differs somewhat from the results reported by Kreitlow et al. [43]. In their work, they report that $T_N^{Br} \sim 5$ K in 3.5 kbar and as a consequence the pressure dependence is rather non-linear. The authors suggest, however, that the peak observed at 5 K in 3.5 kbar may be

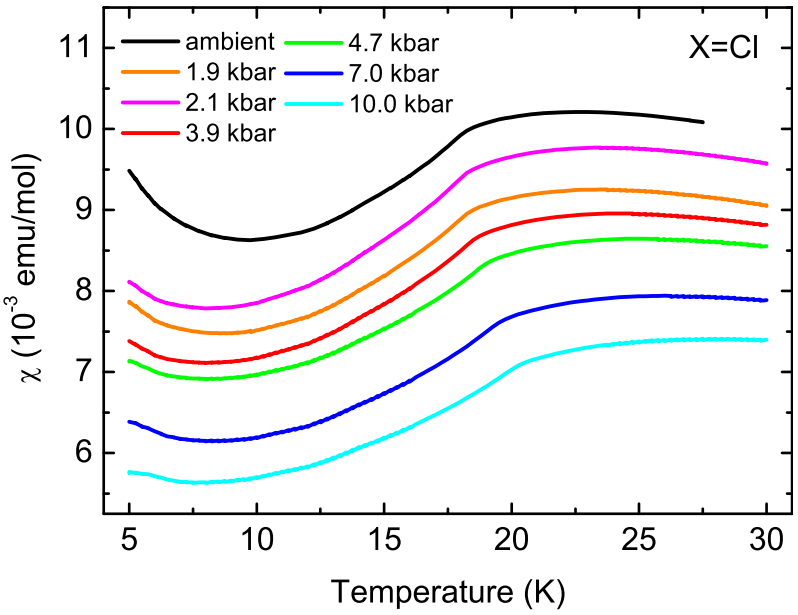

Figure 6.4: Magnetic susceptibility (χ) versus temperature for $Cu_2Te_2O_5Cl_2$ in several externally applied pressures. The measurements were performed in an applied magnetic field of 1 kOe.

an instrumental artefact, which is supported by the results presented in this thesis for which $T_N^{Br} \sim 10.1$ K at 3.1 kbar (and 8.9 K at 4.3 kbar), and for which no feature is observed at 5 K in this pressure range. Moreover, the large number of pressures measured in the work of this thesis have allowed the observation of a more consistent, linear pressure dependence.

Figure 6.4 shows the susceptibility of polycrystalline $Cu_2Te_2O_5Cl_2$ as a function of temperature under various externally applied pressures. This data was taken in an applied field of 1 kOe. Again, the overall magnitude of the susceptibility decreases systematically with increasing pressure (with the exception of the 1.9 kbar data), with the low temperature minima falling from $\sim$ 8.5 x 10^{-3} emu/mol in ambient pressure, to $\sim$ 5.5 x 10^{-3} emu/mol in 10.0 kbar. The maxima in the susceptibility is also seen to increase with applied pressure, from $\sim$ 23 K in ambient pressure to $\sim$ 28 K in 10.0 kbar. Figure 6.5 plots $d^2\chi/dT^2$ as a function of temperature for each of the different pressures. The minima in $d^2\chi/dT^2$ cor-

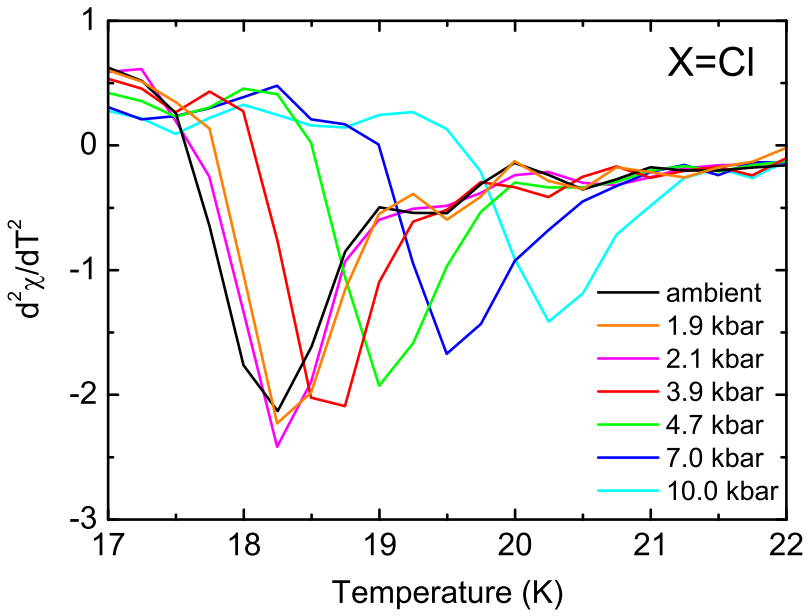

Figure 6.5: The second derivative of the magnetic susceptibility ($d^2\chi/dT^2$) as a function of temperature for $Cu_2Te_2O_5Cl_2$ under different externally applied pressures.

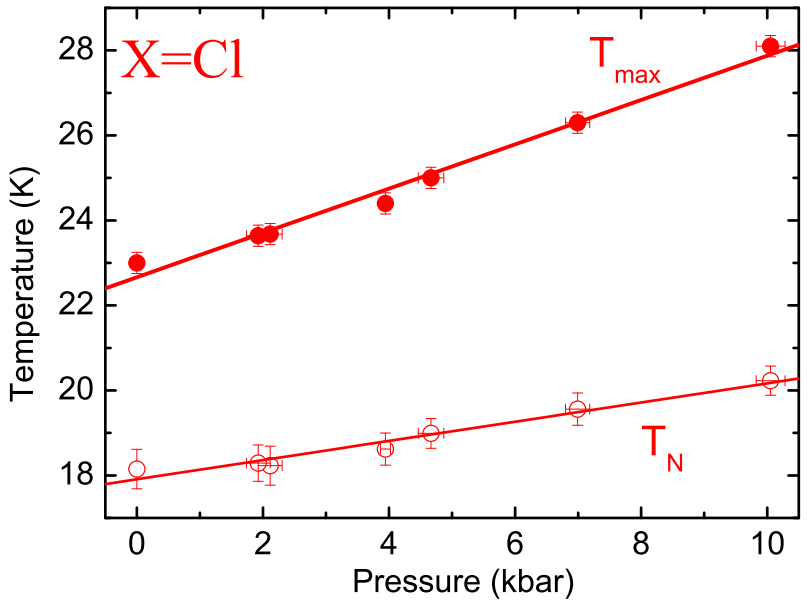

Figure 6.6: The transition temperature, T_N^{Cl}, and the temperature of the maxima in the susceptibility T_{max} of $Cu_2Te_2O_5Cl_2$ as a function of pressure.

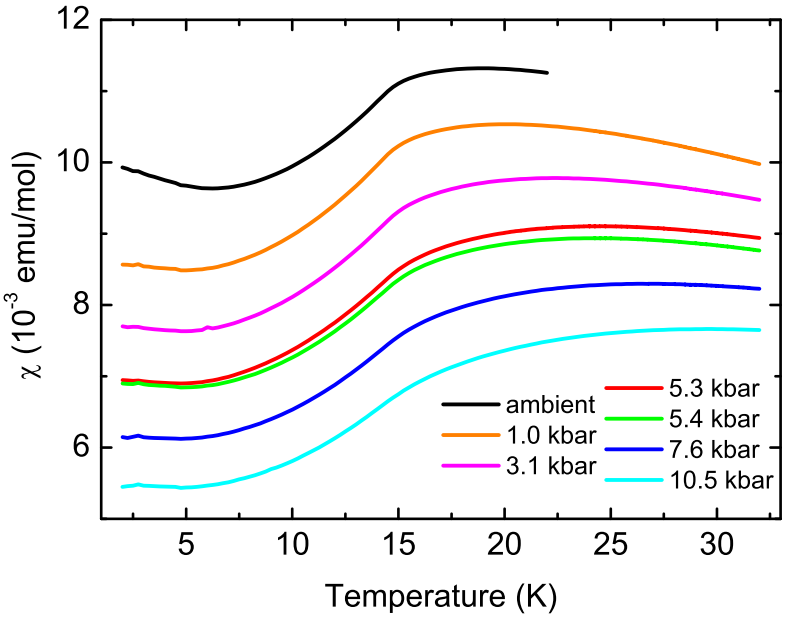

Figure 6.7: Magnetic susceptibility (χ) versus temperature in different externally applied pressures for $Cu_2Te_2O_5(Br_xCl_{1-x})_2$ with $x = 0.73$. The measurements were performed in an applied magnetic field of 1 kOe.

responds to the transition temperature, T_N^{Cl}, which is observed to increase in a linear fashion with increasing pressure. Figure 6.6 shows the pressure dependence of both T_N^{Cl} and T_{max}, with linear fits giving gradients of 0.23(2) K/kbar and 0.52(3) K/kbar for T_N^{Cl} and T_{max} respectively. Neither the transition temperature nor T_{max} respond as strongly to pressure as they do in the case of $Cu_2Te_2O_5Br_2$. T_{max} is almost three times as responsive to pressure in the case of X=Br than X=Cl. T_N is almost four times as responsive to pressure for X=Br compared to X=Cl, and, moreover, the pressure dependence acts in the opposite sense for the two compounds. Whilst for the bromide T_N *decreases* with increasing pressure, for the chloride T_N *increases* with increasing pressure, indicating that pressure has a significantly different effect on these two compounds.

The susceptibility of $Cu_2Te_2O_5(Br_xCl_{1-x})_2$ with $x = 0.73$ is displayed in figure 6.7 as a function of temperature for several externally applied pressures. The data was collected in an applied field of 50 kOe. As was the case for

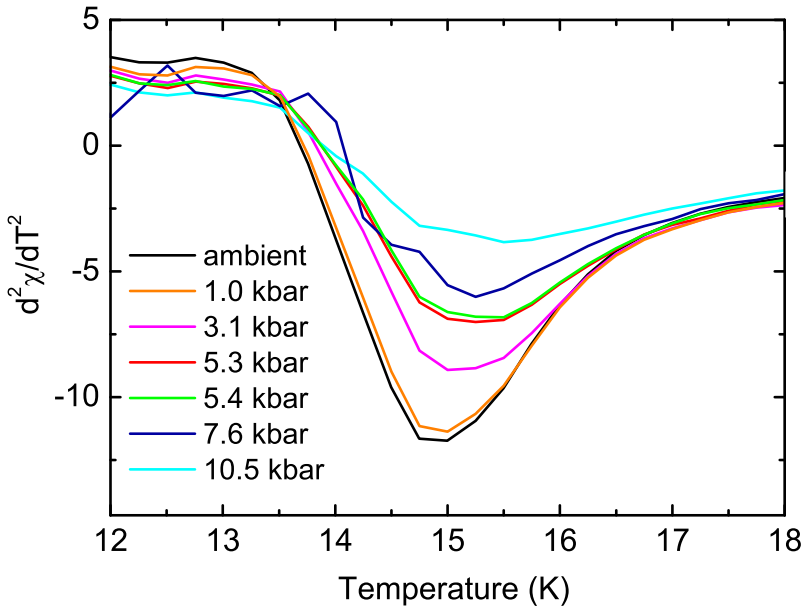

Figure 6.8: The second derivative of the magnetic susceptibility ($d^2\chi/dT^2$) as a function of temperature for $Cu_2Te_2O_5(Br_xCl_{1-x})_2$ with $x = 0.73$, for different externally applied pressures.

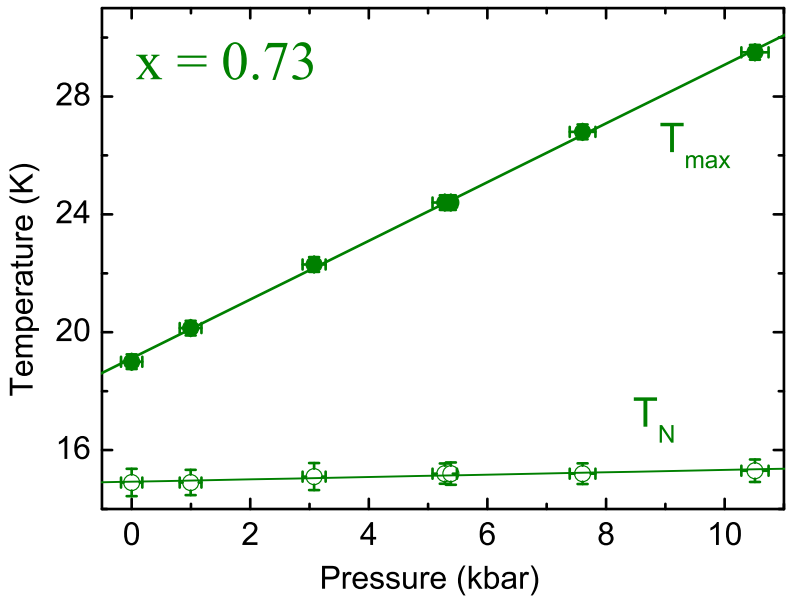

Figure 6.9: The transition temperature ($T_N^{x=0.73}$) and the temperature of the maxima in the susceptibility (T_{max}) of $Cu_2Te_2O_5(Br_xCl_{1-x})_2$ with $x = 0.73$ as a function of pressure.

$Cu_2Te_2O_5X_2$ (X=Br,Cl), the magnitude of the susceptibility falls with increasing pressure, from $\sim 10^{-2}$ emu/mol at low temperatures in ambient pressure to $\sim$ 5.5 x 10^{-3} emu/mol in 10.5 kbar. T_{max} increases from 19 K in ambient pressure to 30 K in 10.5 kbar, which corresponds to an increase of $\sim$ 58 %. Figure 6.8 shows $d^2\chi/dT^2$ versus temperature. The minima in $d^2\chi/dT^2$ is found to correspond to the transition temperature ($T_N^{x=0.73}$) by comparing this data with the ambient pressure heat capacity measurements presented in chapter 3, for which the transition temperature in ambient pressure is well-defined. $T_N^{x=0.73}$ barely changes with applied pressure, increasing by less than 1 K from ambient pressure to an applied pressure of 10.5 kbar. Figure 6.9 shows the pressure dependence of $T_N^{x=0.73}$ and T_{max}, both of which show a linear relationship with gradients of 0.04(1) K/kbar and 1.00(1) K/kbar respectively. The rate at which T_{max} increases with applied pressure is therefore approximately half-way between the rates observed for the chloride and bromide. The pressure dependence of $T_N^{x=0.73}$ is closer to that demonstrated for T_N^{Cl} by the chloride than for T_N^{Br} in the bromide, as it increases with increasing pressure. However, the response is reduced in comparison to the chloride, and the $x = 0.73$ sample therefore behaves in an intermediate manner to the two end compounds.

6.2.2 Neutron diffraction study of $Cu_2Te_2O_5Cl_2$ under pressure

The susceptibility measurements described above give an indication of the effect of applied pressure on the magnetic behaviour on a macroscopic level. In order to directly probe the effect of pressure on a microscopic level, neutron diffraction measurements have been performed on single crystal $Cu_2Te_2O_5Cl_2$ on the D10 diffractometer at the ILL. The sample was of dimensions 5 mm x 2.5 mm x 2.0 mm, and was grown by H. Berger [80]. Hydrostatic pressure was applied to the sample using a CuBe clamp cell with a Fluorinert pressure medium (see section 2.2). In

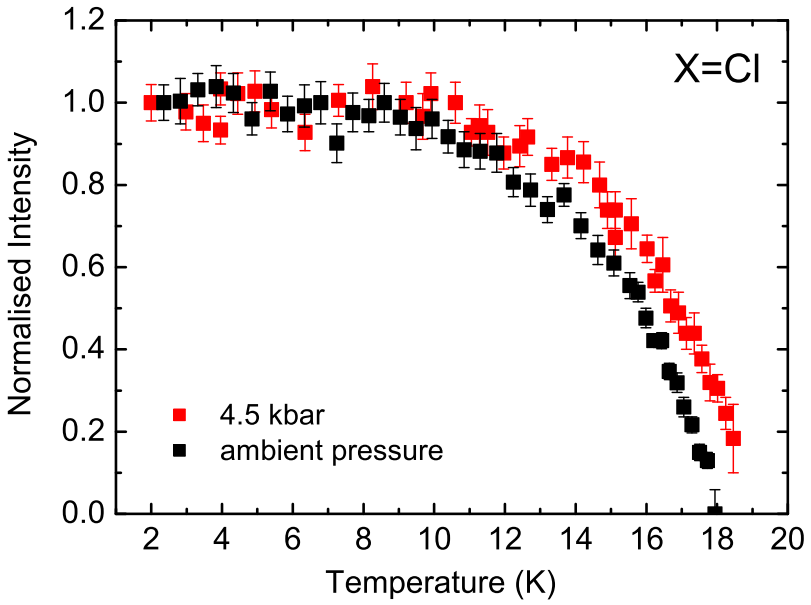

Figure 6.10: Normalised integrated intensity of the $\mathbf{Q} = (0.56\ 0.845\ 0.5)$ reflection as a function of temperature for $Cu_2Te_2O_5Cl_2$. The ambient pressure data is in black and the 4.5 kbar data is in red. This data was collected on D10 at the ILL.

order to measure the pressure *in situ*, a NaCl crystal was placed alongside the sample in the pressure cell, and its lattice parameter was measured at 2 K with the cell under pressure. Making use of the work of Decker [15, 16], in which the equation of state of NaCl is calculated for a range of pressures and temperatures, the pressure applied to the sample was determined to be 4.5(3) kbar.

Firstly, the modulation vector of the incommensurate magnetic structure was not observed to change from that of the ambient pressure structure when under an applied pressure of 4.5 kbar. The intensity of the magnetic reflection $\mathbf{Q} = (0.56\ 0.845\ 0.5)$ was measured as a function of temperature, both in ambient pressure and under 4.5(3) kbar. Figure 6.10 shows the integrated intensity of this reflection over the temperature range 2 - 18.5 K, in which the data taken in ambient pressure and 4.5 kbar have been normalised to the same intensity scale. The data shows a clearly resolved shift in the temperature dependence of the integrated intensity under an applied pressure. The intensity of the magnetic

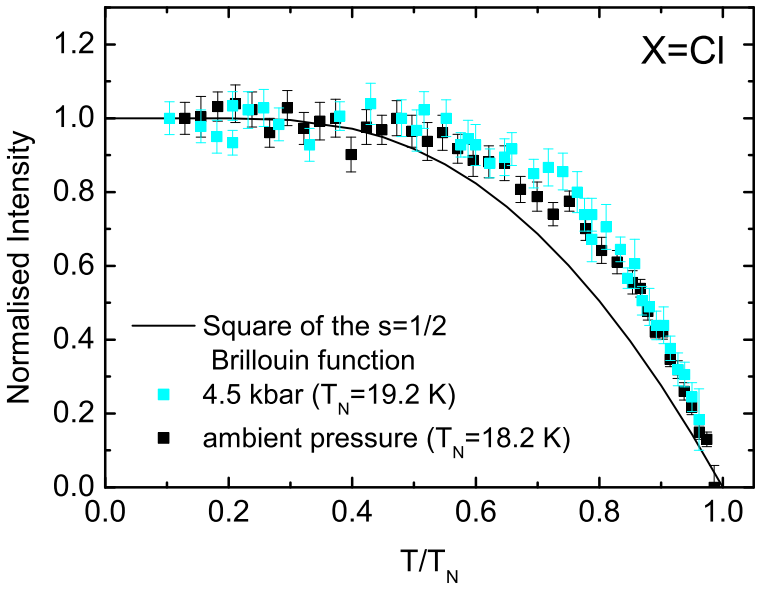

Figure 6.11: Normalised integrated intensity of the $\mathbf{Q} = (0.56\ 0.845\ 0.5)$ reflection of $Cu_2Te_2O_5Cl_2$ as a function of T/T_N, where $T_N = 18.2$ K for the ambient data (black) and $T_N = 19.2$ K for the 4.5 kbar data (cyan). This data was collected on D10 at the ILL.

reflection in ambient pressure drops to $\sim$ 13 % of its value at 2 K by 17.75 K, and by 18 K there is no longer a discernable peak. In contrast, in the 4.5 kbar data, the intensity of the magnetic reflection at 18.5 K is still $\sim$ 18 % of its value at 2 K, although at higher temperatures no peak can be resolved above the background level of scattering. From susceptiblity measurements and previous neutron diffraction measurements [80], the ambient pressure transition temperature of $Cu_2Te_2O_5Cl_2$ is known to be $T_N^{Cl} = 18.2$ K.

The square of the spin-1/2 Brillouin function (BF) can be used as a mean-field estimate of the temperature dependence of the intensity up to the magnetic transition. Figure 6.11 shows the normalised integrated intensity of the magnetic reflection as a function of T/T_N. For the ambient pressure data (black), T_N has been taken as 18.2 K, and for the 4.5 kbar data (cyan), T_N has been taken as 19.2 K. The solid black line is the square of the spin-1/2 Brillouin function [14].

The temperature dependence of the two data sets lie closest to each other when the transition temperature of the 4.5 kbar data is taken to be $T_N = 19.2$ K with respect to the ambient transition temperature of $T_N = 18.2$. This agrees well with the susceptibility measurements of $Cu_2Te_2O_5Cl_2$ presented in section 6.2.1, which indicated an increase in the transition temperature of $\sim$ 1 K under an applied pressure of 4.5 kbar. However, the temperature dependence of the transition does not fit the square of the spin-1/2 BF very well, with the data staying flatter to higher temperatures and falling more steeply near T_N than for the square of the BF. This indicates that the integrated intensity of the reflection does not follow a very mean field-like temperature dependence. In contrast, the temperature dependence of the integrated intensity of the lowest angle magnetic peak in polycrystalline data reported by Zaharko et al. [80], fits the square of the BF closely. It is unclear what gives rise to this discrepancy, although it may possibly be due to the fact that in the polycrystalline data the lowest angle magnetic peak may consist of a number of contributions from different domains.

Finally, similar neutron diffraction measurements of $Cu_2Te_2O_5Br_2$ under pressure have not been possible to date due to the difficulty of growing large enough single crystals of this compound. Such measurements would be highly beneficial to the understanding of the contrasting behaviour that this compound demonstrates under applied pressure.

6.2.3 Discussion

Pressure measurements often provide useful information about the underlying magnetic interactions in a system. As pressure is applied and the sample volume decreases one would expect, in general, the magnetic coupling strengths to increase due to the closer proximity of the atoms and resultant increased overlap of their orbitals. In particular, for $Cu_2Te_2O_5Br_2$ one may naively expect that the effect of pressure would be to push the magnetic behaviour toward that of the $Cu_2Te_2O_5Cl_2$

compound, which has a 7 % smaller volume. However, the magnetic behaviour may not be related to the sample volume in such a straightforward manner. In this system there are both intra- and inter-tetrahedral competing interactions, as well as the presence of an antisymmetric DM interaction. Figures 1.6, 1.7, 1.8 and 1.9 illustrate the exchange paths J_1, J_2, J_a, J_b, and J_c and section 1.3.4 discusses the theoretical and experimental work to date that has been concerned with the relative strengths of these exchange parameters. Due to the competition of the different exchange paths, the magnetic ordering is likely to be very sensitive to the relative coupling strengths of the interactions present, which may respond to pressure in different manners. It is therefore important to closely consider the effect of pressure on the structure of the material alongside the effects observed in the magnetic behaviour. A structural analysis of $Cu_2Te_2O_5Br_2$ under pressure using angle-dispersive x-ray powder diffraction has been reported by Wang et al. [77]. The authors present two key results. Firstly, they observe that the tetragonal unit cell phase is stable up to pressures of approximately 140 kbar, where there is a structural phase transition to a monoclinic unit cell. This will not be discussed further as the pressure range used in the work of this thesis ($<$ 12 kbar) is far lower than 140 kbar, and hence the sample remains in the tetragonal phase. Secondly, the authors refine the atomic positions in the tetragonal phase and observe that, (i) the inter-tetrahedral Br-Br distance decreases with increasing pressure and the Cu-Br-Br path becomes slightly more linear, and (ii) the Cu-Cu distances increase under pressure. In terms of the exchange paths, this corresponds to a decrease in the inter-tetrahedral distances over which the interactions J_a and J_b operate, and an increase in the intra-tetrahedral distances over which the J_1 and J_2 exchange parameters operate. It can also be inferred that the distance between tetrahedra separated along the c-axis, which corresponds to the path over which the J_c exchange interaction operates, decreases with increasing pressure. These results suggest that (i) the inter-tetrahedral exchange interactions J_a, J_b

and J_c may possibly increase under applied pressure, and (ii) the intra-tetrahedral exchange interactions J_1 and J_2 may possibly decrease under applied pressure. Unfortunately, similar structural studies of the chloride or mixed composition samples under pressure have not been reported.

This chapter is concerned with the effect of pressure on the magnetic behaviour of $Cu_2Te_2O_5(Br_xCl_{1-x})_2$. Firstly, consider the pressure dependence observed for the temperature at which the maxima in the susceptibility occurs (T_{max}) for compositions $x = 0$, 0.73 and 1. In all three samples T_{max} increases quite significantly under applied pressure. The rate of increase is greatest for the bromide (1.42(6) K/kbar), followed by the $x = 0.73$ composition (1.00(1) K/kbar), and is least for the chloride (0.52(3) K/kbar). In general, T_{max} is associated with the overall coupling strength of the system, and so it appears that in all three compounds the overall magnetic coupling increases quite significantly with pressure. However, it is not clear which exchange interactions determine the overall magnetic coupling in these materials. In the case of $Cu_2Te_2O_5Br_2$, Kreitlow et al. [43] attribute the increase in overall coupling strength to an increase in the intra-tetrahedral coupling strength under pressure. However, the work of Wang et al. [77] discussed above suggests that it is more likely that the inter-tetrahedral coupling increases with applied pressure, whereas the intra-tetrahedral coupling decreases with applied pressure. This indicates that the overall coupling strength may possibly be determined by the inter-tetrahedral coupling. For the case of $Cu_2Te_2O_5Cl_2$ and the doped $x = 0.73$ composition there is no corresponding structural data, and so it is not known how the different exchange paths respond to pressure relative to each other. However, if one were to assume that there is a similar structural behaviour under pressure in these materials as in $Cu_2Te_2O_5Br_2$, then the increase observed in T_{max} in these compounds could also possibly be attributed to an increase in the overall magnetic coupling determined by the inter-tetrahedral exchange paths.

More information about the underlying exchange interactions can perhaps be extracted by considering the relative behaviour of T_N with respect to T_{max}, and how this varies between the different compounds. It is first worth noting that from the single crystal neutron diffraction measurement of $Cu_2Te_2O_5Cl_2$ described in section 6.2.2, it was confirmed that the shift in the feature of $d^2\chi/dT^2$ with pressure observed in polycrystalline magnetic susceptibility measurements (see figure 6.5) was correctly attributed to a shift in the transition temperature. It is assumed that the shifts in the features of $d^2\chi/dT^2$ observed in the case of the bromide (figure 6.2) and the $x = 0.73$ (figure 6.8) samples also correspond to shifts in the respective transition temperatures. Similar single crystal neutron diffraction measurements of these compounds under pressure were not possible due to the difficulty of growing large enough crystals. Whilst in the chloride and the $x = 0.73$ compound T_{max} and T_N both increase with increasing pressure, for the bromide T_{max} increases while T_N^{Br} decreases. It is clear that the X=Br sample is not pushed toward the behaviour of the X=Cl sample under applied pressure (i.e. increasing T_N^{Br}), as may have been expected from a simple picture in which the volume of the bromide decreases towards the volume of the chloride. Instead, the bromide appears to move toward a non-magnetic phase as the applied pressure is increased. It is not clear how the pressure dependence of T_N^{Br} develops beyond ~ 6 kbar, and whether or not it is completely suppressed at some higher pressure. It has previously been suggested that $Cu_2Te_2O_5Br_2$ and $Cu_2Te_2O_5Cl_2$ lie either side of a quantum critical point [46, 27]. If this is the case, then these results suggest that externally applied pressure has the effect of pushing the bromide closer to the quantum critical point, and pushing the chloride away from it. The $x = 0.73$ composition, although somewhat intermediate in its behaviour, seems to follow more closely the chloride and is pushed slightly further from the possible quantum critical point with a very small increase in $T_N^{x=0.73}$ under pressure.

Consider now how the contrasting relative behaviour of T_N and T_{max} relate

to the underlying magnetic interactions in the three compounds. Firstly, in a low dimensional system the maxima in the magnetic susceptibility often gives a better indication of the underlying strength of the magnetic interactions than the actual transition temperature, which can reflect weaker 'parasitic' interactions that finally lock in the three dimensional order (as discussed in secion 5.3.2). Indeed, for $Cu_2Te_2O_5(Br_xCl_{1-x})_2$ the issue of the relative strengths of the possible interactions, and which determine the low dimensionality or which is dominant in driving the transition to 3D order, has yet to be established. However, it is clear that in the bromide the interaction driving the 3D order is not the same as that which can be thought of as mediating the overall (possibly low dimensional) coupling because T_{max} and T_N^{Br} act in the opposite sense under pressure. A possible scenario that could give rise to the opposite behaviour of T_{max} and T_N^{Br} in $Cu_2Te_2O_5Br_2$ under pressure, is one in which the intra-tetrahedral interactions play an important role in the transition to 3D magnetic order. In this configuration the Cu^{2+} ions could be thought of as forming square planar units (with intra-unit exchange interactions J_a and J_b), that couple along the c-axis via J_c. The transition to 3D magnetic order would require sufficient J_1 and J_2 interactions to couple the chains of square planar units. Under an applied pressure, J_1 and J_2 are thought to possibly decrease in strength [77], which could lead to a suppression of the magnetic transition temperature. In contrast, J_a, J_b and J_c are thought to possibly increase in strength under pressure [77], which in this case would lead to an increase in T_{max}. However, it may not be sufficient to think solely in terms of the relative strength of the inter and intra-tetrahedral interactions. Another means by which the magnetic transition in $Cu_2Te_2O_5Br_2$ could be suppressed is by an increase in the frustration on the tetrahedra, or possibly a weakening of the DM interaction under pressure, as these are also parameters that may play an important part in the stabilisation of a magnetically ordered state in this system.

In the $Cu_2Te_2O_5Cl_2$ and $x = 0.73$ samples, T_{max} and T_N both increase

under pressure. This may perhaps indicate that the interactions driving the overall magnetic coupling strength also play a role in determining the magnetic ordering temperature. The inter-tetrahedral interactions may mediate the low dimensional and short range correlations that give a measure of the overall coupling strength, but the strength of these interactions may also determine the magnetic ordering temperature. From ambient pressure spin dimer analysis [78] it is believed that the intra-tetrahedral exchange interaction J_1 is significantly larger in the chloride than in the bromide. In this sense, the chloride can be viewed as consisting of tetrahedral units (with intra-tetrahedral exchange interactions J_1 and J_2) that firstly correlate and order in low dimensions (in either 1 or 2 dimensions, depending on the relative strengths of the inter-tetrahedral couplings), before undergoing a transition to long range 3D order through a combination of the inter-tetrahedral parameters J_a, J_b and J_c. However, in order to probe this matter further, it is important to firstly understand the effect of pressure on the structure of these two compounds.

Finally, in all three samples a fall in the absolute value of the magnetic susceptibility is observed with increasing pressure over the whole temperature range measured. This shows that there is a systematically lower response of the magnetisation to the same applied magnetic field when pressure is applied to the sample. This could possibly be attributed to a suppression of the magnetic moment with increasing pressure. However, it could also arise due to a reduction in the response of the moments to the applied magnetic field, which may perhaps result from the proposed increase in the overall magnetic coupling strength under pressure. The percentage drop in the susceptibility at low temperatures is greatest in the bromide ($\sim$ 10 % /kbar), followed by the $x = 0.73$ sample ($\sim$ 4 % /kbar), and least in the in the chloride ($\sim$ 3.5 % /kbar).

6.3 Dynamic magnetic behaviour of $Cu_2Te_2O_5Br_2$ under pressure

6.3.1 Results

In section 6.2, the effect of externally applied pressure on the magnetic transition of $Cu_2Te_2O_5(Br_xCl_{1-x})_2$ was discussed. In this section, the effect of applied pressure on the dynamic magnetic behaviour of polycrystalline $Cu_2Te_2O_5Br_2$ is investigated using neutron inelastic scattering (NIS). The measurements were performed on the direct chopper spectrometer HET at ISIS. Hydrostatic pressure was applied externally to the sample using a CuBe lock-nut pressure cell (see section 2.2). The polycrystalline sample (of mass $\sim$ 1.5 g) was pressed into a pellet and placed in a PTFE capsule along with a single crystal of NaCl. The capsule was filled with the pressure medium Fluorinert and inserted into the pressure cell, which was then pressurised using a hydraulic press. In order to determine the precise pressure applied to the sample (P_1), the NaCl crystal was used as an *in situ* pressure gauge. Neutron diffraction measurements of NaCl were performed on PRISMA at ISIS, both in ambient pressure (P_0) and under the applied pressure P_1. Figure 6.12 shows the scattering intensity as a function of d-spacing in the range of one Bragg peak for (i) NaCl in ambient pressure at T = 300 K (green), (ii) NaCl under an applied pressure P_1^{300K} at T = 300 K (red), and (iii) NaCl under an applied pressure P_1^{4K} at T = 4 K (blue). The d-spacings of the peak positions were extracted by fitting the data to a Kropf function (a Gaussian convoluted with an exponential [31]) and the fits are marked as solid lines in figure 6.12. There is a clear shift ($\sim$ 0.035 Å) in the d-spacing of the Bragg peak under applied pressure compared to that at ambient pressure. Using the work of Decker [15, 16], in which the equation of state of NaCl has been calculated, the pressure at 4 K was determined to be $P_1^{4K} = 11.3(1)$ kbar.

The NIS measurements of $Cu_2Te_2O_5Br_2$ presented in chapter 5 revealed a

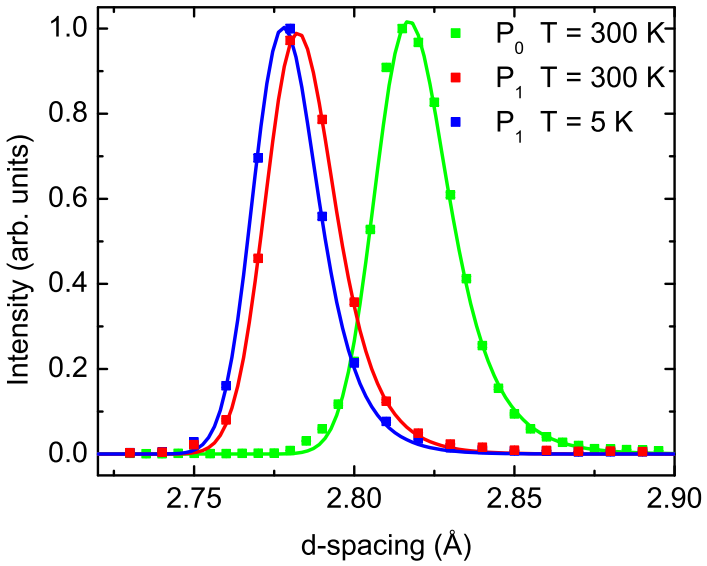

Figure 6.12: Scattering intensity as a function of d-spacing for NaCl, collected on PRISMA, ISIS. The measurements were made (i) in ambient pressure at T = 300 K (green), (ii) under pressure P_1^{300K} at T = 300 K (red), and (iii) under pressure P_1^{4K} at T = 4 K (blue). The solid lines are fits of the peaks using a Kropf function.

magnetic excitation with a flat component centred in energy at $\sim$ 5 meV, and a dispersive component centred at $|\mathbf{Q}| \sim 0.7$ Å^{-1}. In order to access this region of $(|\mathbf{Q}|, \omega)$-space with optimal resolution and flux on HET, an incident energy of $E_i = 18$ meV and chopper frequency of 150 Hz were used. In this configuration, a $|\mathbf{Q}|$ range of $\sim$ 0.5 to 1.5 Å^{-1} is accessible at an energy of 5 meV. The scattering intensity, $S(|\mathbf{Q}|, \hbar\omega)$, was measured as a function of momentum transfer ($|\mathbf{Q}|$) and energy transfer ($\hbar\omega$) for three different sample configurations; (i) sample in the pressure cell under a pressure of 11.3 kbar, (ii) sample in the pressure cell with the pressure completely removed (i.e. at ambient pressure), and (iii) empty pressure cell (including Fluorinert and PTFE capsule). The measurements were all performed at T = 4 K. The pressure cell has a large absorption cross section and its small sample space restricts the measurement to that of a small sample mass. Moreover, $Cu_2Te_2O_5Br_2$ has a small moment (S=1/2) and there is relatively low neutron flux on HET at the incident energy 18 meV required to access the

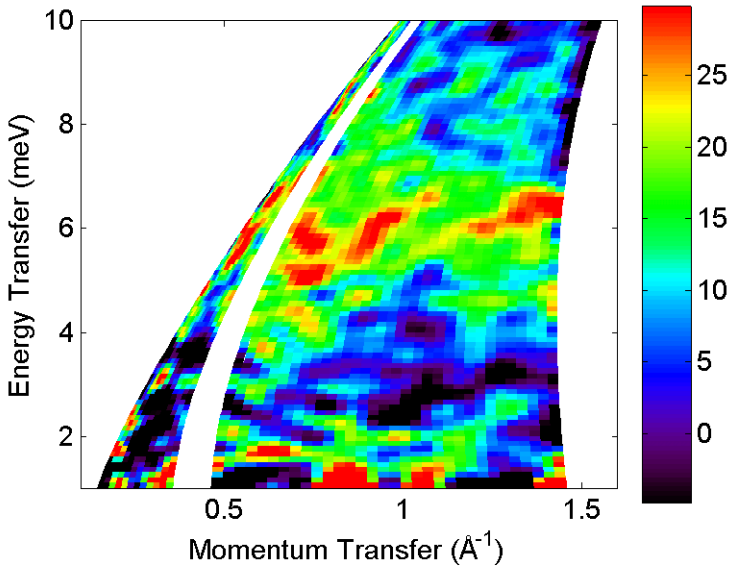

Figure 6.13: 2D map of $S(|\mathbf{Q}|, \hbar\omega)$ as a function of momentum transfer $|\mathbf{Q}|$ and energy transfer $\hbar\omega$ for $Cu_2Te_2O_5Br_2$ under an applied pressure of 11.3 kbar. The colour scale denotes the scattering intensity. The background scattering from the pressure cell has been subtracted from the data.

$(|\mathbf{Q}|, \omega)$ region of interest. Due to these factors the count times required for each measurement were several days, and the final statistics were fairly low. Scattering from the pressure cell, Fluorinert and PTFE capsule produces a large background, which unfortunately includes intensity in the inelastic channel around 5 meV. It was therefore very important to subtract the empty pressure cell measurement from both of the sample measurements in order to extract the scattering from the sample alone. In fact this background subtraction ignores multiple scattering involving the sample and cell, but under the assumption that this is relatively low the subtraction should give a reasonable approximation to the sample scattering.

Figure 6.13 is a 2D plot of $S(|\mathbf{Q}|, \hbar\omega)$ as a function of $|\mathbf{Q}|$ and $\hbar\omega$ (with the colour scale denoting the scattering intensity), for $Cu_2Te_2O_5Br_2$ under an applied pressure of 11.3 kbar. The background scattering from the pressure cell has been subtracted from the data. Unfortunately the statistics are not sufficiently high to make clear $S(|\mathbf{Q}|, \hbar\omega)$ versus $|\mathbf{Q}|$ cuts of the magnetic excitation in different

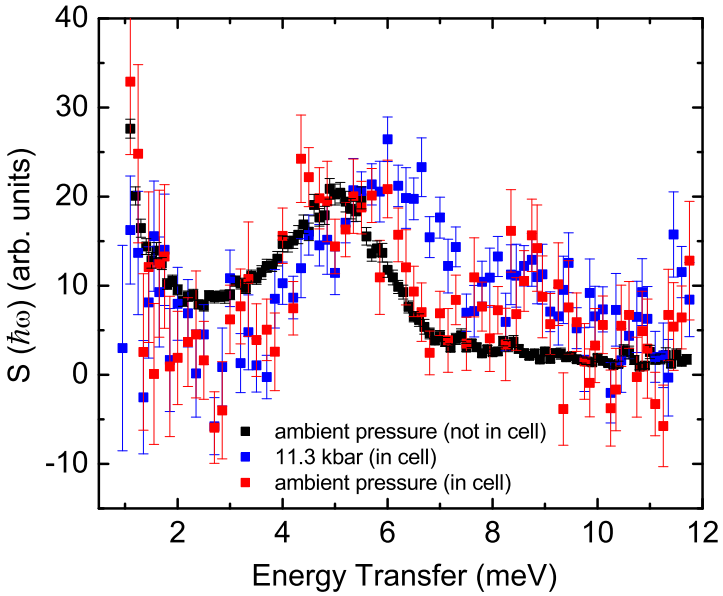

Figure 6.14: $S(|\mathbf{Q}|, \hbar\omega)$ versus energy transfer for $Cu_2Te_2O_5Br_2$, summed over 0.5 Å^{-1} $< |\mathbf{Q}| <$ 1.5 Å^{-1}. Data for the sample in the pressure cell under 11.3 kbar is shown in blue, for the sample in the pressure cell in ambient pressure in red, and for the sample in ambient pressure and not in the pressure cell in black.

regions of energy transfer. It is therefore difficult to investigate the effect of pressure on the dispersive component of the magnetic excitation. However, from this 2D plot it appears that the dispersive component is still present, and there is no indication that it has altered significantly under applied pressure (it can be compared with figure 5.1 in section 5.2.1). Figure 6.14 shows $S(|\mathbf{Q}|, \hbar\omega)$ versus $\hbar\omega$ summed over the $|\mathbf{Q}|$ range 0.5 Å^{-1} $< |\mathbf{Q}| <$ 1.5 Å^{-1} for $Cu_2Te_2O_5Br_2$ in ambient pressure (red) and under an applied pressure of 11.3 kbar (blue) at T $=$ 4 K. In both cases the background has been subtracted. In order to obtain better statistics at ambient pressure, a measurement was also performed with the sample simply wrapped in Al foil and not placed in a pressure cell (taken at T $=$ 7 K). This both reduced the amount of absorption and allowed a much larger sample mass ($\sim$ 15 g compared to $\sim$ 1.5 g), resulting in much better statistics in a far shorter counting time. Figure 6.14 also shows $S(|\mathbf{Q}|, \hbar\omega)$ versus $\hbar\omega$ summed over

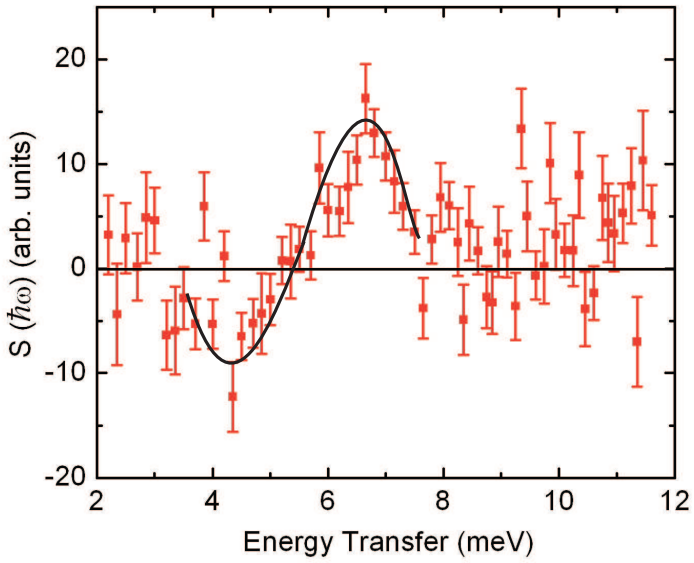

Figure 6.15: $S(|\mathbf{Q}|, \hbar\omega)$ versus energy transfer for $Cu_2Te_2O_5Br_2$, in which the ambient pressure data has been subtracted from the 11.3 kbar data. The data has been summed over 0.5 Å^{-1} $< |\mathbf{Q}| <$ 1.5 Å^{-1}. The solid line is a guide to the eye.

the same $|\mathbf{Q}|$ range for this configuration (black). A peak in the density of states is observed at $\sim$ 5 meV in ambient pressure for the case in which the sample is in the pressure cell as well as the case in which it is not in the pressure cell. Indeed, $S(|\mathbf{Q}|, \hbar\omega)$ versus $\hbar\omega$ for both of the ambient pressure measurements are very similar, as expected, although there are small discrepancies. In particular, at low energy transfer ($\sim$ 1 - 4 meV) $S(|\mathbf{Q}|, \hbar\omega)$ is lower for the ambient pressure data taken with the sample in the pressure cell compared to that taken with the sample not in the pressure cell. This may possibly be an artefact of the background subtraction, which may have been over-estimated in this region. However, the peak in the density of states for the sample under 11.3 kbar is at $\sim$ 6 meV, showing a shift of approximately 1 meV from the ambient pressure data. This shift is more clearly illustrated in figure 6.15, in which the ambient pressure data (taken with the sample in the pressure cell) is subtracted from the 11.3 kbar data. The

experimental setup and instrumental configuration were identical in both cases, hence the subtraction gives the difference in $S(|\mathbf{Q}|, \hbar\omega)$ as a function of energy transfer between measuring under 11.3 and in ambient pressure. The data shows an S-like feature (marked as a solid line in figure 6.15 as a guide to the eye), which corresponds to the shifting of the peak under pressure. The negative part of the S-shape feature indicates that there is less intensity in the 11.3 kbar data in the energy region $\sim$ 3 - 5.5 meV, in comparison with the ambient pressure data. Similarly, the positive part of the S-shape indicates that there is more intensity in the 11.3 kbar data in the region $\sim$ 5.5 - 8 meV compared with the ambient pressure data. From figure 6.14, it appears that there may also be a small broadening of the peak as well as a shift of the centre of the peak to higher energy when under applied pressure.

6.3.2 Discussion

The effect of externally applied pressure on the dynamic magnetic behaviour of $Cu_2Te_2O_5Br_2$ appears to be rather more subtle than its effect on the magnetic transition temperature described in section 6.2. The most notable change in the dynamics under an applied pressure of 11.3 kbar is a shift of the peak in the density of states of the magnetic excitations to 6 meV, from 5 meV in ambient pressure.

In the isolated tetrahedra model, the magnetic excitation present at 5 meV in ambient pressure measurements would correspond to a singlet-triplet spin-gap of $\Delta_{Br} = J_1 = 5$ meV ($J_1 > J_2$). Under pressure, the increase of the peak in the density of states to 6 meV would require the intra-tetrahedral interaction J_1 to increase. However, the measurements of Wang et al. [77] suggest that under pressure this interaction should perhaps decrease. If, however, the system is considered to consist of isolated square planar units mediated by the inter-tetrahedral J_a and J_b interactions, then the peak energy in the density of states would be determined by the strength of J_a and J_b. The work of Wang et al. [77] indicates

that these inter-tetrahedral interactions do possibly increase under pressure, which could explain the small shift of the peak in the density of states to 6 meV.

However, in a magnetically ordered system there must be some form of coupling between the Cu^{2+} clusters, whether they are tetrahedra or square planar units. Nevertheless, an increase in the overall magnetic coupling with pressure (as reported in section 6.2) is consistent with an increase in the energy scale of the magnetic excitations. Unfortunately the statistics of the NIS measurements under pressure are not sufficient to carry out a detailed analysis of the $|\mathbf{Q}|$-dependence in different regions of energy transfer. However, it does appear that the dispersive component of the magnetic excitation in $Cu_2Te_2O_5Br_2$ observed in ambient pressure is still present when a pressure of 11.3 kbar is applied. If the behaviour of T_N^{Br} as a function of pressure displayed in figure 6.3 is extrapolated to 11.3 kbar, one would expect the transition temperature to be lower than 4 K, and possibly even suppressed close to T = 0 K. Therefore the NIS measurement was most probably performed above the transition temperature. It is worth remembering that in the ambient pressure measurements reported in chapter 5, the dispersive component in $Cu_2Te_2O_5Br_2$ remained well above the transition temperature, and was therefore thought to be supported by low dimensional order or short range correlations. Similarly, the presence of the dispersive component in a pressure of 11.3 kbar, under which the transition to 3D magnetic order has been largely suppressed, may also be explained in terms of the low dimensional order or short range correlations. Indeed, the proposed increase in the overall coupling strength under applied pressure may correspond to an increase in the strength of the low dimensional couplings that support the dispersive excitations.

It would be very interesting to perform a more detailed NIS study of this compound under pressure, with higher statistics, more pressures and also a study of the temperature dependence under pressure. A similar investigation of $Cu_2Te_2O_5Cl_2$ and mixed composition samples would also be informative. Such

measurements could potentially reveal further and more conclusive information about the underlying exchange interactions. However, there is a restriction on the feasibility of such measurements due to the very large counting times required with currently available experimental instrumentation. In order to make detailed NIS studies of low moment magnetic systems such as this under pressure, a combination of increased sample space in the pressure cell, reduced absorption of the pressure cell, and strong focusing of the neutrons are required.

6.4 Chapter summary

The effect of externally applied pressure on the magnetic transition temperature (T_N) of $Cu_2Te_2O_5(Br_xCl_{1-x})_2$ with $x = 0$, 0.73 and 1, has been studied using a combination of susceptibility measurements and neutron diffraction. T_N is observed to increase linearly with increasing pressure for the chloride, whilst it decreases rapidly towards T = 0 K in the case of the bromide. For the mixed composition the behaviour of T_N is somewhat X=Cl-like, with a very small increase with increasing pressure. The contrasting behaviour of the chloride and bromide highlights the possibility that they lie either side of a quantum critical point, and that pressure pushes the bromide towards this whilst pushing the chloride and $x = 0.73$ composition away from it. In all three compounds the temperature of the maxima in the susceptibility (T_{max}), which is associated with the overall magnetic coupling strength, was observed to increase significantly with pressure. It is suggested that this is related to an increase in the inter-tetrahedral coupling strengths under pressure.

Neutron inelastic scattering (NIS) measurements of $Cu_2Te_2O_5Br_2$ revealed a small shift in the peak in the magnetic density of states from $\sim$ 5 meV in ambient pressure to $\sim$ 6 meV under an applied pressure of 11.3 kbar, which is associated with the increase in the overall magnetic coupling strength. In addition, the dis-

persive component of the magnetic excitation is still present at 11.3 kbar, and may be supported by low dimensional short range order. Further NIS measurements of the chloride and a number of mixed composition samples (particularly in the range $x > 0.73$) would be highly beneficial in furthering the understanding of this system. A study of the temperature dependence of these samples under pressure may also reveal information about the underlying interactions.

Chapter 7

Thesis Overview

The spin-tetrahedal compounds $Cu_2Te_2O_5Br_2$ and $Cu_2Te_2O_5Cl_2$ exhibit intriguing magnetic behaviour, demonstrating significantly different properties despite the similarity of their structures. In this thesis various aspects of their static and dynamic magnetic behaviour, as well as those of intermediate composition samples $Cu_2Te_2O_5(Br_xCl_{1-x})_2$, $(0 < x < 1)$, have been investigated.

Firstly, in chapter 3 the growth and characterisation of polycrystalline samples of $Cu_2Te_2O_5(Br_xCl_{1-x})_2$, $x = 0$, 0.25, 0.52, 0.63, 0.73 and 1, were described. Magnetic susceptibility measurements of the end compounds $Cu_2Te_2O_5X_2$ (X=Br,Cl) revealed transition temperatures of T_N^{Br}= 11.4 K and T_N^{Cl} =18.2 K for X=Br and X=Cl respectively, in accordance with reference [46]. It was further observed that the transition temperatures of the mixed compositions decrease linearly with increasing x from the chloride to the bromide. Anomalies in the temperature dependence of the heat capacity were also observed at the respective transition temperatures of each composition. The field dependence of the anomalies for $Cu_2Te_2O_5X_2$ (X=Br,Cl) agreed with the previously reported behaviour [46], which showed the anomaly to decrease in height and shift to lower temperatures in the chloride under an applied magnetic field, but increase in height and shift to higher temperatures under an applied magnetic field in the bromide. Interestingly, the

heat capacity data presented in chapter 3 showed all the mixed compositions to follow a X=Cl-like field dependence, suggesting the possibility of a significant change in the underlying magnetic properties within the doping range $0.73 < x \leq 1$. Furthermore, it was also observed from the heat capacity measurements that less than 65 % of the theoretical total magnetic entropy of the samples was recovered at temperatures up to their respective transition temperatures. In particular, for the bromide a maximum of $\sim$ 30 % of the predicted total magnetic entropy was accounted for at temperatures under T_N^{Br}= 11.4 K. This suggests that there may possibly be low dimensional order and/or short range correlations present at temperatures considerably above T_N, which account for the missing magnetic entropy below the transition to long range 3D order.

In chapter 4, an investigation of the magnetic structure of $Cu_2Te_2O_5(Br_xCl_{1-x})_2$ by neutron diffraction was presented. Measurements of polycrystalline samples of composition x = 0, 0.25, 0.52, 0.73 and 1 revealed all of the compounds to have long range incommensurate magnetic order at T = 2 K, with propagation vectors changing linearly with x, from $\boldsymbol{\kappa_{Br}}$ = [0.170, 0.350, 1/2] for the bromide to $\boldsymbol{\kappa_{Cl}}$ = [0.150, 0.420, 1/2] for the chloride. A single crystal neutron diffraction study of $Cu_2Te_2O_5Br_2$ allowed a number of possible models of the magnetic structure to be proposed. These all consisted of a helical magnetic structure with four common features. Firstly, the Cu1 and Cu2 moments pair together and rotate on a common helix at a canting angle of $\sim 20^o$ to each other. Figure 7.1 shows the positions of the four Cu ions on the tetrahedra, where $x \sim 0.730$, $y \sim 0.452$ and $z \sim 0.158$. Secondly, the Cu3 and Cu4 moments also pair up and rotate in the same helical plane with a canting angle of $\sim 120^o$. Thirdly, all four Cu^{2+} moments rotate on planes that are close to the xz-plane. Finally, the refined moment of the Cu^{2+} ions (equal by assumption) is $\sim$ 0.40 μ_B/ion. However, it was not possible to differentiate between the proposed models to conclusively select one final model for the magnetic structure of $Cu_2Te_2O_5Br_2$. Neither could definitive information about

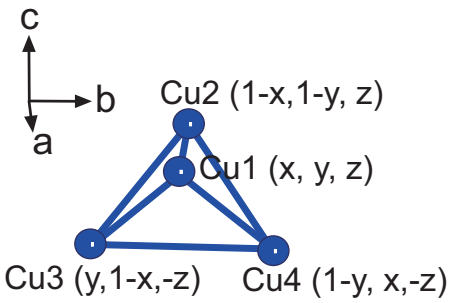

Figure 7.1: Positions of the four Cu ions that make up the tetrahedra in $Cu_2Te_2O_5Br_2$, where $x \sim 0.730$, $y \sim 0.452$ and $z \sim 0.158$.

the relative strengths of the various underlying exchange interactions be extracted solely on the basis of these measurements. The models determined for the magnetic structure of single crystal $Cu_2Te_2O_5Br_2$, as well as the proposed magnetic structure of single crystal $Cu_2Te_2O_5Cl_2$ [80], were applied to the polycrystalline data of all compositions ($x = 0$, 0.25,0.52,0.73 and 1). Small discrepancies between the single crystal and polycrystalline data were observed, due in part to the presence of different magnetic domains in these materials. However, in general the results presented indicate that the magnetic structure of all of the compositions are reasonably similar.

In chapter 5, the dynamic magnetic behaviour of $Cu_2Te_2O_5(Br_xCl_{1-x})_2$ was investigated by neutron inelastic scattering of polycrystalline samples of composition $x = 0$, 0.25, 0.52, 0.63, 0.73 and 1. Magnetic excitations with a dispersive component were observed in all of the compounds, arising from the Bragg peaks of the incommensurate magnetic order. Peaks in the density of states of the magnetic excitations were observed at $\sim$ 5 meV in the bromide and $\sim$ 6 meV in the chloride. In the doping range $x \sim 0.6$ - 0.7, two peaks in the density of states at $\sim$ 4 and $\sim$ 7 meV were observed. It remains unclear what gives rise to these magnetic excitations, although the data indicates that exchange interactions on an inter-tetrahedral length scale play an important role. The temperature dependence of the magnetic excitations are particularly interesting. The excitation spectra of

the chloride softens toward the ordering temperature, whilst both the dispersive and flat components of the magnetic excitations in the bromide remain present well above T_N^{Br}. The existence of dispersive excitations at temperatures much greater than the transition temperature may suggest the possibility of low dimensional and/or short range correlations well above T_N^{Br}. The magnetic excitations of the mixed compositions all exhibit a X=Cl-like temperature dependence, again indicating that a significant change in the underlying magnetic properties occurs in the region $x > 0.73$.

The effect of externally applied pressure on the magnetic behaviour of $Cu_2Te_2O_5(Br_xCl_{1-x})_2$ with $x = 0$, 0.73 and 1, is discussed in chapter 6. In magnetic suscpetibilty measurements under pressure it was observed that the overall coupling strength of all three compositions increases significantly with increasing pressure. This can perhaps be attributed to a possible increase in the strength of the inter-tetrahedral couplings under pressure. The transition temperature of the chloride was found to increase linearly with pressure, at a rate of 0.23(2) K/kbar. The transition temperature of the $x = 0.73$ composition also increased under applied pressure, although only at a small rate of 0.04(1) K/kbar. However, the bromide showed starkly contrasting behaviour with a large suppression of the transition temperature under pressure, at a rate -0.95(9) K/kbar. This indicates that the bromide is in the vicinity of a non-magnetic phase, and that pressure pushes it toward this state. However, in neutron inelastic scattering measurements of $Cu_2Te_2O_5Br_2$ under pressure only a small change to the ambient pressure magnetic excitations were observed. The peak in the density of states was seen to shift from $\sim$ 5 meV in ambient pressure to $\sim$ 6 meV under an applied pressure of 11.3 kbar, which was associated with the increase in the overall magnetic coupling strength.

Whilst the work of this thesis has added to the current knowledge and understanding of this topic, it has equally highlighted the complexity of $Cu_2Te_2O_5(Br_xCl_{1-x})_2$,

and the need for further investigations to reach a more complete understanding of the system. Future work must encompass several areas of study. Firstly, the growth of high quality, large single crystals of both end compounds and a range of intermediate compositions (particularly in the range $0.73 < x < 1$) is essential. This would allow a more complete neutron diffraction investigation of the underlying magnetic structure of these materials, and in particular the presence and importance of different magnetic domains. Furthermore, single crystal neutron inelastic scattering experiments of a range of compositions would greatly enhance the understanding of the dynamic magnetic behaviour, which the results of chapter 5 indicate to be very interesting on the basis of polycrystalline measurements. The results presented in chapter 6 suggest that externally applied pressure has a very interesting and varied effect on the magnetic behaviour of these compounds, but significant work remains in order to improve the understanding of this. In particular, a detailed structural (nuclear and magnetic) analysis of the effect of pressure on a range of the compositions would be beneficial. Improved instrumentation, larger sample sizes and a lot of neutron beamtime are required in order to probe these intriguing properties further.

Bibliography

[1] I. Affleck. Quantum spin chains and the Haldane gap. *J. Phys.: Condensed Matter*, **1**(3047), 1989.

[2] N.W. Ashcroft and N. Mermin. *Solid State Physics*. Saunders College Publishing, 1976.

[3] G.E. Bacon. *Neutron Diffraction*. Clarendon Press, 1975.

[4] M. Bée. *Quasielastic Neutron Scattering*. Institute of Physics Publishing, 1988.

[5] P.R. Bevington. *Data Reduction and Error Analysis for the Physical Sciences*. McGraw-Hill, 1969.

[6] S. Blundell. *Magnetism in Condensed Matter*. Oxford University Press, 2001.

[7] S.T. Bramwell and M.J.P. Gingras. Spin ice state in frustrated magnetic pyrochlore materials. *Science*, **294**(1495), 2001.

[8] W. Brenig and K.W. Becker. Magnetism of a tetrahedral cluster spin chain. *Phys. Rev. B*, **64**(214413), 2001.

[9] P.J. Brown. *International Tables for Crystallography*, page 391. Kluwer Academic, Dordrecht, 1992.

[10] W.J.L. Buyers, R.M. Morra, R.L. Armstrong, M.J.Hogan, P. Gerlach, and K. Hirakawa. Experimental evidence for the Haldane gap in spin-1, nearly isotropic, antiferromagnetic chain. *Phys. Rev. Lett.*, **56**(371), 1986.

[11] B. Canals and C. Lacroix. Pyrochlore antiferromagnet: A three-dimensional quantum spin liquid. *Phys. Rev. Lett.*, **80**(2933), 1998.

[12] E. Dagotto. Experiments on ladders reveal a complex interplay between a spin-gapped normal state and superconductivity. *Rep. Prog. Phys.*, **62**(1525), 1999.

[13] E. Dagotto and T.M. Rice. Surprises on the way from one- to two-dimensional quantum magnets: The ladder materials. *Science*, **271**(618), 1996.

[14] M.I. Darby. Tables of the Brillouin function and of the related function for the spontaneous magnetization. *Brit. J. Appl. Phys.*, **18**(1415), 1967.

[15] D.L. Decker. Equation of state of NaCl and its uses as a pressure gauge in high-pressure research. *J. Appl. Phys.*, **36**(1), 1965.

[16] D.L. Decker. High pressure equation of state for NaCl, KCl, and CsCl. *J. Appl. Phys.*, **42**(8), 1971.

[17] A.-J. Dianoux and G. Lander. *Neutron Data Booklet*. Institut Laue-Langevin, 2002.

[18] H.T. Diep. *Magnetic Systems with Competing Interactions*. World Scientific, 1994.

[19] I. Dzyaloshinsky. A thermodynamic theory of 'weak' ferromagnetism of antiferromagnets. *J. Phys. Chem. Solids*, **4**(241), 1958.

[20] P. Fazekas. *Lecture Notes on Electron Correlation and Magnetism*. World Scientific Publishing Co., Pte. Ltd., 1999.

[21] K.H. Fischer and J.A. Hertz. *Spin Glasses*. Cambridge University Press, 1991.

[22] H. Fukuyama, T. Tanimoto, and M. Saito. Antiferromagnetic long range order in disordered spin-Peierls systems. *J. Phys. Soc. Jpn.*, **65**(1182), 1996.

[23] A. Furrer and H.U. Gudel. Interference effects in neutron scattering from magnetic clusters. *Phys. Rev. Lett.*, **39**(657), 1977.

[24] S. Gasiorowitz. *Quantum Mechanics*. John Wiley and Sons, 1996.

[25] J.B. Goodenough. *Magnetism and the Chemical Bond*. Wiley, Cambridge, MA, 1963.

[26] E.S.R Gopal. *Specific Heats at Low Temperatures*. Heywood Books for Iliffe Books Ltd., 1966.

[27] C. Gros, P. Lemmens, M. Vojta, R. Valentí, K.-Y. Choi, H. Kageyama, Z. Hiroi, N.V. Mushnikov, T. Goto, M. Johnsson, and P. Millet. Longitudinal magnon in the tetrahedral spin system $Cu_2Te_2O_5Br_2$ near quantum criticality. *Phys. Rev. B*, **67**(174405), 2003.

[28] A.P. Guimaraes. *Magnetism and Magnetic Resonances in Solids*. John Wiley & Sons, 1998.

[29] F.D.M Haldane. Nonlinear field theory of large-spin Heisenberg antiferromagnets: Semiclassically quantized solitons of the one-dimensional easy-axis Néel state. *Phys. Rev. Lett.*, **50**(1153), 1983.

[30] O. Halpern and M.H. Johnson. On the magnetic scattering of neutrons. *Phys. Rev.*, **55**(898), 1939.

[31] M.J. Harris and M.J. Bull. *The PRISMA GENIE Data Analysis Manual*. http://www.isis.rl.ac.uk/excitations/prisma/index.htm, 1998.

[32] M. Hase, I. Terasaki, and K. Uchinokura. Observation of the spin-Peierls transition in linear Cu^{2+} (spin-$1/2$) chains in an inorganic compound $CuGeO_3$. *Phys. Rev. Lett.*, **70**(3651), 1993.

[33] J.M. Hastings and L.M. Corliss. Magnetic structure of manganese chromite. *Phys. Rev.*, **126(2)**(556), 1962.

[34] L. Van Hove. Correlations in space and time and Born approximation scattering in systems of interacting particles. *Phys. Rev.*, **95**(249), 1954.

[35] J. Jensen, P. Lemmens, and C. Gros. Magnetic Raman scattering of the ordered tetrahedral spin-$1/2$ clusters in $Cu_2Te_2O_5(Br_{1-x}Cl_x)_2$ compounds. *Europhys. Lett.*, **64**(689), 2003.

[36] M.W. Johnson. DISCUS: A computer program for the calculation of multiple scattering effects in inelastic neutron scattering experiments. *UKAEA Harwell Report*, AERE-(R7682), 1974.

[37] M. Johnsson, K. W. Tornroos, F. Mila, and P.Millet. Tetrahedral clusters of copper(II): Crystal structures and magnetic properties of $Cu_2Te_2O_5X_2$ (X=Cl,Br). *Chem. Mater.*, **12**(2853), 2000.

[38] H. Kageyama, K. Yoshimura, R. Stern, N.V. Mushnikov, K. Onizuka, M. Kato, K. Kosuge, C.P. Slichter, T. Goto, and Y. Ueda. Exact dimer ground state and quantized magnetization plateaus in the two-dimensional spin system $SrCu_2(BO_3)_2$. *Phys. Rev. Lett.*, **82**(3168), 1999.

[39] M.A. Kastner, R.J. Birgeneau, G. Shirane, and Y. Endoh. Magnetic, transport, and optical properties of monolayer copper oxides. *Rev. Mod. Phys.*, **70**(897), 1998.

[40] N. Kato and M. Imada. Spin gap in two-dimensional Heisenberg model for CaV_4O_9. *J. Phys. Soc. Jpn.*, **64**(4105), 1995.

[41] S. Kirpatrick, C.D. Gelatt, and M.P. Vecchi. Optimization by simulated annealing. *Science*, **220**(671), 1983.

[42] V.N. Kotov, M.E. Zhitomirsky, M. Elhajal, and F. Mila. Weak antiferromagnetism and dimer order in quantum systems of coupled tetrahedra. *Phys. Rev. B*, **70**(214401), 2004.

[43] J. Kreitlow, S. Sullow, D. Menzel, J. Schoenes, P. Lemmens, and M. Johnsson. Unusual criticality of $Cu_2Te_2O_5Br_2$ under pressure. *J. Magn. Magn. Mater.*, **290-291**(959), 2005.

[44] S.-H. Lee, C. Broholm, T.H. Kim, W. Ratcliff II, and W.-W. Cheong. Local spin resonance and spin-Peierls-like phase transition in a geometrically frustrated antiferromagnet. *Phys. Rev. Lett.*, **84**(3718), 2000.

[45] P. Lemmens, K.-Y. Choi, G. Guntherodt, M. Johnsson, P. Millet, F. Mila, R. Valentí, C. Gros, and W. Brenig. Search for quantum criticality in the spin tetrahedra system $Cu_2Te_2O_5(Br_xCl_{1-x})_2$. *Physica B*, **329-333**(1049), 2003.

[46] P. Lemmens, K.-Y. Choi, E.E. Kaul, C. Geibel, K. Becker, W. Brenig, R. Valentí, C. Gros, M. Johnsson, P. Millet, and F. Mila. Evidence for an unconventional magnetic instability in the spin-tetrahedral system $Cu_2Te_2O_5Br_2$. *Phys. Rev. Lett.*, **87**(227201), 2001.

[47] S.W. Lovesey. *Theory of Neutron Scattering from Condensed Matter*. Oxford University Press, 1984.

[48] S. Ma, C. Broholm, D.H. Reich, B.J. Sternlieb, and R.W. Erwin. Dominance of long-lived excitations in the antiferromagnetic spin-1 chain NENP. *Phys. Rev. Lett.*, **69**(3571), 1992.

[49] K. Manabe, H. Ishimoto, N. Koide, Y. Sasago, and K. Uchinokura. Antiferromagnetic long-range order in $Cu_{1-x}Zn_xGeO_3$. *Phys. Rev. B*, **58**(R575), 1998.

[50] E. Manousakis. The spin-1/2 Heisenberg antiferromagnet on a square lattice and its application to the cuprous oxides. *Rev. Mod. Phys.*, **63**(1), 1991.

[51] W. Marshall and S.W. Lovesey. *Theory of Thermal Neutron Scattering*. Oxford University Press, 1971.

[52] M. Matsumoto, B. Normand, T.M. Rice, and M. Sigrist. Field- and pressure-induced magnetic quantum phase transitions in $TlCuCl_3$. *Phys. Rev. B*, **69**(054423), 2004.

[53] D.C. Mattis. *The Theory of Magnetism I*. Springer-Verlag, 1981.

[54] L.B. McCusker, R.B. Von Dreele, D.E. Cox, D. Louer, and P. Scardi. Rietveld refinement guidelines. *J. Appl. Cryst.*, **32**(36-50), 1999.

[55] T. Moriya. Anisotropic superexchange interaction and weak ferromagnetism. *Phys. Rev.*, **120**(91), 1960.

[56] S.E. Nagler, D.A. Tennant, R.A. Cowley, T.G. Perring, and S.K. Satija. Spin dynamics in the quantum antiferromagnet chain compound $KCuF_3$. *Phys. Rev. B*, **44**(12361), 1991.

[57] Nield. *Diffuse Neutron Scattering from Crystalline Materials*. Oxford University Press, 2001.

[58] J. Pannetier. Simulated annealing: An introductory review. *Inst. Phys. Conf. Ser.*, **107**(23), 1990.

[59] C. Pfleiderer and A.D. Huxley. Pressure dependence of the magnetisation in the ferromagnetic superconductor UGe_2. *Phys. Rev. Lett.*, **89**(147005), 2002.

[60] C. Pfleiderer, G.J. McMullan, S.R. Julian, and G.G. Lonzarich. Magnetic quantum phase transition in MnSi under hydrostatic pressure. *Phys. Rev. B*, **55**(8330), 1997.

[61] M. Prester, A. Smontara, I. Zivković, A. Bilusić, D. Drobac, H. Berger, and F. Bussy. Ground-state order and spin-lattice coupling in tetrahedral spin systems $Cu_2Te_2O_5X_2$ (X=Br or Cl). *Phys. Rev. B*, **69**(180401), 2004.

[62] A.I.M Rae. *Quantum Mechanics*. Institute of Physics Publishing, 1980.

[63] A.P. Ramirez. Strongly geometrically frustrated magnets. *Annu. Rev. Mater. Sci.*, **24**(453), 1994.

[64] H.M. Rietveld. A profile refinement method for nuclear and magnetic structures. *J. Appl. Crystallography*, **2**(65), 1969.

[65] J. Rodriguez-Carvajal. http://www-llb.cea.fr/fullweb/powder.htm.

[66] J. Rodriguez-Carvajal. Recent advances in magnetic structure determination by neutron powder diffraction. *Physica B*, **192**(55), 1993.

[67] S. Sachdev. *Quantum Phase Transitions*. Cambridge University Press, 1999.

[68] R.R.P. Singh, W.E. Pickett, D.W. Hone, and D.J. Scalapino. Some recent issues in quantum magnetism. *Comments on Modern Physics 2*, B1, 2000.

[69] A.V. Sologubenko, R. Dell'Amore, H.R. Ott, and P. Millet. Anisotropic field dependence of the magnetic transition in $Cu_2Te_2O_5Br_2$. *Eur. Phys. J. B*, **42**(549), 2004.

[70] S.L. Sondhi, S.M. Girvin, J.P.Caini, and D. Shahar. Continuous quantum phase transitions. *Rev. Mod. Phys.*, **69**(315), 1997.

[71] G.L. Squires. *Introduction to the Theory of Thermal Neutron Scattering*. Cambridge University Press, 1978.

[72] A. Sundaresan, A. Maignan, and B. Raveau. Evidence for 2D-3D magnetic ordering of Gd in high-T_c-related $CaGdCuO_3Cl$ and $Ca_4R_2Cu_3O_8Cl_4$ (R=Gd,Sm). *Phys. Rev. B*, **54**(12576), 1996.

[73] S. Taniguchi, T. Nishikawa, Y. Yasui, Y. Kobayashi, M. Sato, T. Nishioka, M. Kontani, and K. Sano. Spin gap behaviour of s=1/2 quasi-two-dimensional system CaV_4O_9. *J. Phys. Soc. Jpn.*, **64**(2758), 1995.

[74] K. Totsuka and H.-J. Mikeska. Low-lying excitations and magnetization process of coupled tetrahedral systems. *Phys. Rev. B*, **66**(054435), 2002.

[75] R. Valentí, T. Saha-Dasgupta, C.Gros, and H. Rosner. Halogen-mediated exchange in the coupled-tetrahedra quantum spin systems $Cu_2Te_2O_5X_2$ (X=Br,Cl). *Phys. Rev. B*, **67**(245110), 2003.

[76] D. Wagner. *Introduction to the Theory of Magnetism*. Pergamon Press Ltd., 1972.

[77] X. Wang, I. Loa, K. Syassen, P. Lemmens, M. Hanfland, and M. Johnsson. The effect of pressure on the structural properties of the spin-tetrahedral compound $Cu_2Te_2O_5Br_2$. *J. Phys.: Condens. Matter*, **17**(S807-S812), 2005.

[78] M.-H. Whangbo, H.-J. Koo, D. Dai, and D. Jung. Interpretation of the magnetic structures of $Cu_2Te_2O_5X_2$ (X=Cl,Br) and $Ca_{3.1}Cu_{0.9}RuO_6$ on the basis of electronic structure considerations: cases for strong super-superexchange interactions involving Cu^{2+} ions. *Inorg.Chem*, **42**(3898), 2003.

[79] O. Zaharko. Private communication.

[80] O. Zaharko, A. Daoud-Aladine, S. Streule, J. Mesot, P.-J. Brown, and H. Berger. Incommensurate magnetic ordering in $Cu_2Te_2O_5X_2$ (X=Cl,Br) studied by neutron diffraction. *Phys. Rev. Lett.*, **93**(217206), 2004.

[81] O. Zaharko, H.M. Ronnow, A. Daoud-Aladine, S. Streule, F. Juranyi, J. Mesot, H. Berger, and P.J. Brown. Incommensurate magnetism in the coupled spin tetrahedra system $Cu_2Te_2O_5Cl_2$. *Physika Nizkikh Temperatur*, **31**(1068), 2005.

[82] A. Zheludev. Interacting quantum spin chains. *Appl. Phys. A*, **74**(S1-S5), 2002.